Deliverable 16.7: MAGIC – T3-Report on micro scale chemo-mechanical modelling of leaching and carbonation and parameters upscaling

Work Package 16

This project has received funding from the European Union's Horizon 2020 research and innovation programme 2014-2018 under grant agreement N°847593.

Document information

Project Acronym	**EURAD**
Project Title	**European Joint Programme on Radioactive Waste Management**
Project Type	**European Joint Programme (EJP)**
EC grant agreement No.	**847593**
Project starting / end date	**1st June 2019 – 30 May 2024**
Work Package No.	**16**
Work Package Title	**Chemo-Mechanical AGIng of Cementitious materials**
Work Package Acronym	**MAGIC**
Deliverable No.	**16.7**
Deliverable Title	**Report on micro scale chemo-mechanical modelling of leaching and carbonation and parameters upscaling**
Lead Beneficiary	**PSI**
Contractual Delivery Date	**Dec 2023**
Actual Delivery Date	**January 2024**
Type	**Report**
Dissemination level	**L**
Authors	**Sergey Churakov (PSI), Alexandre Dauzères (IRSN), Cornelius Fischer (HZDR), Athanasios Mokos (PSI), Janez Perko (SCK CEN), Nikolaos Prasianakis (PSI), Suresh Seetharam (SCK CEN), Tri Phung (SCK CEN), Jianfu Shao (LAMCUBE), Jing Xue (LAMCUBE).**
To be cited as:	Churakov S., Dauzères A., Fischer C., Mokos A., Perko J., Prasianakis N. Seetharam S.C., Phung, T.P., Shao J.-F., Xue, J. (2024): Report on micro scale chemo-mechanical modelling of leaching and carbonation and parameters upscaling. Final version as of 19.01.2024 of deliverable D16.7 of the HORIZON 2020 project EURAD. EC Grant agreement no: 847593.

Disclaimer

Acknowledgement

This document is a deliverable of the European Joint Programme on Radioactive Waste Management (EURAD). EURAD has received funding from the European Union's Horizon 2020 research and innovation programme under grant agreement No 847593.

Status of deliverable		
	By	Date
Delivered (Lead Beneficiary)	Sergey Churakov (PSI)	Oct. 2023
Reviewed (internal review)	MAGIC board members	Nov 2023
Verified (WP Leader)	Alexandre Dauzères (IRSN)	Dec 2023-Jan 2024
Reviewed (Reviewers)	Janez Perko (SCK CEN)	Nov 2023
Approved (PMO)	Bernd Grambow	Jan 2023
Submitted to EC (Coordinator)	ANDRA coordinator	Jan 2024

Executive Summary

Task 3 of WP-MAGIC had the ambitious goal of analysing the microstructural evolution and the mechanical properties of cement pastes under various influencing chemical factor such as internal degradation, chemical recrystallisation/leaching due to the interaction with formation water and microbial activities. The current report provides analysis of existing numerical models and describe the newest development accomplished in the course of WP-MAGIC. In particular, it presents the results on micro scale chemo-mechanical modelling of leaching and carbonation as well as upscaling approaches for cementitious systems obtained under the framework of EURAD project WP-MAGIC. The results published in this report are obtained by the use of numerical simulations developed under the task 3.1-3.4.

The presented work is a collective effort of the several research groups namely CNRS/LAM3, HZDR, IRSN, SCK CEN and PSI. The major achievements of the Task 3 in the WP-MAGIC described in the report include:

- Development of Lattice-Boltzmann based simulator for the pore scale modelling of cement microstructure evolution.
- Development of a generic pore scale model coupling microbial activity, surface microtopography evolution and surface reactivity.
- Development of numerical and analytical approaches for prediction of mechanical properties of cement paste and mortar based on 3D microstructure conducted by pore scale geochemical codes.
- Application of ML/AI methods for acceleration of the numerical simulations and development of surrogate models.
- Application of the developed methods for assessment of degradation processes in cement and concrete including upscaling.

The report is organised in six chapters. Chapter 1 addresses impact of calcareous water on chemo-mechanical properties of concrete and transferability of lab scale experiments to field scale. Chapter 2 addresses the simulation of microstructure evolution at pore scale using traditional and surrogate model for geochemical solver. Chapter 3 presents homogenisation methods use for estimation of mechanical properties based on the microstructure models. Chapter 4 deals with upscaling of transport parameters from pore to continuum scale. Chapter 5 presents case studies relevant to Ca leaching and carbonation. The major finding and outlook are summarised in Chapter 6.

Table of content

List of Figures

List of Tables

Glossary

ASR	Alkali silica reactions
BSE	Back Scattered Electrons
CEM	Cement (CEM I, CEM II…)
CFL	Courant-Friedrichs-Lewy
CH	Calcium hydroxyde: Portlandite
CI	Cement-clay Interaction
CIGEO	Industrial Centre for Geological Disposal
CKD	Cement kiln dust
CNT	Classical Nucleation Theory
COX	Callovo-Oxfordian clay
C-S-H	Calcium Silicates Hydrates
DDL	Diffuse double layer
EC	European Commission
EDS	Energy dispersive spectroscopy
EPS	Extracellular Polymeric Substances
EPS	Extracellular polymeric substances
EU	European Union
EURAD	European Joint Programme on Radioactive Waste Management
FDM	Finite difference method
FE	Finite Element
FEM	Finite Element Method
FFT	Fast Fourier Transform
GC	Gouy-Chapman (model)
GDF	Geological disposal facilities
GEM	Gibbs Energy Minimization
HCP	Hydrated cement paste
HD	High Density
HET	Heterogeneous
HLW	High-level waste
HON	Homogeneous
ILW	Intermediate level waste
ITZ	Interfacial Transition zone

LAC	Low Alkaline Cement
LB	Lattice Boltzmann (method)
LBM	Lattice Boltzmann Modelling
LD	Low Density
LLW	Low level waste
LMA	Law of Mass Action
MAGIC	The chemo-mechanical aging of cementitious materials
MSH	Magnesium silicate hydrate
NN	Neural Networks
MAE	Mean absolute error
NS	Navier-Stokes
OPA	Opalinus clay
OPC	Ordinary Portland Cement
PB	Poisson Boltzmann
R&D	Research and Development
REV	Representative Elementary Volume
RH	Relative humidity
RMSE	Root Means Square Error
PSD	Power spectral density
RTM	Reactive transport modelling
SEM	Scanning Electron Microscope
URL	Underground Rock Laboratory
XRD	X-ray diffraction analysis

Introduction

Cementitious materials are widely used in radioactive waste disposal facility design, as conditioning material or structural support material for access galleries, disposal drifts or cells (e.g., concrete/shotcrete), and massive plugs for the sealing of repository infrastructure. The mechanical behaviour of cementitious materials is strongly influenced by disposal in in-situ conditions and the boundary conditions imposed by the geo-technical system and the host rock (i.e. water saturation, temperature, etc.), during both the operational phase and the post-closure transient period. To assess the performance of the cementitious components, studies must be extended over long periods of time, considering various operating conditions. Furthermore, over the long-term, ground- and pore-waters, with large chemical disequilibrium, are key driving factors for cementitious materials deterioration. The mineralogical and microstructural changes generated by these environments might have consequences on the mechanical behaviour of the cementitious matrix.

In Task 3 of WP MAGIC, the bio-chemo-mechanical models for microstructure evolution of cement paste and mortar exposed to various representative disturbances such as carbonation and calcium leaching relevant to the conditions of deep geological nuclear waste repositories are developed and validated using experimental characterisation and multiscale modelling benchmarks. The aim of this technical report is to provide a review of the state-of-the-art modelling approaches for chemo-mechanical evolution of cement microstructure and upscaling based the newest concepts used and developed during WP MAGIC.

1. Bio-chemo-mechanical processes in cement and concrete in the context of radioactive waste disposal

1.1 Cementitious material in repository concepts

In geological repositories for radioactive waste, cement and concrete are used to support the construction of the underground repository infrastructure (e.g. liner for tunnel reinforcement), immobilisation and conditioning of radioactive waste (e.g. waste matrix) and passive safety seals (e.g. post disposal sealing of underground infrastructure). To ensure the repository safety, the cementitious engineering barriers need to maintain their safety function for a long period of time, much longer the typical civil infrastructure.

Many European countries consider the disposal of low and intermediate level radioactive waste in argillaceous rocks. The French geological disposal project (CIGEO) for Intermediate Long-Lived Wastes (ILLW) and High-Level Wastes (HLW) includes a facility situated within a Callovo-Oxfordian claystone formation. According to the plan for disposal of ILLW, the disposal cells are expected to be constructed from cementitious materials (liner, confinement plugs, and waste containers). The sealing zones, both horizontal and vertical, will be comprised of a bentonite core positioned between two concrete massive plugs. These zones will be exposed to various types of natural waters (calcareous or clayey water) based on the facility's location. Swiss concept of geological disposal considers a combined repository for HLW and L/ILW (Long / Intermediate Level Waste) in Opalinus clay formation (Nagra, 2021). Large quantities of cement are used as waste matrix, sealing of the L/ILW repository, tunnel support and post disposal sealing. Over time, these materials will interact with carbonate saturated formation pore water which will contribute to the degradation of concrete infrastructure in addition to the internal degradation of the cement paste. Alike, Belgium waste management authorities considers potential implementation of geological disposal in poorly indurated Boom Clay or Ypres Clay formations (NIROND, 2001).

Concrete used for construction of tunnel support and sealing zones have specific requirements on the mechanical performance for an extended period. These safety relevant construction elements will be exposed to various types of natural waters (calcareous or clayey water) based on the facility's location. Both, experimental studies and numerical simulations are necessary to assess the long-term performance of concrete under site specific conditions. The corresponding processes are very slow and in-situ experiments require long, often too long to be implemented, duration of experiments. The main component in concrete that provides structural integrity is hardened cement paste. In this context the characterisation of cement microstructure evolution at a microscale and the microstructure evolution modelling with a consequent estimation of effective material properties based on multiscale simulations is a promising route for development of cement degradation models for long term prediction of bio-chemo-mechanical behaviour of cement and concrete. Consideration of small-scale experiments, often conducted in laboratory under controlled condition raise the question of data transferability for laboratory to the field scale and upscaling of the laboratory results.

1.2 Microstructure evolution and in situ chemistry of cement paste

The most essential chemical processes affecting the loss of mechanical stress of concrete in the geological waste repository are expected to be the internal concrete degradation enhanced by the exchange of hyperalkaline pore water solution with quasi pH neutral formation water, the Alkali-silica (ASR) and alkali-carbonate (ACR) reactions in concrete.

In the case of exchange of alkaline pore water solution with quasi pH neutral water, leaching of ions from cement paste happens. The evolution of Ordinary Portland Cement due to leaching can be described by four stages of cement degradation are considered depending on total exchanged water volumes and the pH and cement pore water controlling cement phases (pH-values are for the reference temperature of 25°C). At stage 1, the pH is larger than 12.5 and concentration of Na and K ions is high. At stage 2, the pH is equal to 12.5 and controlled by the dissolution of portlandite (CH) with approximately 20 mmol of equilibrium Ca concentration in the pore water solution. Stage 3 onset when

all portlandite has been leached out of the cement and the pH is between 12.5 and 10 (Jacques et al., 2014).

Cement paste microstructure consists of different mineral phases and a complex network of pores between the solid phases. The porosity has a multiscale character with specific features manifesting at nano and micro-meter scales and even at mm scale in case of fractures. Hardened cement paste consists of numerous solid phases, most important of which are portlandite (CH), calcium-silicate-hydrates (C-S-H), and aluminium containing phases such as AFm and AFt (Winter, 2009).

Mineralogical and consequently microstructural changes occur in cementitious systems due to chemical evolution towards stable mineral fluid equilibria in the cement paste itself or result of chemical equilibration with the environment. The mineralogical composition and microstructural transport properties determine the chemical stability of the solid, the mobility of species, and the overall fluid flow through the system. Accurate description of chemical interaction in cement system is a prerequisite for the prediction of long-term performance and assessment of mechanical properties of cementitious materials. In practical applications, chemical changes manifest as hydration and degradation, which are occurring at the same time. Even the predictions of the mineralogical and microstructural changes during hydration alone is a challenging task.

The cement clinker and additives react with water to form the hydration products. The hydrating system is initially a colloidal suspension, and the hydrated reaction products increase in volume (Snyder, 2009). The volume fills the inter-particle porosity, which initially has been filled with water. Precipitation leads to formation of inter-connected network of solids resulting in significant structural modifications in cement paste. As soon as a sufficient inter-connected network of solids is established, the paste becomes mechanically stable and can support an amount of shear stress. Hydration continues further and reaction products fills the remaining void space, thereby increasing the load carrying capacity, quantified in practice by the compressive strength (Zhihui, Guang, & Surendra, 2005). The pore system becomes denser with hydration and diffusion slowing down due the higher tortuosity of the transport path.

There is a wide range of possible blended cementitious mixtures that may be used, and the specific physical/chemical properties of supplementary materials that influence hydration process (Scrivener & Kirkpatrick, 2008). Hydration and degradation processes are both controlled by transport of water and ionic species in the aqueous pore solution and chemical reactions between ionic species in the pore solution and the soluble mineral phases present.

Modelling of cementitious systems often assumes that the material is a porous matrix and that aqueous pore solution is in equilibrium with the solid phases in the material composite. Geochemical model relies on the thermodynamic databases that should in principle include all relevant solid phases. Sufficiently accurate data, exist for the most important reactions in Portland cement, fly ash, ground granulated blast furnace slag, and silica fume. For some mineral phases, however, more accurate data are needed for the solubility and the temperature dependence. The equilibrium calculations provide the quantity of mineral phases that either dissolve or precipitate, thereby changing the pore structure and the transport properties, which can be numerically evaluated by a 3-D microstructure model. From a chemical point of view, geochemical reactions induce a gradual change in the pore water composition, from typical "young" concrete pore water with a pH above 13 (for ordinary Portland cement) to more evolved pore water with a pH lower than 10 (Jacques et al., 2013). The extent of this process strongly depends on the availability of water and water to solid ratio. SEM BSE image of transition zone of leached sample showing leached CH and consequent larger porosity is shown in Figure 1-1 (Phung et al., 2016).

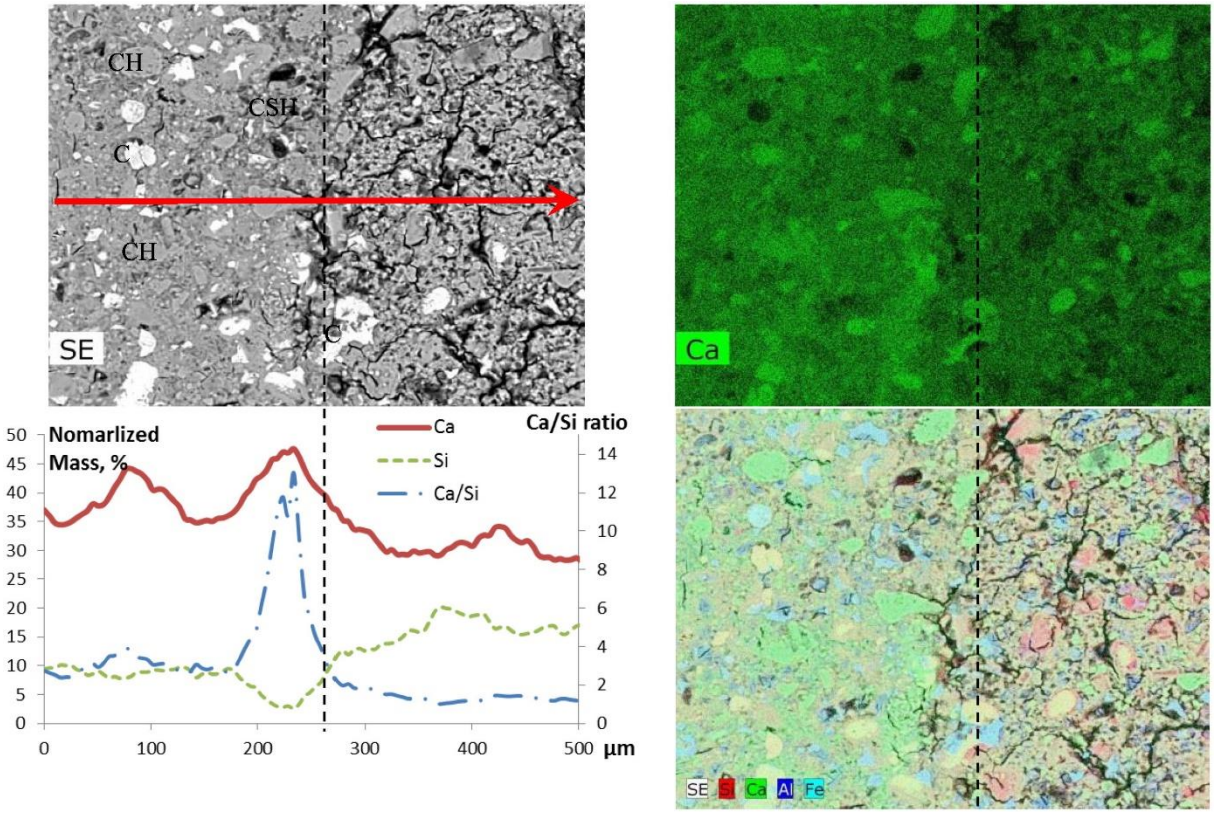

Figure 1-1: Image of transition zone of leached sample (reproduced from (Phung et al., 2016)).

The pore water composition is buffered by different cement phases including AFt, AFm and calcium-silicate hydrates (C-S-H phases). The end of this state is defined when all these phases are completely leached out. State 4 has a pH lower than 10 with aggregate minerals present; in this system calcite is the only aggregate used. The pore water composition is then mainly influenced by the composition of the infiltrating water.

Ingress of natural groundwater into cement induce physico-chemical modifications in the concrete matrix (carbonation, leaching, ettringite precipitation) upon contact with the host rock, due to its neutral pH and varying concentrations of sulphates, carbonates, and magnesium (Dauzeres et al., 2016; Neji et al., 2022). Conversely, the highly alkaline pore solution of the cementitious material affects the geochemical properties of the host rock (Tinseau et al., 2006). To limit the interaction between concrete and the host rock, globally recognized cementitious formulations termed "low-pH" have been developed. These formulations involve mixing Portland cement with pozzolanic additives. These additives create a cementitious matrix without Portlandite, which in turn reduces the pH of the interstitial solution (Codina et al., 2008; Bach et al., 2012), thus minimizing chemical degradation for both materials.

1.3 Impact of calcareous water on chemo-mechanical properties of concrete transferability of laboratory studies to field scale

The results obtained in laboratory under controlled conditions need to be tested at the field scale and upscaled to the real operation condition. In particular the concrete performance observed in lab tests need to be confirmed under the in situ conditions on industrial scale. In the framework of the IMCB (Impact of calcareous water on chemo-Mechanical Behaviour of concrete) project conducted in collaboration with WP-MAGIC, IRSN and several other project partners investigate the chemo-mechanical impact of calcareous water on the low-pH cementitious matrix. In particular, this study aims to estimate the potential difference in concrete performance observed in controlled conditions and on an industrial scale. To this end, one set of HCP samples was cast in the laboratory, and another set of concrete samples and massive concrete structures were casted using a large scale outside experimental platforms. After the hydration period, samples were immersed in a high volume of natural calcareous ground water. Periodic characterization was performed by SEM-EDS, µ-CT, XRD and micro/nano-indentation.

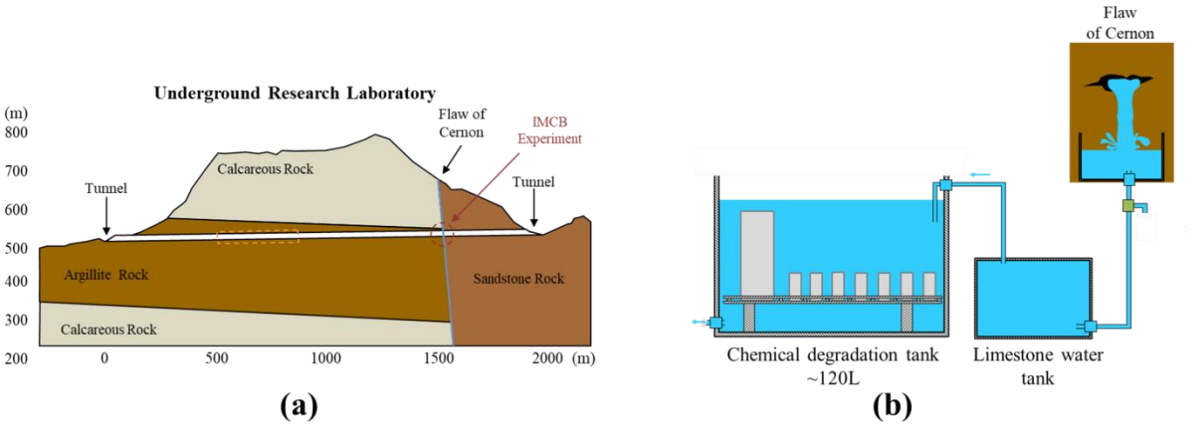

Figure 1-2: Illustrative sketch (a) of the underground research laboratory of Tournemire and (b) of the IMCB-TR experimental setup.

Two experimental setups were used. The first system set up in December 2018 in the IRSN underground research laboratory (URL) in Tournemire (IMCB-TR) was only composed of centimetre sized samples (Figure 1-2). The second one (IMCB-ODE), started in October 2019 and located in the ODE platform of Cadarache (South of France), was focused on macroscopic scale. In both cases, the composition of the synthetic solution in the reservoir was equivalent to natural calcareous ground water from the Cernon fault in the URL of Tournemire. Table 1-1 details the concentration of the main chemical elements present in this water.

Table 1-1: Chemical composition of water from the Cernon fault.

Chemical element	Concentration mmol/L / pH
Ca^{2+}	1.91
HCO_3^-	5.9
Mg^{2+}	0.82
SO_4^{2-}	0.06
pH	8.2

The first aim of this study was to provide insights for understanding the chemo-mechanical behaviour of a low-pH cementitious matrix in contact with calcareous ground water.

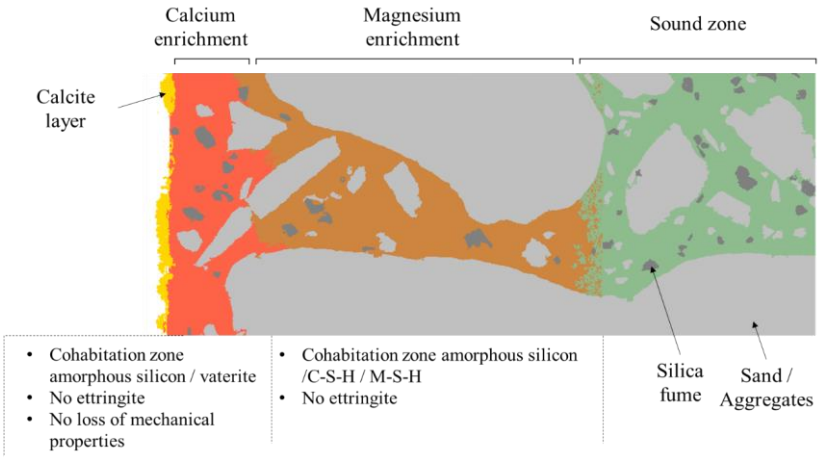

Figure 1-3: Illustrative diagram of the degradation scenario proposed to explain the alteration of low-pH cementitious matrix in contact with calcareous water.

The experimental campaign coupled with numerical simulations reveals the following mineralogical changes (see Figure 1-3):

- At the interface, a crust of calcium carbonate is visible.
- The first hundred microns are characterised by the calcium enrichment and the presence of amorphous silica. Vaterite has been identified in this domain, too. The presence of vaterite compensates for the weak elastic properties of the amorphous silica providing a high Young's modulus of the composite material (see Figure 1-4). A flaking phenomenon in this zone is anticipated, likely due to the low Young's modulus of amorphous silica.
- Magnesium enrichment is observed upstream to the previous zone. Despite the low concentration of the infiltrated solution, the model and SEM-EDS measurements show that the magnesium enrichment can, in some cases, reach 20% of the volume ratio of the material. The low mechanical properties of the magnesium phases usually observed in low-pH matrices raise the question of the durability of this zone.

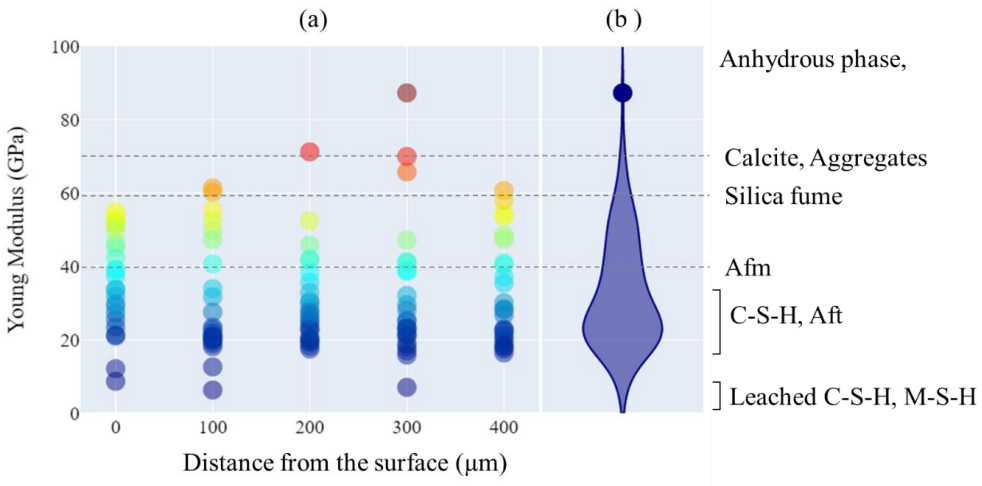

Figure 1-4: (a) Distribution of Young's moduli measured by micro-indentation as a function of depth where each point corresponds to a single micro-indentation measurement and (b) global violin diagram for a low-pH T3 concrete immersed for 8 months in IMCB-ODE. Dotted lines indicate typical value for the individual cement phases.

The second objective of this study was to estimate the potential deviation of results between a study made in controlled laboratory conditions and another less constrained condition corresponding to industrial manufacturing. The manufacturing protocol seems to have a significant impact on the chemical

response of the cementitious materials. A high porous zone appears at the interface in large concrete blocks cured outside and wrapped with stretch film. The evolution of transport properties in this zone has an effect on the degradation scenario. In the case of cementitious materials cured under controlled laboratory conditions, the interaction with the external solution induces formation of a layer of calcium carbonates, which tends to close the porosity. This low porosity zone seems to have a passivation function and slows down the leaching, so that no degradation is noticed in the cement matrix. In the high porous zone, the formation of two large zones, one enriched in calcium at the interface and another further upstream enriched in magnesium is observed. The observed evolution of these zones raises some concerns regarding the potential flaking in the calcium carbonates zone and the low Young's modulus of the magnesium phases, which are expected to precipitate in the magnesium enrichment zone. However, the observed change seems to be limited to the high porous zone, without impacting the integrity of the concrete structure.

As observed in IMCB project, in contact with natural ground water, the leaching of the low-pH cement matrix may be accompanied by an enrichment in magnesium leading to the formation of brucite and/or magnesium silicate hydrates (M-S-H), the properties of which are poorly known (Dauzeres at al., 2016; Bernard et al., 2017).

The PM2SH project comprises a multi-physics study of the weathering of low calcium matrices by magnesium containing waters at the mesoscopic scale. The main aim of the study was to understand the reaction mechanisms of M-S-H formation in low-calcium cementitious matrices, and to study its influence on micro-structural and mechanical properties on concrete. Two cementitious pastes (model paste based on colloidal silica and real paste based on silica fume and slag) were exposed to solutions with different Mg concentrations (5 and 50 mmol/L).

The model cement pastes were composed by CEM I and colloid silica, whereas the low-pH paste was produced by mixing CEM III A with silica fume. After the manufacturing, the pastes were kept under endogenous conditions for 2 years. Then, cylindrical samples (diameter=3cm, thickness=1cm) were cut, coated with sealant on the lateral side to allow unidirectional degradation. The samples were immersed in magnesium solutions in 60 L closed tanks for 4 months. The solutions were constantly agitated and renewed every two months. At the end of the exposure time, two samples were taken, cut out and prepared for the various characterization tests.

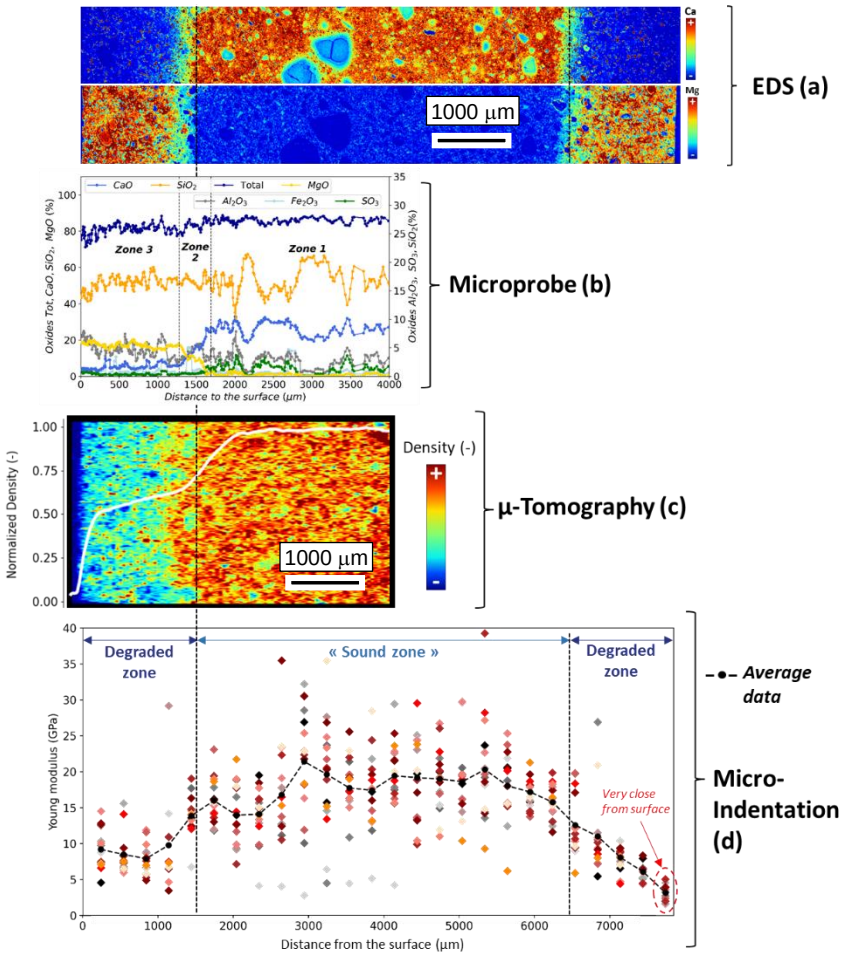

Figure 1-5: Multi-physics characterization of a low-pH industrial cement paste after 4 months interaction with 50 mM $MgCl_2$. (a) 2D maps of Ca and Mg distribution. (b) 2D density map. (d) Each point represents individual nanoindentation measurement, and the dushed line is the spatial average on the Young moduli.

In the study of the low-pH model paste, the measured mineralogical properties and microstructural, result in mechanical properties of the degraded paste which a much lower than those of T3 concrete used in IMCB project (Figure 1-5). The sound paste was homogeneous and composed only of C-S-H and ettringite. In contact with the $MgCl_2$ solution, at 5 mM or 50 mM, the findings were the same. The magnesium attack causes the leaching of calcium and sulphate, dissolving the only two phases observed in XRD namely C-S-H and ettringite. The degraded zone entirely consisted of M-S-H. No other phases are available to compensate for poor microstructural and mechanical properties of M-S-H in the degraded sample, contrary to T3 concrete where the low water to cement ratio and the presence of other phases such as slag limit the impact of M-S-H formation on the microstructural and mechanical properties of the material.

In conclusion, the analysis confirms that the magnesium attack is characterised by the dissolution of C-S-H and ettringite, as well as by the formation of M-S-H during the contact between a low-pH paste/concrete and an environment containing magnesium. **As M-S-H has much looser microstructure and weaker mechanical properties than C-S-H, the replacement of C-S-H by M-S-H does not lead to good mechanical and microstructural properties. Even if a new semi-amorphous phase is formed, the mechanical properties of the paste are significantly reduced during magnesium attack**.

2. Numerical modelling of cement microstructure

2.1 Pore scale reactive transport modelling concepts

Pore-scale models increase the detail of micro-scale heterogeneity such as the explicit representation of the pore structure or mineral structure (Li et al., 2006; Raoof et al., 2012; Prasianakis et al., 2018; Molins and Knabner, 2019). Several reactive transport models are already developed to study dissolution-precipitation reactions at micro- and mesoscales: finite-volume methods (Deng et al., 2016; Li and Jun, 2017; Molins et al., 2017; Seigneur et al., 2017), smoothed particle hydrodynamics (Tartakovsky et al., 2007), pore-network models (Li et al., 2006; Raoof et al., 2012), and lattice Boltzmann methods (Kang et al., 2007; Kang et al., 2010; Yoon et al., 2012; Prasianakis et al., 2018; Patel et al., 2014; Poonoosamy et al., 2019). Most numerical studies for carbonation of cementitious materials deal with CO_2-rich environments for the application in fields such as CO_2 sequestration. The process and the evolution of carbonation are different when concrete structures are exposed to CO_2 concentrations close to atmospheric conditions or to high CO_2 concentration conditions. Some case studies for dissolution-precipitation considered only constant boundary for dissolved CO_2 concentrations (Raoof et al., 2012; Seigneur et al., 2017), while r, for structures exposed to atmospheric conditions, a fixed partial pressure of CO_2 at air-liquid boundary interface would be an appropriate choice.

In cementitious materials, the rate of chemical evolution is often controlled by ion transport. This is because cementitious materials are characterized by fine pores, with the majority below the scale of a few micrometers. Moreover, cementitious materials also have heterogeneous distribution of solid phases. Similar to pore sizes, also the sizes of solid phases are mostly below the scale of a few micrometers. Hence, to obtain representative properties of the materials and provide reliable process description the studies have to be done at least on the spatial scale of a few micrometers (Shih et al., 1999; Thomas et al., 1996).The cement paste microstructure is described by a complex network of pores and intergrown solid phases. Each transition between phases or minerals requires an interface with mostly a very sharp transition of physical, chemical and mechanical properties. The numerical description of such system requires numerical approaches that can cope with many boundaries, sharp transitions and are computationally cheap. In addition to the traditional numerical methods (finite difference, finite element and finite volume methods), the lattice Boltzmann method is increasingly used in recent years (Molins et al., 2021).

The lattice Boltzmann method stems from particle methods and solves a simplified form of the discrete Boltzmann equation, which describes the evolution of a particle distribution function $f_i(\boldsymbol{x},t)$ at position $\boldsymbol{x}$ in time t and direction i. The particle distribution function $f_i(\boldsymbol{x},t)$ in the lattice Boltzmann method does not represent discrete particles, but the probability of finding a particle with speed e_i at position $\boldsymbol{x}$ in time t. Because the method is based on particles, the definition of particle translation and collision in the lattice are quick operations and boundary conditions can be very easily defined (e.g. particle bounce-back for no-flow condition). Moreover, the behaviour of particles at position $\boldsymbol{x}$ is only defined by the particles at the neighbouring nodes in the lattice. Hence, there is no need to solve systems of equations, which makes the method very attractive for parallelization. Moreover, because of the particle nature of the method and inherent link between spatial and temporal scales, von Neumann criteria are always respected.

Although the description of the system at pore scale assumes different discrete phases, some phases and processes cannot be represented explicitly in the model. The pore size distribution of a typical microstructure of a hardened cement paste (Phung et al., 2017) shows pore sizes ranging from a few nano-meter scale to micrometers. Such large range of scales (10^2-10^3) obviously cannot be represented in a single model. Many pore-scale dissolution-precipitation models assume that the voxels contain either pore space or a single solid phase (Kang et al., 2004; Kang et al., 2010; Yoon et al., 2012). However, the regions with mixtures of very small pores and solids are often more homogeneous (e.g. C-S-H amorphous phase in hardened cement pastes).

For such “multiscale” materials it has been proposed to upscale the properties for these phases and use them as effective properties in the pore-scale model (Patel et al., 2021). When we have a combination of discrete phases and phases with effective properties in the same model, we refer to this approach as multi-level approach (Patel et al., 2021; Varzina et al., 2020).

Multi-level models have been used to examine the role of gel porosity in the diffusivity of cement paste (Patel et al., 2018), to study the evolution of leaching from cement paste (Perko et al., 2020) and carbonation of portlandite (Varzina et al., 2020). An example of 3D dissolution at pore scale is shown in Figure 2-1.

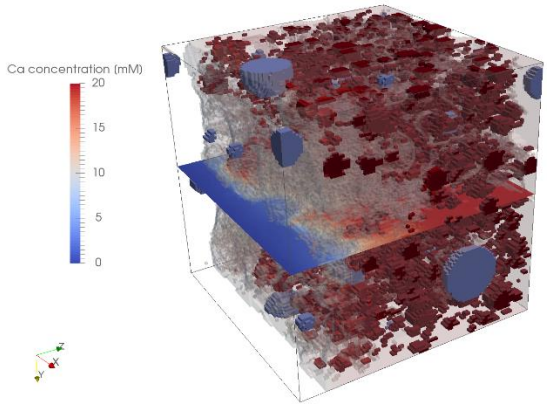

Figure 2-1: Modelling of leaching of cement paste with de-ionised water (left boundary condition). Portlandite is marked with red colour, C-S-H phases with grey and clinkers with blue. The cross-section represents dissolved Ca concentration (Perko, Ukrainczyk, Šavija, Phung, & Koenders, 2020).

Currently, one of the major challenges in the multi-scale modelling of systems with several primary and secondary phases is coupled description of dissolution and precipitation reactions in the same voxel containing one or more phases. For example, dissolving portlandite in a voxel provides space for calcite precipitation and additional pores. These processes can only occur in adjacent voxels when single phase voxels models are applied. To overcome the discussed limitations, the pore-scale models dealing with combined precipitation-dissolution processes, a new pore-scale modelling concept is introduced to account for simultaneous dissolution and precipitation reactions within a voxel and the development of residual porosity (Varzina et al., 2020). The pore-scale coupled reactive transport process is solved with a lattice Boltzmann method using the multilevel approach that allows representation of voxels with mixed phases. A specific framework is added to handle sub-grid dissolution and precipitation patterns and effects of limitation of the precipitation in confined spaces with extreme small pore radii (Emmanuel and Berkowitz, 2007) also termed as pore-size dependent solubility (Ghosh et al., 2001; Liu and Jacques, 2017). Taking a pore-size dependent solubility into account may prevent the pore space to be completely occupied by solid phases during carbonation. Consequently, a so-called residual porosity remains in a carbonated layer allowing for diffusive transport of aqueous species.

Recently, a lot of attention has been devoted in the nucleation principles in pore-scale models. Most models until now assume heterogeneous nucleation that initiates at the boundary of dissolving mineral. This assumption is based on the classical nucleation theory (CNT) where it is shown that the energy barriers and formation of critical nuclei is higher for homogeneous reaction (Prasianakis et al., 2017).

Several studies touched upon the effect of nucleation to the precipitation process. For example, Nooraiepour et al. (2021) investigates the precipitation of calcium carbonate crystals on a heterogeneous sandstone substrate as a function of chemical super saturation, temperature, and time. The goal of the study is to delineate the amount and location of nucleation and precipitation events in the spatial-temporal domain. The results showed that probabilistic nucleation contributes to broad stochastic distributions in both amounts and locations of crystals in temporal and spatial domains. The influence of the use of CNT on heterogeneous nucleation has been studied in (Starchenko, 2022). This

study coupled the pore-scale reactive transport modelling with the Arbitrary Lagrangian-Eulerian approach which allowed for tracking evolution of explicit solid interface during mineral precipitation.

Pore scale models can be time consuming. The reason is that in order to capture the critical features at the pore scale, such as the presence of capillary pores or heterogeneity in mineral phases, geometrical information with high resolution is needed. Often the purpose of a microstructural model is to upscale the information obtained at the pore to the continuum scale. In practice this entails respecting representative elementary volume (REV) which, in heterogeneous materials, can be large. Thus, detailed spatial information for a sufficiently large simulation domain requires a fine and large computational discretization resulting in a large number of unknowns and huge memory and computational costs, especially for three-dimensional domains.

The time step is constrained by numerical stability criteria, for example by Neumann criteria for diffusion, or Courant-Friedrichs-Lewy (CFL) stability criterion for advection/diffusion transport conditions. These criteria are linked to the spatial discretization and smaller time steps are needed for finer spatial discretization. Usually, the size of the numerical domain and its discretization are defined by the experimental settings and characterization methods. Consequently, when more complex and larger models are imposed, the most straightforward approach is to computationally optimize the solution, either by parallelization of processes or by increasing of computational resources e.g. solve the problem on a supercomputer. Groen et al. (2013) have shown that lattice Boltzmann method can be well scalable up to 32.000 cores with only 11% slowdown. However, even for a parallelized framework, the number of time steps is fixed as it is defined by stability criteria enforced by the migration conditions, either being diffusion or advection/diffusion (fixed by physics) and spatial discretization (fixed by the model). This issue has also been recognised in (Blunt et al., 2013) for flow simulations on pore-scale. Another way of reducing computational time in a coupled reactive transport model is by making the computationally demanding geochemical calculations less demanding by e.g. look up tables (Huang et al., 2018), first-order estimations (Allan et al., 2017) or surrogate modelling (Lucia et al., 2017).

For chemically buffered materials, a very efficient approach is to reduce the number of geochemical time steps by scaling of solid amount. The conditions under which the scaling is possible and the extent to which they could be scaled is described in (Perko and Jacques, 2019).

With in MAGIC project PSI team has further developed an advanced model for the chemical and structural evolution of cementitious materials at pore scale, using a three dimensional high resolution multi-component LBM approach. The LB code solves the advection-diffusion equations for the concentrations of the different components of the cementitious materials mimicking a continuous fluid in the macroscopic limit (Qian, et al., 1992; Lallemand and Luo, 2000; Wolf-Gladrow 2000). The code benefits from efficient parallelisation algorithm compatible with the most advanced HPC infrastructure and is tuned for massively parallel execution using graphical processor units(hybrid-CPU/GPU).

2.2 Microstructure evolution due to leaching of cement phases

Within WP – Magic, the project partners at SCK CEN, CNRS-LAM3 and PSI jointly investigate the effect of the leaching on the mechanical degradation of cement using 3D Lattice Boltzmann (LB) simulation and numerical simulation of mechanical properties of cement paste (See section 3.1). The LB method is used to simulate the diffusion of Ca ions through the hydrated porous material, caused by the dissolution of portlandite (CH).

The advection-diffusion equation is then recovered from the Boltzmann equation through a multi-scale Chapman-Enskog expansion (Qian, et al., 1992; Lallemand and Luo, 2000; Wolf-Gladrow 2000). To describe the particle interactions, the LB method uses a concentration distribution f, which is advanced in time and space by Equation (2.1):

$$f_i(\boldsymbol{r} + \boldsymbol{e}_i\,\Delta t,\ t + \Delta t) - f_i(\boldsymbol{r}, t) = \Delta t \Omega_i(\boldsymbol{r}, t) \qquad (2.1)$$

Equation (2.1) shows the evolution in probability because of the particle movement in space (left side) and its collisions with other particles (right side). The equation is discretised for nodes with coordinates

$\boldsymbol{r}$ and advances at time t with timestep Δt. The discrete velocities $\boldsymbol{e}$ correspond to its neighbouring nodes whose number depends on the lattice used. For these 3D simulations, a D3Q27 lattice is used, meaning the node is connected to 26 neighbours and the direction $i = 0{,}1 \ldots 26$ with 0 being the self-interaction of the node.

For the collision, Ω_i signifies the collision operator, for which multiple models have been developed (Wolf-Gladrow 2000). For these simulations, the Bhatnagar–Gross–Krook approximation with a single relaxation time (SRT) is used (Qian, et al., 1992), as shown in Equation (2.2):

$$\Omega_i^{SRT}(\boldsymbol{r}, t) = -\frac{1}{\tau}\left(f_i(\boldsymbol{r}, t) - f_i^{eq}(\boldsymbol{r}, t)\right) \tag{2.2}$$

The single relaxation time τ is used to connect the LB simulation to the diffusion process and by extension to a time step. In the SRT model, the distribution function f is locally relaxed towards an equilibrium function f^{eq}, which is computed by Equation (2.3) to minimise entropy while ensuring the conservation of mass and momentum.

$$f_i^{eq} = C_{Ca} \prod_{a=x,y,z} \frac{1 - 2e_{ia}^2}{2^{e_{ia}^2}} (e_{ia}^2 - 1 + e_{ia}u_a + u_a^2 + T_L) \tag{2.3}$$

The Ca concentration is linked to the LB distribution function through a summation: $C_{Ca} = \sum_{i=0}^{26} f_i$ and the relaxation time is connected to the diffusion coefficient of the dissolved Ca ions. The velocity $\boldsymbol{u}$ is also connected through a summation: $\boldsymbol{u} = \frac{1}{C}\sum_{i=0}^{26} f_i \boldsymbol{e}_i$ while the lattice temperature T_L is considered constant with a value of $1/3$. For the fluid-solid interaction at the boundaries, a non-slip (bounce-back) boundary condition is implemented.

The Ca mass balance is implemented based on the concept of 'quasi-solid' computational nodes, which keep track of both solid (within the CH) and dissolved Ca (liquid) concentrations. The quasi-solid nodes bordering the fluid are allowed to dissolve according to the reaction rate, until the solid concentration is reduced to 0, at which point the computational node is treated as fluid filled porosity.

Due to the coupled treatment of diffusive transport and surface controlled reaction kinetics the resulting computational time step for a fully resolved simulations is extremely small, i.e. in the order of milliseconds. To reduce the computational cost of the simulations, the LB code is accelerated by taking advantage of the clear separation of the diffusion and dissolution timescales. A smart variable time-stepping technique has been implemented which provides a significant overall acceleration of the code. The scheme will be described in detail in a future upcoming publication (Mokos et al., 2024).

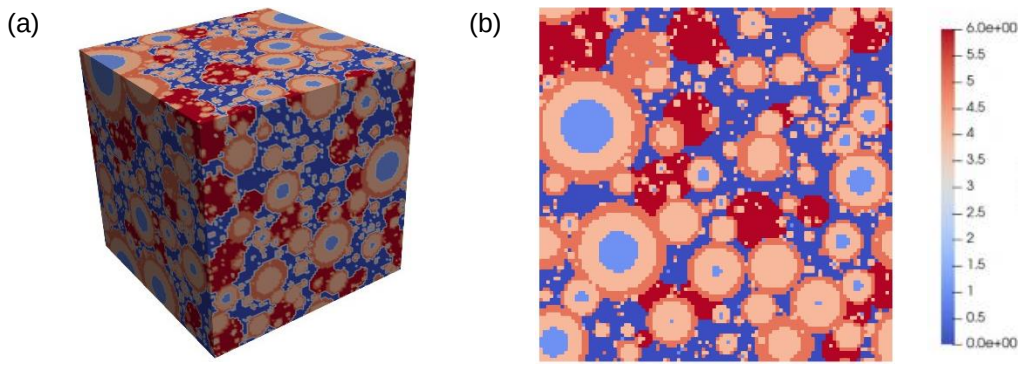

Figure 2-2: 3D geometry provided by the MAGIC partners at SCK-CEN (0 is fluid, 1 unhydrated phases, 4 high density C-S-H, 5 low density C-S-H and 6 is CH. (a) is the full 3D domain and (b) is a 2D slice from the middle of the domain.

The LBM is applied on a 3D OPC microstructure, algorithmically generated by HYMOSTRUC (van Breugel, 1996), and provided to PSI by the project partners at SCK CEN. The sample geometry is a

cube of size 10^{-4} m and represents a hydrated 60-day aged OPC, consisting of several phases generated as spheres by HYMOSTRUC. The microstructure consists of 14.4% CH, 21.1% high density C-S-H and 25.2% low density C-S-H with the remaining being unhydrated phases. The microstructure has a porosity of 0.233. Figure 2-2 shows the 3D domain and a 2D slice from the middle of the domain. One of the features of this realistic geometry may be seen in Figure 2-2(b). In 2D the pore-space is depercolated and there is no connectivity of the free pore-space. This is expected for porous media with porosities as low as 0.233 and signifies that the evolution of such realistic geometries cannot be consistently simulated in two-dimensional computational setups. Therefore, it is necessary to consider the three-dimensional representation where the pore-network is fully connected.

For the CH dissolution modelling, the C-S-H nodes were initially considered as inactive while the CH nodes were treated as considered quasi-solid. At the edges of the domain, a constant Ca concentration of 10^{-10} mol/l was applied, meaning essentially that the sample was entirely immersed in are large water reservoir. Applying the LB algorithm and the reaction equation, the gradual removal of the CH solid nodes is seen at Figure 2-3 and Figure 2-4 for two 2D slices extracted from the evolving 3D domain, at 50μm and 25μm from the cement edge respectively. Figure 2-5 shows the CH solid node removal for the entire 3D domain. The time scale of the removal can be estimated using the time step conversion (1 LB time step = 0.0014245s), which occurs by considering the similarity of the diffusion coefficient for dissolved Ca ions reported by Galan et al. (2015) as $1.17 \cdot 10^{-10}$ m^2/s with the LB relaxation time (selected as 0.5) and the current discretisation of the domain (1 lattice unit = 1 μm). For the dissolution of 50% of the CH nodes, in the described boundary conditions the system requires approximately 900,000 steps. The LB results are in line with the experimental dissolution rate, which predicts 9.35s or approximately 6,500 LB steps for a single voxel of volume $1\mu m^3$ to be entirely dissolved, when immersed in constantly replenished water and saturation is maintained at 0.

As seen in Figure 2-3 and Figure 2-4, the portlandite nodes slowly dissolve from the outer to the inner shell until they are removed completely. The rate of removal is higher near the edges of the domain rather than the centre. This is expected and is due to the boundary conditions imposed and chemical gradients are higher. Because we impose zero concentration boundary condition for Ca concentration, the amount dissolving from the CH nodes is transported outside of the domain through diffusion due to the concentration gradient with the boundaries. Naturally, this transport is faster at the edges due to the shorter distance. For example, there is a clear difference between the CH nodes in the centre of Figure 2-3 and the nodes in the upper right corner. The former only starts shrinking in Figure 2-3(d), while the latter has almost completely vanished at that point.

(a) 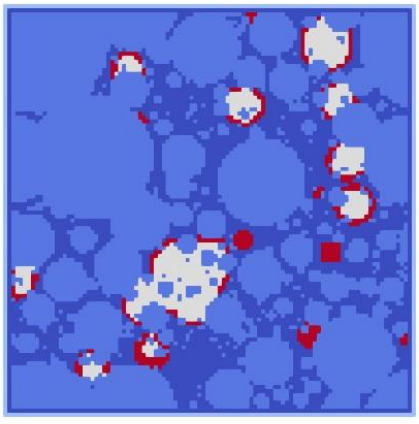 (b) 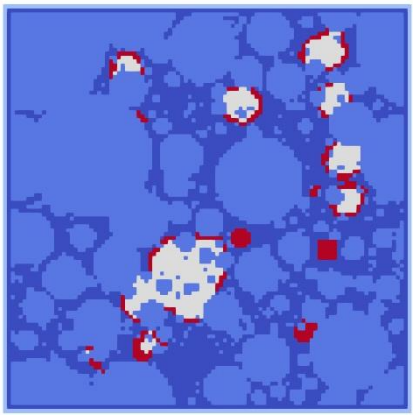

I

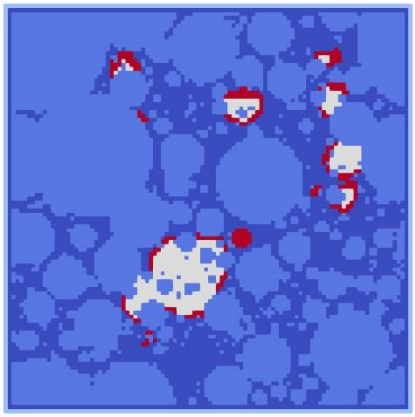

(d)

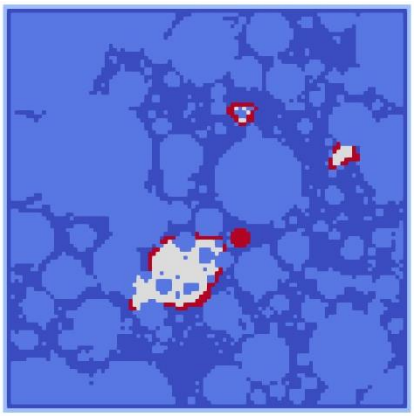

Figure 2-3: Snapshots of a 2D slices from the 3D simulation domain at 50μm from the beginning of the solids as the CH (red and white nodes, with red signifying dissolving CH voxels) solid nodes gradually dissolve. (a) is the beginning of the simulation, (b) after 29.3%, (c) after 49.4% and (d) after 76% of the CH solid nodes on the system have dissolved.

This is because at the centre of the domain, where transport is slower due to the limited pathways, the lower gradient to the neighbouring nodes (where dissolution may be also taking place) and the increased distance, the dissolution is occurring faster than the diffusion and the process is diffusion limited. As a result and as seen in Figure 2-6, the central domain is saturated with respect to CH. However, as the simulation progresses and the pore space evolves, the porosity increases and as a result new pathways for diffusion are created. Pore-water solution in the central domain exchange with the external reservoir and becomes undersaturated with respect to CH. The microstructure evolution in the central domain starts, as seen in Figure 2-6(b) and (d), which eventually lead to the full dissolution of CH in the sample.

(a)

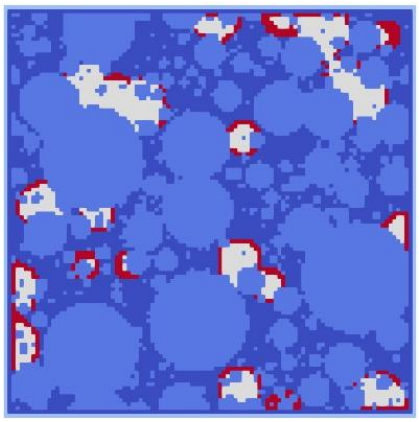

(b)

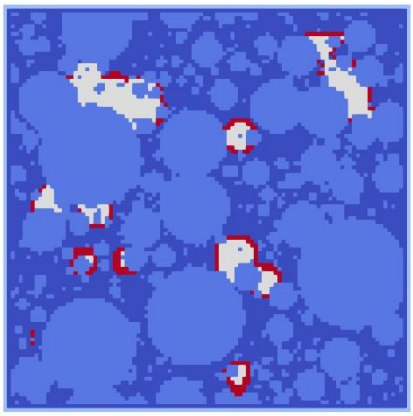

(c)

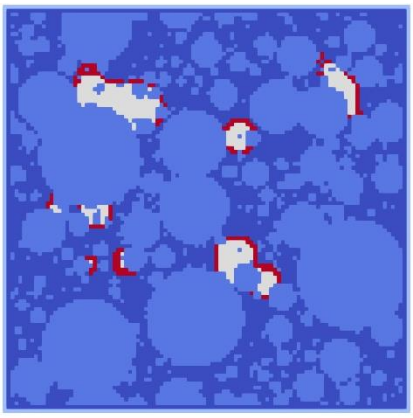

(d)

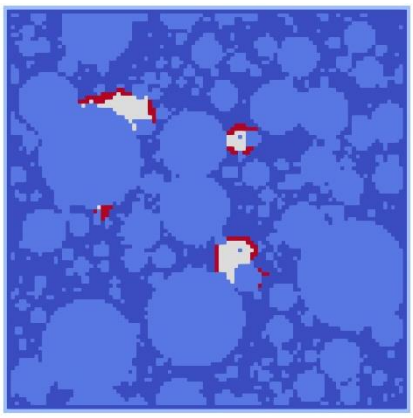

Figure 2-4: Snapshots of 2D slices from 3D simulation domain at 25μm from the beginning of the solids as the CH (red and white nodes, with red currently dissolving) solid nodes gradually dissolve. (a) is the beginning of the simulation, (b) after 29.3%, (c) after 49.4% and (d) after 76% of the CH solid nodes on the system have dissolved.

At the next level of model complexity both CH and C-S-H dissolution are considered simultaneously. The dissolution of C-S-H nodes (both high and low density) release Ca similar to CH dissolution. In addition, the C-S-H release Si, whose diffusion is also tracked in the model. To account for the changes in the Ca:Si ratio of the pore water solution, a recrystallisation of C-S-H solid solution with variable composition is implemented. To better understand the behaviour of such a complex system, the modelling is performed for boundary conditions with different Ca and Si concentrations particularly under conditions pertaining to the clay interface at the nuclear repository.

Such models are particularly important for modelling cement-clay interfaces, as the clay may be a Ca and Si source. Precipitation is a more complex phenomenon than dissolution, since the precipitation rate depends on the pore-size and the available mineral surfaces which can serve as the templates for heterogeneous nucleation and precipitation. To model such phenomena which involve several species, it is crucial to consider the chemical speciation. For that, the simulation code is usually coupled with a geochemical solver (Kulik et al., 2013) or a look-up Table. The LBM code has been extended with a surrogate NN for geochemical simulations (more details in Section 2.5) which enables the modelling of C-S-H precipitation at the cement-clay interface.

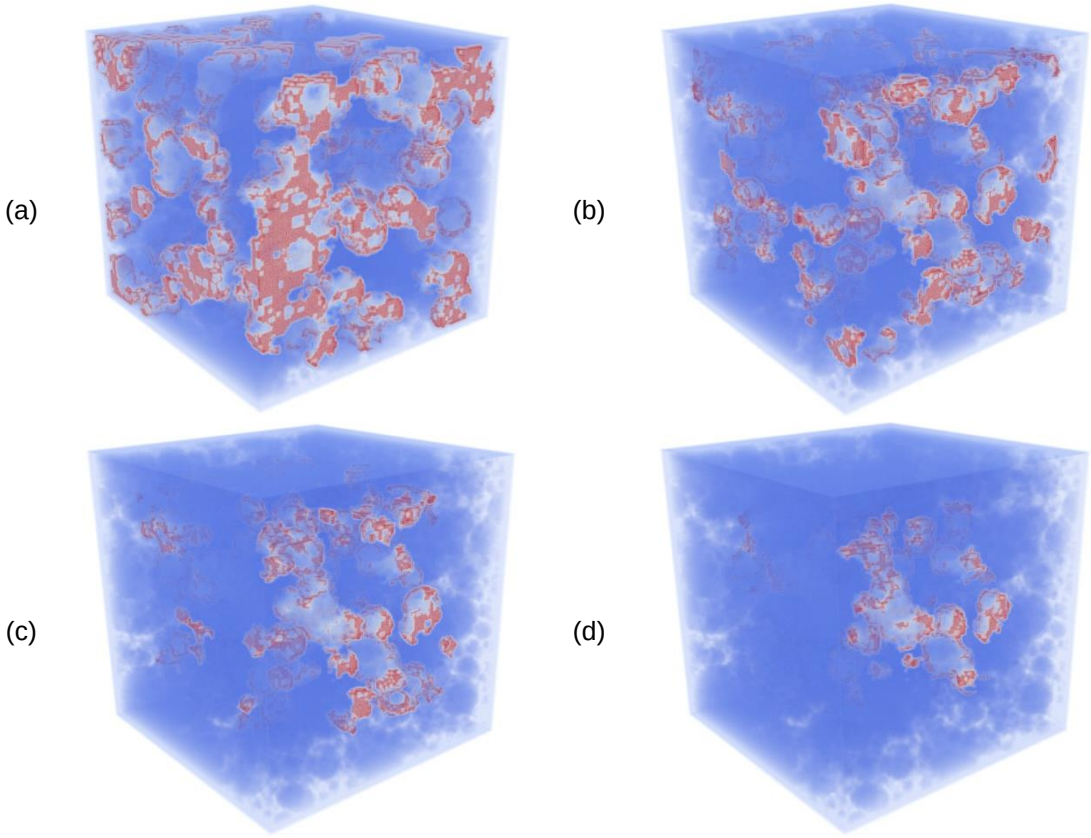

Figure 2-5: Snapshots of the 3D domain as the CH (red and white nodes, with red currently dissolving) solid nodes gradually dissolve. (a) is the beginning of the simulation, (b) 29.3%, (c) 49.4% and (d) 76% of the CH solid nodes on the system have dissolved.

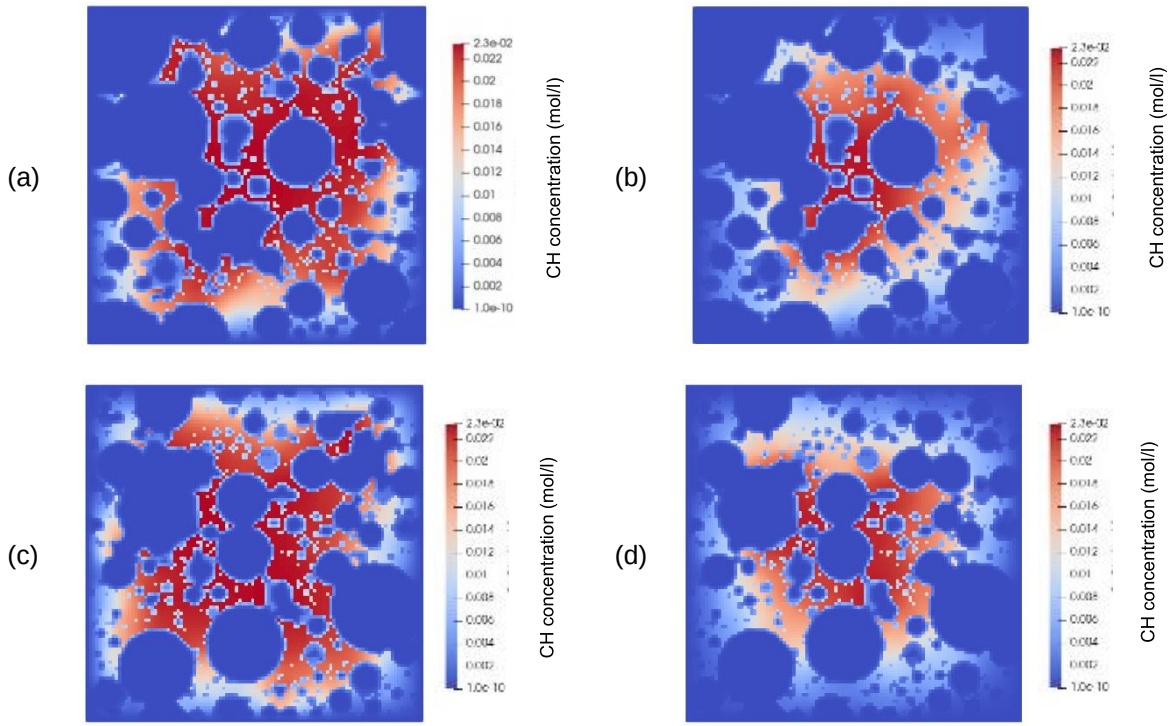

Figure 2-6: A 2D slices from 3D simulation showing CH concentration within the fluid after 30% (a), (c) and 75% (b), (d) of the CH solid nodes on the system have dissolved. (a) and (b) show a slice at 50µm from the edge while (c) and (d) show a slice 25µm from the edge.

2.3 Microbial activity and their effect on the surface reactivity

Microbial induced carbonate precipitation can be formed as a by-product of different microbial metabolic activities, including photosynthesis, ureolysis, denitrification, ammonification, sulfate reduction, and methane oxidation (Zhu and Dittrich et al., 2016). So far the best studied microbial metabolic activity is the ureolysis, where bacteria hydrolyze urea, an important nitrogen compound found in the environment. The products that will be formed are carbonate and ammonium (Mitchel et al., 2019) and in the presence of dissolved calcium carbonate can be formed. Ureolytic bacteria were found in different soils and aquatic environments (Arias et al., 2019, Bibi et al., 2018, Nasser et al., 2022) and can be also used for biotechnological applications (Fang and Achal., 2019, Jeong et al., 2017, Nasser et al., 2022). *Sporosarcina pasteurii* (formerly known as *Bacillus pasteurii*) has been extensively used as the model urease-producing organism in ureolysis-driven $CaCO_3$ precipitation studies, due to its high ureolytic activity (Yoon et al., 2001). Factors that seems to be beneficial for the excellent performance of this bacterium are for example the high negative cell surface charge of *S. pasteurii*, which is favourable for binding calcium ions and the good correlation between biomass growth and urease production (Ma et al., 2020,). The biomineralization of calcium carbonate by this bacterium was also studied in the presence of trivalent europium, a substitute for trivalent actinides, using time-resolved laser-induced fluorescence spectroscopy (TRLFS) and a variety of physicochemical techniques (Johnstone et al., 2016). During the $CaCO_3$ phase transformation Eu^{3+} speciation changed and resulted in several species incorporated in the calcite phase either substituting at the Ca^{2+} site or in a previously unidentified, low-symmetry site. Most of studies with *S. pasteurii* for $CaCO_3$ precipitation were performed under aerobic conditions, because *S. pasteurii* seems to be unable to grow anaerobically (Martin et al., 2012).

Biofilm growth, fluid flow and mass transfer in porous materials and their interactions need to be addressed in a coupled manner in Reactive Transport Modelling (RTM). At the core scale, an RTM was applied to simulate the microbial-induced calcite precipitation through ureolysis (Zhang & Klapper, 2010). Their model can predict the temporal and spatial evolution of rock porosity due to microbial-induced calcite precipitation. At the pore scale, a coupled RTM was applied to study the impact of microbial activity on the efficiency of underground hydrogen storage (Ebigbo et al., 2013). In this model, three microbial species (i.e., methanogens, acetogens, and acetotrophs) were considered to be active in the presence of high concentrations of hydrogen. The simulation results demonstrated that hydrogen

was consumed by these three microbial species. These studies proposed different numerical models at different length scales to simulate the microbial activities (e.g., growth and induced mineral precipitation) and corresponding physical and chemical processes. However, the study of the effects of microbial activity on mineral surface topography evolution was not included in these investigations. As a surrogate parameter to quantify the evolution of surface topography, surface roughness has a significant impact on various processes, such as mineral dissolution (Deng et al., 2018) and the adsorption of contaminants (Yuan et al., 2021). The impact depends on the scale on which the roughness is considered, chemical buffering of the system, kinetics and transport mode. For example, a microscale roughness has no effect for Ca leaching under diffusive transport, because there is almost no gradient between the roughness peaks (Perko et al., 2020). The increase of microbial activity on minerals causes changes in the substrate surface topography, affecting contaminant transport at the core scale and beyond. Consequently, a comprehensive understanding of the evolution of surface topography due to the microbial activity at the pore scale is beneficial to improve the estimation of contaminant migration in the subsurface.

In the course of MAGIC project, HZDR focused on the modelling and experimental study of microbially induced calcite precipitation and the evolution of mineral surface reactivity at the pore scale. This is a model system for a number microbially induced precipitation processes is studied in a complementary experimental project and has well constrained set of kinetic equations necessary for the reactive transport modelling. Among the six common microbial metabolic activities, i.e., photosynthesis, ureolysis, denitrification, ammonification, sulfate reduction, and methane oxidation, the ureolysis is the most common metabolism to induce calcite precipitation in soils and rocks (Zhu & Dittrich, 2016). In this study a pore-scale reactive transport model owing to microbially induced calcite precipitation through ureolysis taking place at the biofilm-mineral interface in porous media has been modelled at a pore scale. The model of ureolysis contains three parts: (1) urea hydrolysis catalyzed by ureolytic bacteria; (2) dissociation of carbonatic acid, bicarbonate ion, and ammonia; and (3) calcite precipitation in the presence of dissolved calcium ions. The numerical simulations describe the reactive transport in a flow-through cell and quantification of the evolution of surface topography by a statistical parameter, surface nanoroughness, and applying the power spectral density (PSD) analysis. The sensitivity analysis comprises the effects of advection, diffusion, and reaction on the evolution of surface topography. The surface nanoroughness and PSD was analysed based on two dimensionless numbers, Péclet (*Pe*) and Damköhler (*Da*) numbers, which determine the dominancy among the advection, diffusion, and reaction.

The coupled numerical simulations of the fluid flow, solute transport, and microbial-induced calcite precipitation at the pore scale are conducted using the micro-continuum approach (Soulaine et al., 2017; Soulaine & Tchelepi, 2016). In this approach, each control volume contains a pore region, or solid region, or both, which are differentiated by the volume fraction of void space, ϕ_f. In the pore region, $\phi_f = 1$. In the solid-fluid interface, $0 < \phi_f < 1$. In the solid region, the solid phase is described by a fictitious low-porosity material (i.e., $\phi_f = 0 \equiv 0.001$), which results in near-zero velocities in the solid regions and a no-slip boundary condition at the solid-fluid interfaces (Soulaine et al., 2017). In the mathematical model, the Stokes-Brinkman equation (Brinkman, 1947) is utilized for modelling fluid flow in both solid-free and porous regions in a single framework (Soulaine & Tchelepi, 2016; Yuan et al., 2016). We then couple the Stokes-Brinkman equation, the reactive transport equations, and rock property models for simulating the coupled processes.

The kinetics of calcite precipitation induced by hydrolysis of bacteria urea ($CO(NH_2)_2$) (Zhu & Dittrich, 2016), was described by Equations 2.4-2.8 (Mitchell et al., 2019). Firstly, the ureolytic bacteria produce the urease, which catalyses the hydrolysis of urea, resulting in the product of ammonia (NH_3) and carbonic acid (H_2CO_3) (Eq. 2.4). The ammonia and carbonic acid equilibrate in circumneutral aqueous conditions to form bicarbonate (HCO_3^-), ammonium ion (NH_4^+), and carbonate ion (CO_3^{2-}) (Eqs. 2.5-2.7). In the presence of the dissolved calcium (Ca^{2+}), the saturation state of the system shifts and as a consequence solid calcium carbonate ($CaCO_3$) is formed (Eq. 2.8). In this study, the Eqs. 2.4 and 2.8 are considered as the kinetic reactions, while the Eqs. 2.5 – 2.7 are the aqueous speciation reactions.

$$CO(NH_2)_2 + 2H_2O \rightarrow 2NH_3 + H_2CO_3, \quad (2.4)$$

$$H_2CO_3 \rightleftharpoons HCO_3^{-1} + H^+, \quad (2.5)$$

$$HCO_3^{-1} \rightleftharpoons CO_3^{2-} + H^+, \quad (2.6)$$

$$2NH_4^+ \rightleftharpoons 2NH_3 + 2H^+, \quad (2.7)$$

$$Ca^{2+} + CO_3^{2-} \rightleftharpoons CaCO_3. \quad (2.8)$$

The proposed mathematical model is solved numerically using a decoupled approach (Yuan et al., 2019), which contains four sub-steps within each time step: (1) solution of the Stokes-Brinkman and continuity equations resulting in velocities and pressure; (2) solution of reactive-transport equations using the calculated velocities, resulting in solute concentrations and updated volume fractions of solids; (3) the fluid-solid interface will be updated based on the updated volume fractions of the solid phase; (4) the local permeability is then calculated based on the volume fractions of porous regions using the Kozeny-Carman equation. The updated permeability will be used for the calculations in the next time step. In this study, the chemical reactions (i.e., Eqs. 2.4 – 2.8) are calculated using PHREEQC v3.7 (Parkhurst & Appelo, 2013). To solve the reactive-transport equations (cf. step 2), we couple the PHREEQC/IPhreeqc with a previously developed numerical simulator (Yuan et al. 2019) using a non-iterative operator-split approach (Steefel et al. 2015).

In the numerical experiment, we assume a constant concentration of biomass (Mitchell et al. 2019), which is attached to the mineral surface. Since the biomass can lead to a permeability reduction by a factor of 2000 if the biomass completely fills the pores (Dupin et al. 2001), we assume for simplicity the biofilm is the solid phase with a significantly low permeability. Therefore, no explicit differentiation is made between the biofilm and solid phase in the model. Moreover, we assume the calcite precipitation only occurs at the interface between water and solid phases with the following steps: (1) locate the interface cells that have a volume fraction of void space of one (i.e., $\phi_f = 1$) and at least have one neighboring cell of solid phase (i.e., $\phi_f = 0 \equiv 0.001$); (2) update volume fractions of the solid phase of the interface cells ($0 < \phi_f < 1$) based on the calculated precipitated calcite (cf. step 3 in numerical solution procedure); (3) repeat the growing process of (2) until the volume fraction of the solid phase of the interface cells reaches one (i.e., $\phi_f = 0 \equiv 0.001$); (4) repeat the steps (1) and (2) for the next interface cells. In this study, we consider that one cell has four neighbors in four principal directions (i.e., ±x and ±y directions) with identical growth probability in the two-dimensional (2D) Cartesian coordinates.

As a starting point for the modelling the surface data of the cement material analysed before starting the microbial experiment were applied (Figure 2.7).

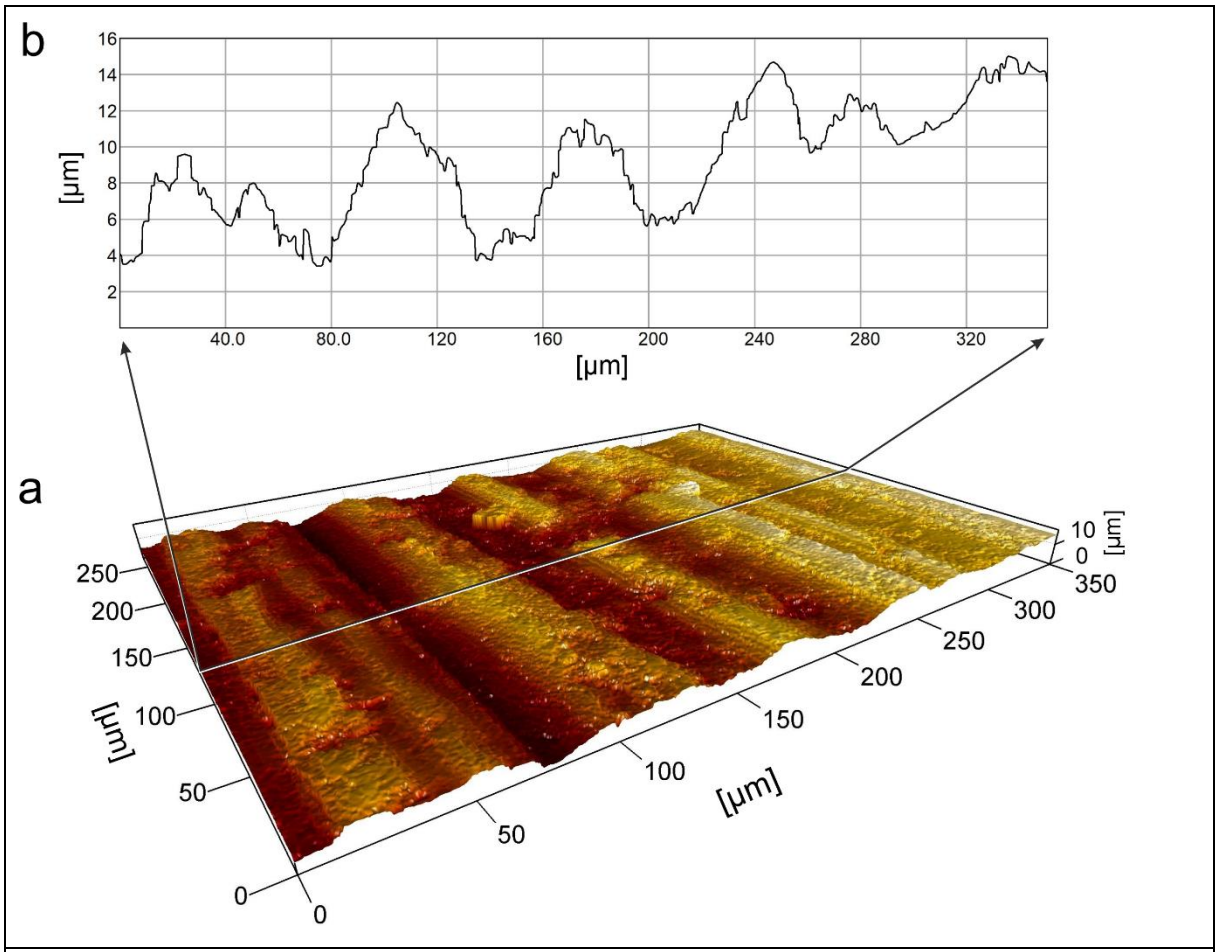

Figure 2-7: (a) Surface topography data of a representative surface section measured by confocal microscopy, cement material CEM1. Field of view (FOV) size = 350 µm × 260 µm, spatial resolution is ~258 nm × 258 nm. (b) One dimensional (1D) surface topography profile extracted from the surface data for the model. Profile line is marked by black arrows in (a). The pixel size is 258 × 129 nm^2.

Constant injection velocity (u_0) is applied at the inlet boundary. Thus, a certain length parallel to the flow direction is required for developing the Stokes flow situation, resulting in the calculated velocity distribution based on the momentum balance (Figure 2.8).

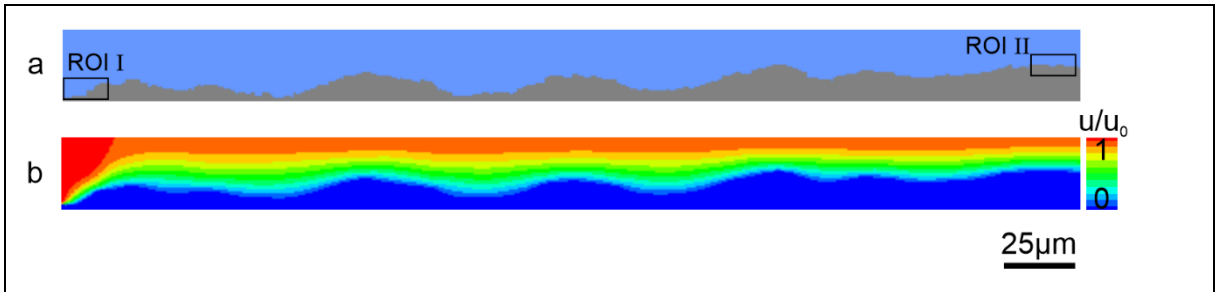

Figure 2-8: (a) 2D reactive transport model consisting of pore water (*blue color, upper part of the domain*) and solid phase (*gray color, lower part of the domain*). The profile data are extracted from the surface topography data (cf. Figure 1b). The biofilm is assumed to attach to the mineral surface and the thickness of the biofilm is ignored. (b) the relative velocity distribution (u/u_0) based on the rough surface, as shown in (a). A constant injected velocity (u_0) is applied at the inlet (left side). Solid phase in (b) corresponds to the zero velocity.

For a quantitative analysis of the change in surface topography due to the microbialy induced calcite precipitation, the evolution of surface roughness was analysed. Power spectral density (PSD) analysis

provides insight into the frequency of surface building blocks of different sizes. The difference in surface topography (before and after precipitation) is available by comparing the PSD curves of the initial and simulated surface. Figure 2.9 illustrates the size-specific modification of the PSD curve due to the microbial-induced site-specific calcite precipitation.

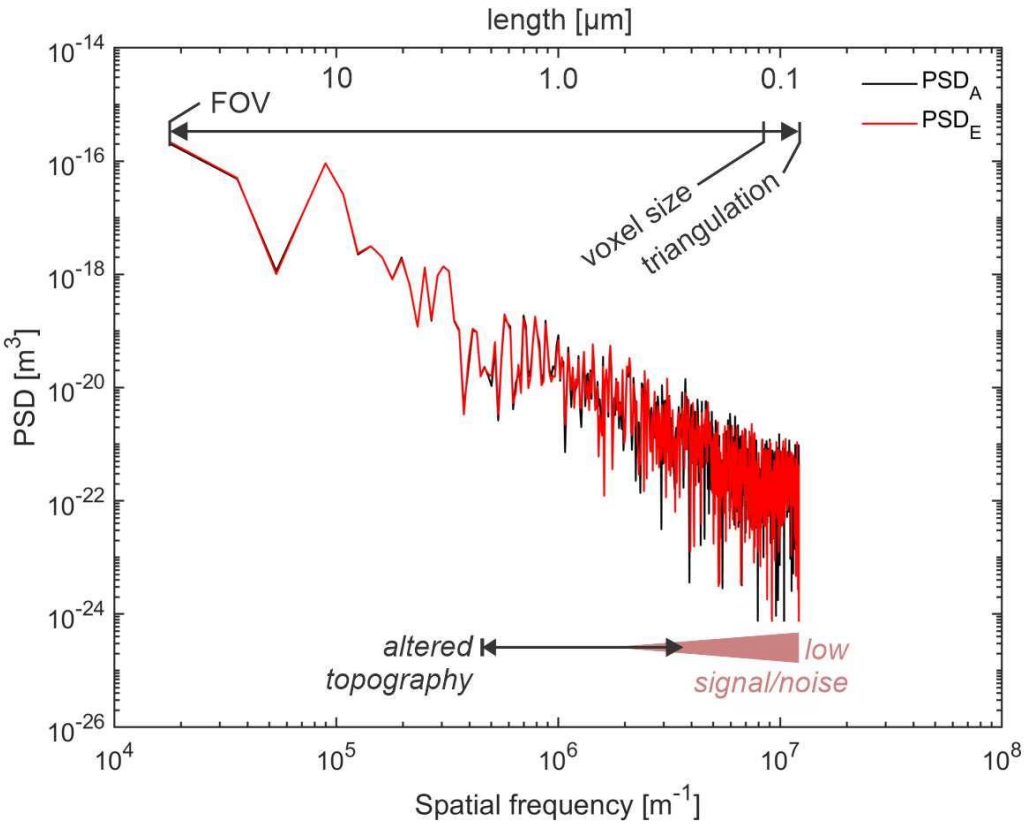

Figure 2-9: Comparison of the PSD curves of the initial (black) and modelled (red) surface. Calcite precipitation reduces the roughness of surface building blocks < ~ 5µm.

Within the MAGIC project, HZDR developed a pore-scale reactive transport mode for describing the coupled processes of flow, multi-component transport, microbially induced calcite precipitation, and evolution of the solid surface. The developed model is validated using published experimental data and ready to be used for the interpretation of the experimental results of biofilm growth to be obtained in the project. The numerical experiments focus on fluid flow through a 2D channel with a rough surface. The numerical results show that heterogeneous calcite precipitation causes a generally decreased surface roughness under advection-dominated and transport-limited conditions. Moreover, the results of power spectral density analysis demonstrate that microbially induced calcite precipitation affects surface topography both through general changes in surface roughness over the entire spatial frequency range (trend of fractal dimension change) and via local modifications in surface topography in the micron wavelength spatial frequency range. Sensitivity studies clearly show that uniform and non-uniform types of precipitation can be caused by different flow rates. Such different types of precipitation lead to different surface shapes. Quantitative insights into the evolution of surface height under different flow and reaction conditions provide a comprehensive understanding of surface evolution by microbially induced calcite precipitation at the pore scale. This has implications for enhanced predictability of contaminant transport in the subsurface with microbial activities at the core scale and beyond.

It is foreseen to compare with the simulation results on topography evolution with the measurements conducted in a complementary experimental study.

2.4 Thermodynamics & kinetics of mineral surface reactivity at pore scale

Different model models can be applied to describe dissolution kinetic dissolution of CH at the pore-scale. For the LB simulations described in section 2.2 dissolution was modelled based on the transition state theory (Lasaga, 2014), where R is the portlandite dissolution rate depends on the reaction kinetic constant (k), the reactive surface area (A) and the saturation ratio (ω), according to Equation 2.9:

$$R = kA(1 - \omega) \qquad (2.9)$$

Johanssen and Rademacher (1999) reported the reaction kinetic constants between $0.39 \cdot 10^{-4}$ and $6.2 \cdot 10^{-4}$ mol/(L·s·m^2). These measured values depend on the solution volume used in the experiment. Wang et al. (1998) reported reaction kinetic constants independent of the solution volume, equal to $5.4 \cdot 10^{-4}$ mol/(s·m^2), which would be consistent within the values reported by Johanssen and Rademacher (1999) assuming a solution volume close to 1l. Galan et al. (2015) reported a value of 0.0233 mol/l for the saturation concentration and $1.17 \cdot 10^{-10}$ m^2/s for the diffusivity of the dissolved Ca ions. The saturation ratio ω equals 1 when the concentration of the solution equals the saturation concentration. At this point the solid is at equilibrium and net dissolution reaction rate is equals zero. When the solution in contact with portlandite becomes undersaturated due to diffusive transport of CaOH ions away from the reacting interface, the dissolution reaction resumes with a rate given by Equation (2.9).

For more complex simulation scenario, where the dissolution and re-precipitation of C-S-H phases is considered, the chemical speciation and thermodynamic calculations are based on surrogate models for the sake of computational efficiency. Surrogate models are trained using the GEM-Selektor [11] for creating the training and test datasets.

To investigate mineral surface reactivity, PSI used the LBM code described in Section 2.2 to model the effect of microbial microorganisms on the cement-clay interface. The microbial microorganisms, which are investigated by HZDR, are incorporated in the code as a different reaction rate depending on whether they consume or produce Ca and Si. An increase or decrease in the reaction rate has the potential of changing the concentration field within the domain, and by extension, the removal sequence of the solid CH nodes. This would then change the material properties of the cementitious materials if the results were to be upscaled.

According to Equation 2.9 the reaction rate is controlled by reactive surface area and the degree of saturation. These parameters depend on transport processes, effective surface area and microbial activity. Preliminary tests, investigating the increase/decrease of the reaction rate by 10^2 or 10^{-2} respectively (see Figure 2-1).

Consideration of increasing dissolution rate while keeping the same time step in the reactive transport simulation is challenging. Fast dissolution rate results may result in an under-resolved simulations and the concentration overshooting the saturation point. Accordingly, LB time step should be controlled by the dissolution rather than the diffusion process. Such consideration are particularly important for the consideration of enhanced reactivity caused the microbial activity.

For the decreasing reaction rate, the subsequent transition of solid to fluid nodes naturally occurs at a much slower rate. At 300,000 steps, as shown in Figure 2-1, no such transition has yet occurred. That is because the amount dissolved is too low, not due to the concentration being near the saturation point (see Figure 2-1(a)). Indeed, as Figure 2-1(b) demonstrates, only a small portion of the CH concentration in the solid nodes has dissolved to the fluid field.

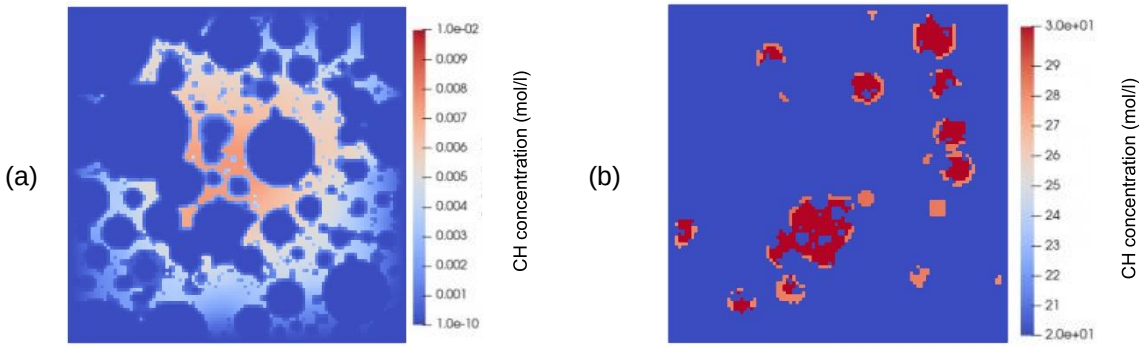

Figure 2-10: (a) CH concentration in the fluid and (b) Ca concentration in CH solid nodes after 300,000 steps for a 10^{-2}mol/(l·s) change in the reaction rate.

The LB model and simulations described above should be benchmarked against experimental data from ongoing experiments on cement paste degradation carried out by PSI/Empa as part of Subtask 3.1, which investigate the chemo-mechanical, microscopic and mineralogical characterisation of newly casted OPC and ESDRED mortar specimens. The specimens are exposed to an OPA pore solution at 40°C to accelerate degradation conditions and mimic the repository environment. In addition, data from 9-year aged mortars obtained from the Mont Terri experimental site (Jenni et al, 2014) are available, examined as part of Subtask 2.2. The LB code can use the specimens' microstructure, if available through X-ray tomography measurements, to replace the HYMOSTRUC generated domain. While the current domain reflects the composition and physical parameters such as porosity and diffusivity, as the domain is part of the code input, no internal changes will be necessary to begin new simulations. If the X-ray measurements are not of sufficient scale, composition data should be obtained through crystallographic studies and used with HYMOSTRUC to generate new representative domains.

2.5 Surrogate models for geochemical systems

Because of the complex nature of computations related to thermodynamic equilibrium and geochemical speciation calculations become a computational bottleneck in reactive transport modelling. Large computational demands arise from the multitude of species involved and the necessity to carry out chemical calculations at each mesh point for every time step. Consequently, the integration of the LB and geochemical solvers results in a poorly balanced code, with the majority of its computational resources spent 1n the thermodynamic modelling routines (Prasianakis et al., 2020). Moreover, it is worth noting that the time scales for chemical reactions and mass transport mechanics differ significantly.

To further model interactions such as C-S-H precipitation at a cement-clay interface, the LB code has been newly coupled with an artificial NN running on the GPU (which is at least one order of magnitude faster to single-core CPU NN computations) acting as a surrogate model for the native geochemical solvers.

The feedforward type of neural networks are used for the pore-level simulations. This is one of the simplest but most efficient network type, suitable for solving complex regression problems. The neural networks used in this study were obtained by a supervised learning approach in order to encode the thermodynamic equilibrium depending on the composition of the solution, with the data that GEMS provides. The mean squared error loss function is used. The right balance between the size of the network and its resulting accuracy was pursued. For that, several networks were tested, by varying the number of neurons per hidden layer, the number of hidden layers and the activation functions of the neurons. Moreover, several training algorithms were tested. It is noted, that a common issue in this type of networks is the element mass conservation between input and output of the networks, which can be an issue if not properly resolved. The architecture of the NN and typical performance against native geochemical solver is shown in Figure 2-11. The NN takes the total Ca and Si concentration expressed at $(Ca(OH)_2)_{aq}$ and $(SiO_2)_{aq}$ as input, provided by the LB code, as input. The output consists of multiple

phases including solids such as jennite and tobermorite in accordance with the CSHQ model (Kulik, 2011). NN training is done using the backpropagation technique (Rumelhart, 1986).

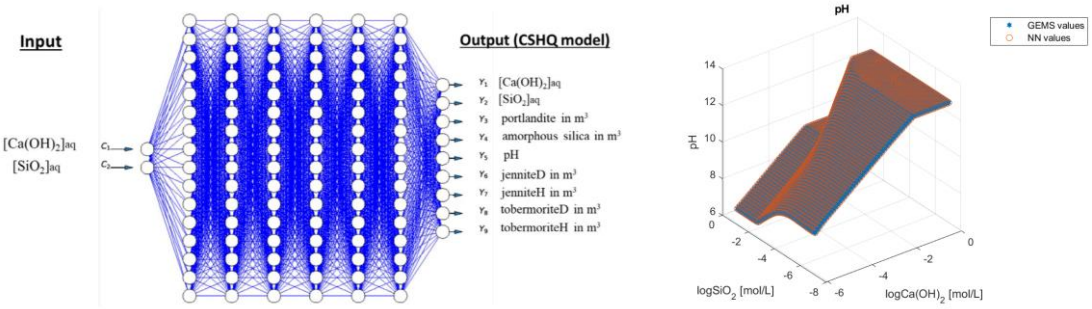

Figure 2-11: (left) A neural network model used for reactive transport simulations of leaching and C-S-H reprecipitation. Input is the species concentrations in solution and the output is the thermodynamic equilibrium of the C-S-H phases and the resulting aqueous species. (right) Graphical representation of the comparison of the neural network values (NN values, e.h. pH, red circles) vs the geochemical solver values (GEMS, blue stars). The two manifolds practically overlap.

The code is now capable of running on supercomputing parallel GPU clusters. The NN has been pre-trained through a sample of 90'000 pre-calculated simulations by geochemical modelling software GEM-Selektor in the case of C-S-H dissolution/precipitation reactions. The surrogate model with the selected dimensions is three to four orders of magnitude faster than the the full geochemical calculations performed with GEMS providing a large boost to the overall computation time (Prasianakis et al., 2020).

In summary, several pore scale simulations models have been developed to predict the microstructure evolution of cement phase. These models include leaching and carbonation phenomena caused by interaction with the formation pore water and consider possible microbial effects on carbonation processes. The models provide time and space resolved microstructures used in the simulations of mechanical properties of degraded cement paste and upscaling as described in the following sections.

3. Micromechanical models for effective elastic properties

Similar to most engineering materials, concrete materials are heterogeneous composite materials with complex and multi-scale microstructures. It is well known that their macroscopic performance is closely related to the composition and evolution of microstructures. Based on experimental data, numerous macroscopic models have been developed to describe the mechanical behaviour of concrete. However, in general, these models do not establish explicit connections between macroscopic properties and microstructural parameters. To overcome this limitation, micro-mechanical approaches have been developed to estimate the macroscopic mechanical properties of concrete composites by considering microstructural parameters and constituent properties as the basis. Broadly speaking, these approaches are either based on numerical homogenisation or analytical models. Without providing an exhaustive list of all these models, several most fundamental ones are listed here. These are the Voigt and Reuss bounds, the Mori-Tanaka estimation (Mori and Tanaka 1973; Benveniste 1987), the Hashin and Shtrikman bounds (Hashin and Shtrikman 1963), the self-consistent scheme (Qu and Cherkaoui 2006), and the differential scheme (McLaughlin 1977), which are used to study the effective elastic properties of materials. Moreover, by employing nonlinear homogenization techniques, several analytical strength criteria (void ratio and shape, void nucleation rate, yield) have been established for heterogeneous materials containing pores and inclusions at different scales (Maghous et al. 2009; Shen et al. 2013; Shen et al. 2017; Shen et al. 2020b). Based on these criteria, full elastic-plastic models that consider hardening or damage effects have been developed (Shen et al. 2012; Bignonnet et al. 2016; Shen and Shao 2016; Shen et al. 2020a; Aldakheel 2020). However, limitations of these analytical models have been clearly shown for materials with a large contrast in constituent properties, or a high volume fraction of aggregates. On the other hand, various types of numerical homogenization methods have been developed to predict the macroscopic responses of materials with complex microstructures (Cao et al. 2018a; Cao et al. 2018b; Cao et al. 2020). Commonly used numerical methods for full field simulations of concrete RVE include finite element method (FEM), finite difference method (FDM). However, numerical homogenization methods usually require significant computational costs. Recently, machine

learning-based methods have also been applied to the multi-scale mechanical modeling of concrete (He et al. 2022; Liu and Lu 2022). In this cutting-edge domain, researchers have started exploring how to leverage machine learning (ML) techniques to enhance the prediction and analysis of concrete properties. Particularly, Artificial neural networks (ANNs) have been widely utilized for establishing predictive models of concrete's mechanical properties. ANNs, a powerful ML tool, emulate the connectivity and information transmission among biological neurons, learning the complex relationships between inputs and outputs through training data. In this section, our focus is to provide a detailed introduction to the multi-scale mechanical model based on ANN that we have developed for studying the effective mechanical properties of concrete. Several studies conducted in WP-MAGIC aims at establishing connections between microstructural parameters, material composition characteristics, and macroscopic mechanical properties, enabling accurate predictions of concrete performance. This approach significantly improves the predictive power and accuracy of the model, while also efficiently completing complex mechanical modelling within a condensed temporal framework.

3.1 Numerical homogenization of elastic properties

The micromechanical models are used to estimate effective properties of a heterogeneous material, whatever the spatial scale. The subject is rather mature when it comes to estimating elastic properties of concrete using either analytical or numerical homogenization. The state of the art report "*Deliverable 16.1: MAGIC - T1 - Initial State of the Art on the chemo-mechanical evolution of cementitious materials in disposal conditions*" covers general idea and applications of homogenization in the context of cement paste and concrete. This section provides a minimum treatment of the theoretical aspects of numerical homogenization used for estimating Young's modulus and Poisson's ratio in the course of the MAGIC project.

In principle, the equation of motion is solved, assuming no body forces applied:

$$\boldsymbol{\nabla}.\boldsymbol{\sigma} = \mathbf{0} \tag{3.1}$$

where $\boldsymbol{\sigma}$ is the Cauchy's stress tensor. The linear elastic constitutive law is given by:

$$\langle \boldsymbol{\sigma} \rangle = \langle \mathbf{D}^{\mathrm{eff}} \rangle : \langle \boldsymbol{\epsilon}_{\mathrm{el}} \rangle \tag{3.2}$$

where, $\mathbf{D}^{\mathrm{eff}}$ is the effective stiffness tensor, which is to be determined, $\boldsymbol{\epsilon}_{\mathbf{el}}$ is the elastic strain tensor (e.g. Hain and Wriggers, 2008). The Macaulay brackets is given by:

$$\langle \cdot \rangle = \frac{1}{|\mathrm{V}|} \int_{\mathrm{V}} \cdot \, d\mathrm{V} \tag{3.3}$$

where V is volume of the representative volume element (RVE). Linear displacement boundary condition is applied to the RVE to solve Equation (3.1)). Note that for the linear displacement boundary condition to be valid, the elements on the boundaries of the RVE must have homogeneous properties, which is not the case with cement microstructures. Therefore, a window technique is applied as described in Hain and Wriggers (2008).

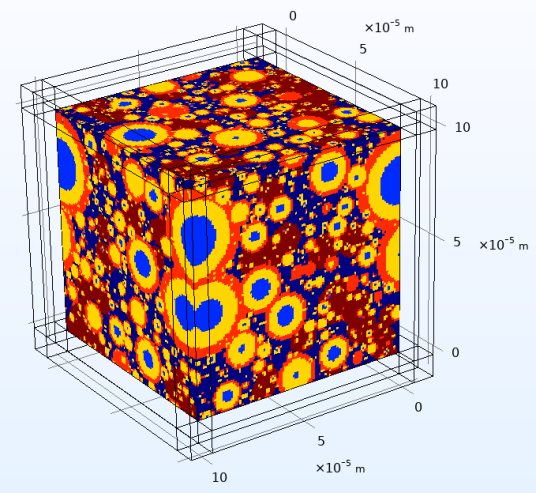

Figure 3-1: Illustration of the window around the RVE for iterative solution of linear elasticity equation with respect to effective material properties.

Hydration of ordinary Portland cement typically produces various hydrated phases and left behind some unhydrated clinkers. The dominant phases by volume are typically portlandite (CH), calcium silicate hydrates (C-S-H) and pores. The remaining noticeable phases include monosulfates (AFm), Ettringite (AFt) and unhydrated clinkers. In this study, only CH, C-S-H, micropores and unhydrated clinkers are considered for homogenization of elastic properties. In particular, two C-S-H phases are explicitly represented: high density C-S-H (HD C-S-H) and low-density C-S-H (LD C-S-H).

Cement paste microstructures can be categorized as non-periodic microstructures given random distribution of different hydrated and unhydrated phases, microcracks and air voids. This also implies that the cement microstructure can have infinite number of various arrangements of the phases within a representative volume element. Ideally, at least few tens of microstructural realizations are needed for a quantitative analysis of the uncertainties in the calculations of effective material properties. Due to the computational burden related to the 3D reactive transport simulation of the microstructrure evolution the analysis carried out in this project uses just one realization to obtain one possible solution amongst a family of solutions. The computational burden not only arises from the number of realizations of microstructures but also because of the number of iterations using the window technique that has to be carried out for each realization and for each degradation state of the material, moreover, for two different degradation mechanisms.

In the conducted study, the RVE size of 100×100×100 μm^3 is considered and a window of 10 µm is introduced all around the domain as shown in Figure 3-1. To address the scalability of the results we note that a much smaller RVE has been shown to be sufficient for a typical OPC cement microstructure (Saeid, 2021). For all analysis reported here, the RVE is discretized into 1 M hexahedral elements and solved using a finite element method.

The principles of numerical homogenization for concrete remains same as hardened cement paste described above, except the components of concrete differs. These include homogenized cement paste, interfacial transition zone (ITZ), air voids and aggregates. In this study, only aggregates and homogenized cement paste matrix are considered. Future refinements should incorporate air voids for estimating the elastic properties. ITZ may become important for estimating strength properties, which will not be addressed with numerical homogenization.

Typically, the volume fraction of construction concrete is in the range of 60-70% with various aggregate size distribution defined by a certain sieve curve. As the aggregates are treated as spherical inclusions in this study, it is impossible to embed all aggregate sizes respecting the sieve curve. Thus a step wise concrete RVE has to be built, which is elaborated in Section 5. Similar to numerical homogenization of

cement paste, here also the window technique is used in order to respect linear displacement boundary condition as the materials on the boundaries are not necessarily homogeneous.

Numerical homogenisation of elastic properties described above is conducted for a 3D representation of mineral phases and pores within the material on a grid. Such a presentation can either be measured (e.g. x-ray CT) or simulated by a numerical model. Several numerical models are available for the description of hydrated cement paste such as CEMHYD3D (Bentz, 2005), HYMOSTRUC3D (Gao et al. 2019), etc. are available. The structure obtained with such a model can either be directly used for the analysys of chemomecanical properties of cement and concrete or used is initial condition doe the reactive transport simulation with a consequent chemo mechanical analysis. In this study, HYMOSTRUC3D model has been applied. Theoretical details of HYMOSTRUC3D can be found elsewhere (Gao et al. 2019). HYMOSTRUC3D is typically used to generate synthetic microstructures with a maximum voxel size of 1 µm. Resolution smaller than this is possible, however, it introduces huge computational burden. Therefore, pore sizes less than 1 µm is not represented and is lumped in the properties of C-S-H phase.

Note that HYMOSTRUC3D is only used to generate synthetic microstructure of a sound material. With the initial microstructure, the microstructure of leached or carbonated material is achieved via a pore scale reactive transport model or randomly generated microstructure mimicking a specific degradation state of the material.

3.2 ANN-based Model for elastic properties of concrete

The elastic modulus is a fundamental mechanical property for the design and analysis of concrete structures. Many experimental and theoretical studies have been conducted on various types of concrete materials (Wang et al. 1988; Vilardell et al. 1998; Carrillo et al. 2019; Kanthe et al. 2022). As a composite material, the macroscopic elastic property of concrete is closely dependent on the mineral composition and the local elastic properties of constituents such as cement paste and aggregates (Garboczi and Bentz 1997; Bernard et al. 2003; Li and Metcalf 2005; Duplan et al. 2014; Zheng et al. 2006). On the other hand, the interfaces between aggregates and cement paste has different, usually weaker, mechanical properties. There exists an interface transition zone, commonly called interface transition zone (ITZ), which generally has a higher porosity and lower elastic stiffness and strength than the surrounding cement paste. The macroscopic mechanical properties of concrete materials can be significantly affected by the presence of ITZ (Li et al. 2003; Nadeau 2003; Baji et al. 2019; Liu et al. 2018). In order to evaluate the ITZ effect on the macroscopic elastic properties of composites, several efforts have been made to formulate of analytical models by using different homogenization techniques. For instance, by applying a generalized self-consistent scheme (GSCS), the so-called Hashin model has been established (Hashin and Monteiro 2002). This model is used as a reference work for the incorporation of ITZ effect in macroscopic elastic properties of different types of composites. Christensen et al. have determined the effective bulk modulus of three-phase composites based on the Eshelby's equivalent medium theory (Christensen 2012). Ramesh et al. have applied the appropriate stress and displacement conditions to the four-phase sphere model to determine the effective elastic modulus of concrete materials (Ramesh et al. 1996). There are many other extensions, by accounting for the aggregate gradation (Garboczi and Bentz 1997; Nadeau 2003), by considering spherical aggregates(Zheng et al. 2012; Herve et al. 2010). However, limitations of these analytical models have been clearly shown for materials with a large contrast in constituent properties, or a high volume fraction of aggregates(Dunant et al. 2013; Idiart et al. 2009; Das et al. 2016). Figure 3-2 compares the results of the Hashin, Christensen, and Ramesh models in predicting the elastic modulus of concrete (E_{itz}, E_{hom}, E_m, E_{agg} stands for Young's modulus of interface transition zone (ITZ), homogenised medium (hom), matrix (m) and aggregates(agg), respectively). According to these three analytical models, for a given cement matrix, the macroscopic elastic modulus of concrete composite increases when the stiffness of aggregates or ITZ is higher. More precisely, with a constant E_{itz}/E_m, the value of E_{hom}/E_m increases with E_{agg}/E_m. In particular, when E_{itz}/E_m = 0 (right Figure 3-2), the aggregates are debonded from the cement matrix. As a consequence, the macroscopic elastic modulus should not be affected by

the stiffness of aggregates. This physical phenomenon is correctly reproduced by the Ramesh model, but not by the two other ones. In particular, the Hashin model still provides a large effect of aggregates. Based on these results, it seems that the Ramesh model provides a more reasonable estimation of macroscopic elastic modulus than the Hashin and Christensen models. Furthermore, the numerical results based on FFT are then compared with the analytical predictions by the Ramesh model and presented in Figure 3-3. It is found that although the general evolution trend of macroscopic modulus is similar, there are significant quantitative differences between the analytical model and numerical solutions.

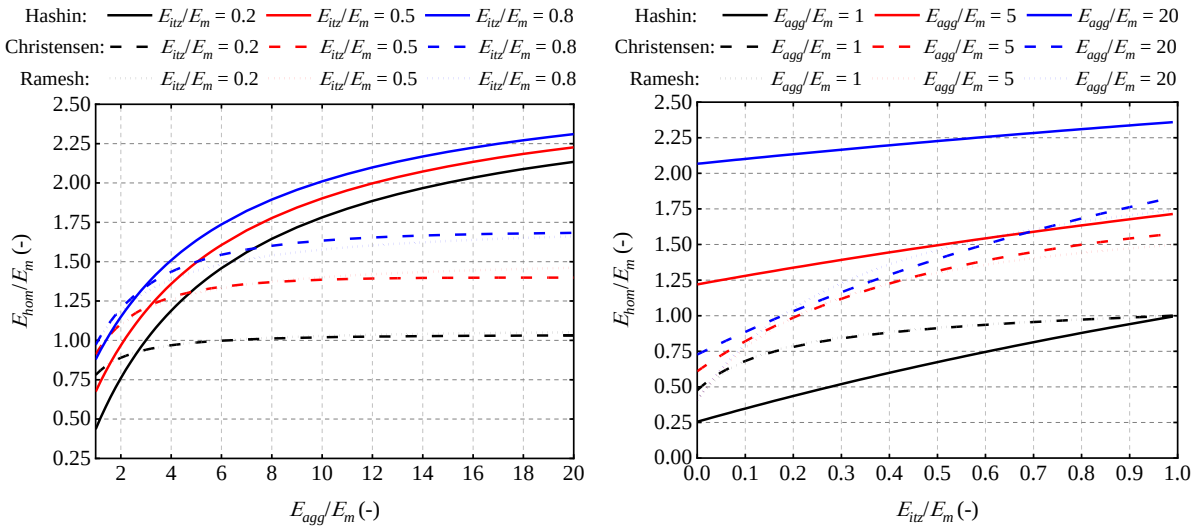

Figure 3-2: Variations of relative macroscopic Young's modulus $\mathrm{E_{hom}/E_m}$ as functions of E_{agg}/E_m and E_{itz}/E_m: comparisons between three analytical models.

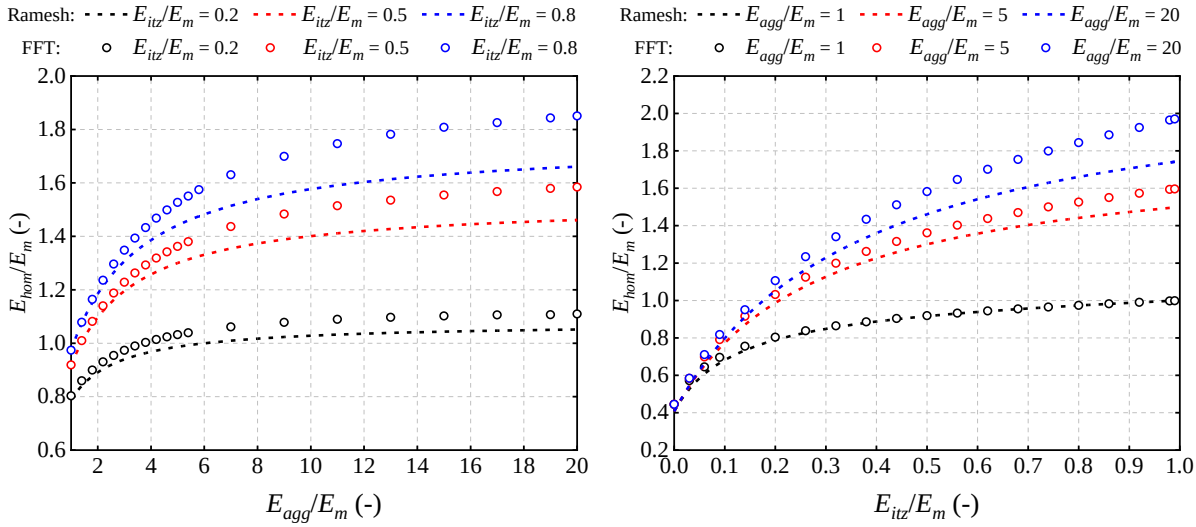

Figure 3-3: Evolution of normalized effective Young's modulus respectively with E_{agg}/E_m and E_{itz}/E_m: comparisons between numerical results and Ramesh model's predictions.

The FFT-based model is able to explicitly consider various kinds of microstructures by performing direct numerical simulations. But this approach requires a high computing time and its application to real materials and problems is not easy. It is here used for not only investigating impacts of microstructure on macroscopic elastic properties, but also to construct a representative dataset. With such a dataset, it is possible to develop an ANN-based model. After training and validation, the ANN model is able to

provide macroscopic properties without needing heavy numerical calculation. Moreover, the ANN model can also be used for the optimization of material. For example, what type of mineralogical composition should be used for get desired macroscopic properties.

The ANN model for concrete composite is built and trained with the widely used platform Keras and the TensorFlow is employed to solve the regression problem. The trial-and-error method is adopted to determine the architecture of the ANN model. Since the inputs and outputs of the model are already determined, only the structure of hidden layers needs to be chosen, i.e., the number of hidden layers and that of neurons per layer. For this purpose, we have considered 16 different models, respectively composed of 1, 2, 3 and 4 hidden layers, and with 50, 100, 150 and 200 neurons per layer. The 16 models are initially trained by using 2916 data sets (2187 for training, 729 for test). In Figure 3-4, we show the comparison of root-mean-square error (RMSE) between 16 different models after 100 epochs. One can see that although in general the accuracy of ANN model increases with the number of hidden layers and neurons in each layer, it is not systematically observed. For example, for the models with 150 neurons per layer, the value of RMSE becomes stationary. after the use of three hidden layers. Therefore, it seems that the model with 3-layers×150-neurons represents an optimal choice. Based on this analysis, the ANN model selected for estimating the elastic properties of concrete composites is shown in Figure 3-5. The corresponding hyper-parameters of the model are given in Table 3-1.

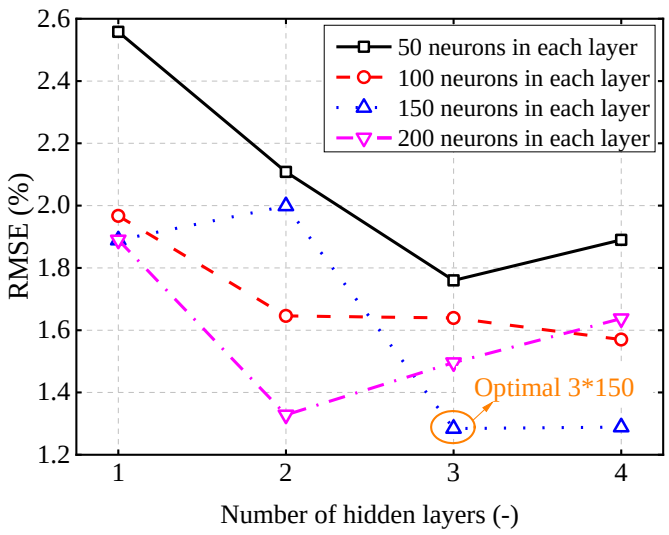

Figure 3-4: Comparison of root-mean-square error (RMSE) between 16 different neural architectures after 100 epochs.

Table 3-1 Hyper-parameters of the artificial neural network model for prediction of bulk(κ) and shear (μ) moduli κ_{hom}/κ_m and μ_{hom}/μ_m, of homogenized medium (hom) and matrix (m), respectively.

Input layer	Hidden layers	Output layer	Loss function	Optimizer
f_{agg},κ_m, μ_m, κ_{itz}/κ_m, μ_{itz}/μ_m, f_{itz}	3-layers × 150-neurons × ReLU	κ_{hom}/κ_m, μ_{hom}/μ_m	MSE	Adam

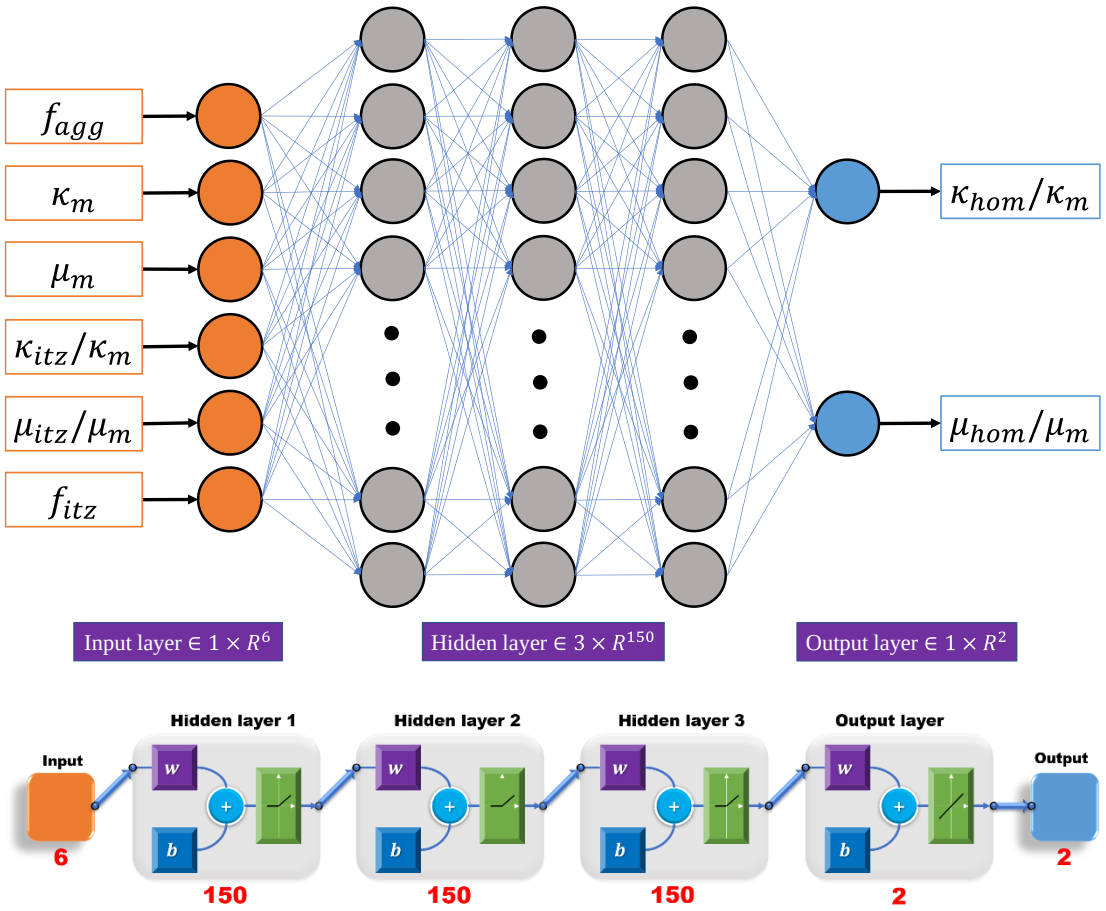

Figure 3-5: An ANN model for evaluating κ_{hom}/κ_m and μ_{hom}/μ_m of concrete containing ITZ.

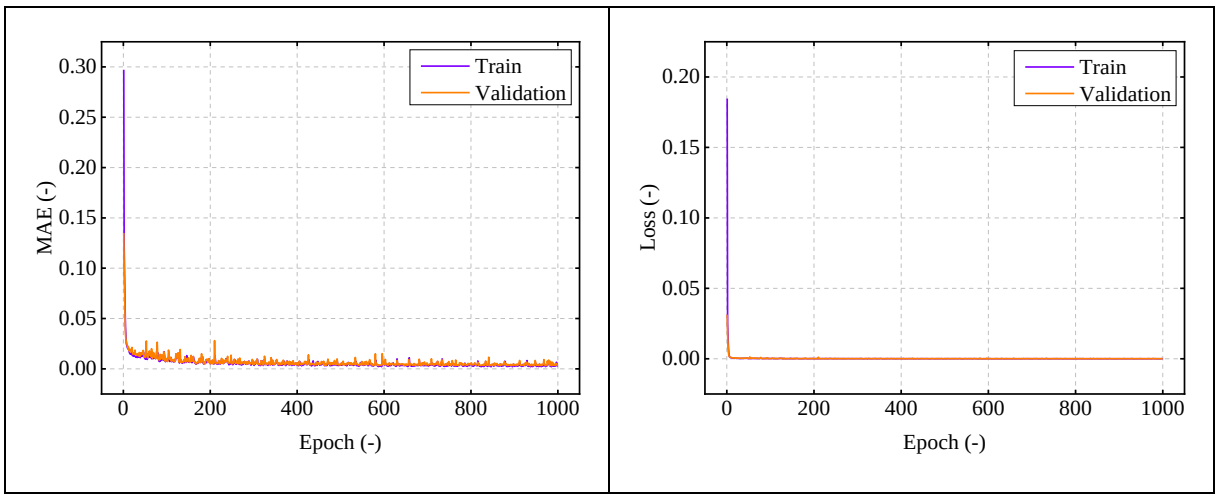

Figure 3-6: Mean absolute error (MAE) and loss function evolution during training process.

The variations of the loss function and mean absolute error (MAE) with epoch number are presented in Figure 3-6, for both training and validation sets. It can be seen that the proposed ANN model converges very fast. After a small number of continuous learning and self-adjustment of the network, the loss

function and MAE value decrease rapidly. The final values of MAE and loss function are 3.07 × 10^{-3}, 1.7211 × 10^{-5} for the training dataset and 3.51 × 10^{-3}, 3.00744 × 10^{-5} for the validation one. The relatively small difference between the results of the train and validation sets indicates that the model is not over-fitting. Furthermore, to quantitatively illustrate the correlation between the experimental and predicted value, for the whole test dataset (729 sets), in Figure 3-7, one presents the correlations between the predicted values and the exact ones. The fitted line matches the ideal fit line and has a high value of R^2 (0.99927 for κ_{hom}/κ_m and 0.99964 for μ_{hom}/μ_m). These results demonstrate the high accuracy of the proposed ANN model in the prediction of κ_{hom}/κ_m and μ_{hom}/μ_m. The predicted variations of κ_{hom}/κ_m, μ_{hom}/μ_m and E_{hom}/E_m as functions of κ_{agg}/κ_m, μ_{agg}/μ_m and E_{agg}/E_m as well as of κ_{itz}/κ_m, μ_{itz}/μ_m and E_{itz}/E_m are shown in Figure 3-8. The results provided by the ANN model are compared with those obtained from the FFT-based direct simulations used here as the reference solutions. One can observe a very good agreement between the ANN and FFT models. It is seen that the output results of the ANN model are almost the same as those of the FFT direct simulations. All these results illustrate the very good accuracy of the ANN-based model.

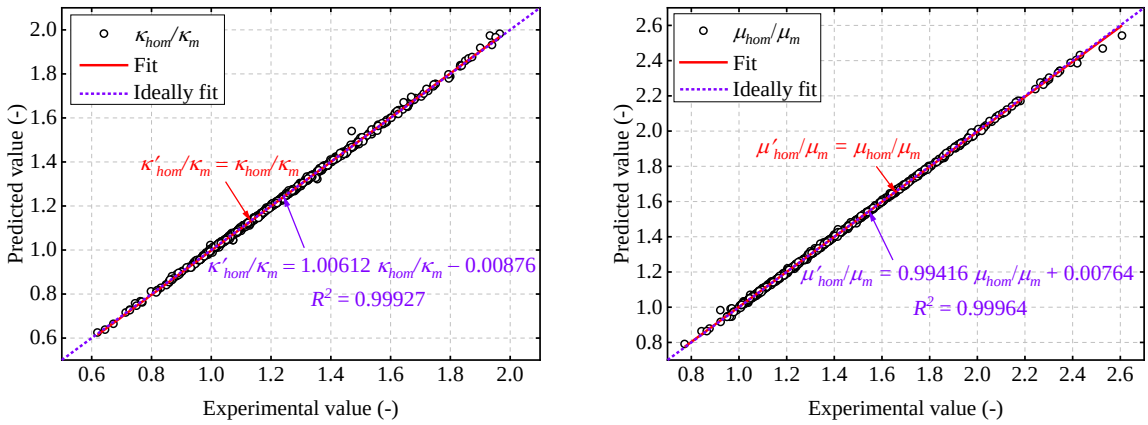

Figure 3-7: Correlation between predicted and experimental values of κ_{hom}/κ_m and μ_{hom}/μ_m

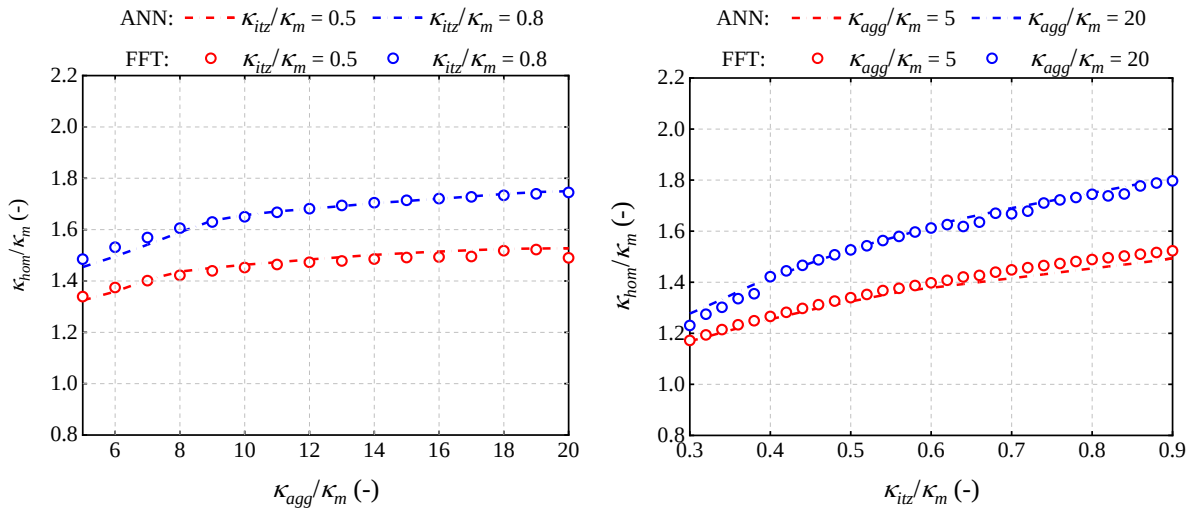

(a) Variations of effective bulk modulus κ_{hom}/κ_m with κ_{agg}/κ_m and κ_{itz}/κ_m

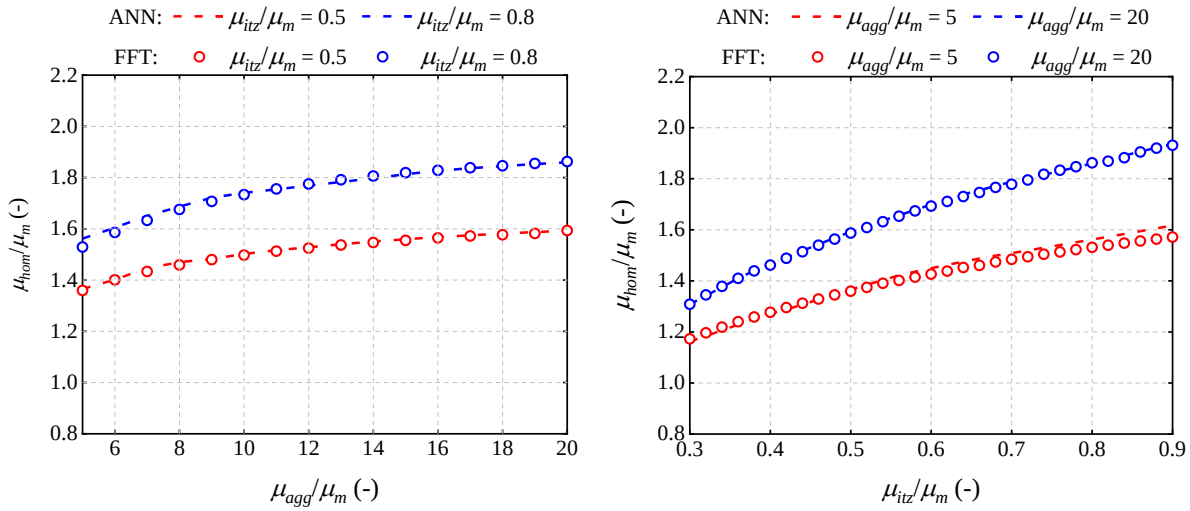

(b) Variations of effective shear modulus μ_{hom}/μ_m with μ_{agg}/μ_m and μ_{itz}/μ_m

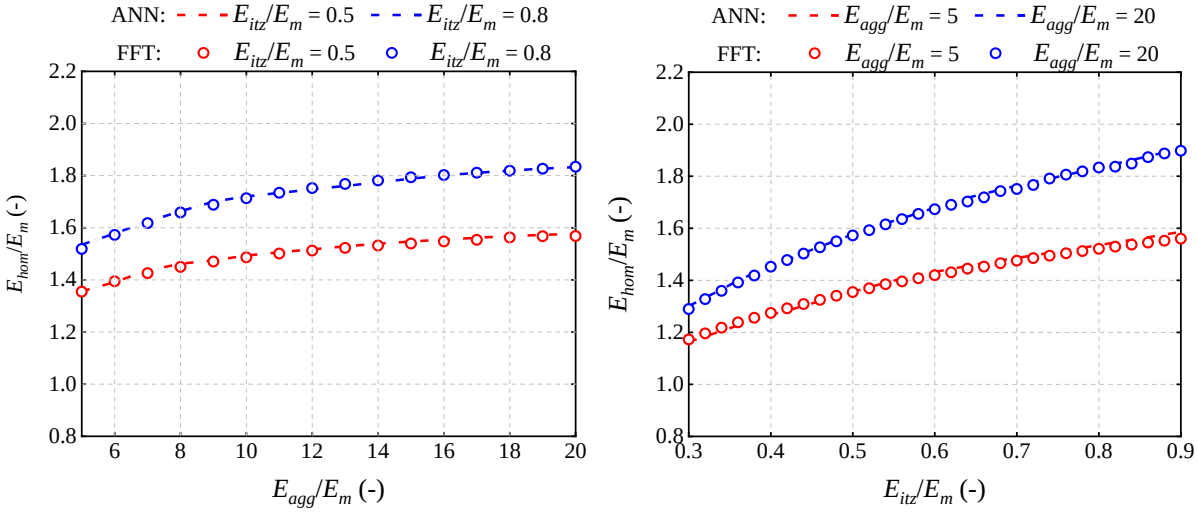

(c) Variations of effective Young's modulus E_{hom}/E_m with E_{agg}/E_m and E_{itz}/E_m

Figure 3-8: Comparisons between ANN-based model and FFT-based direct simulations.

3.3 ANN based model for strength of concrete

In the past few decades, significant advancements have been made in understanding the nonlinear behaviour of heterogeneous materials. In particular, various macroscopic strength criteria have been developed to assess the failure stresses of materials. However, establishing analytical strength criteria requires simplification of the microstructural morphology of concrete materials. For instance, attempting to derive an analytical strength criterion by considering pores, inclusions and ITZ at the same time poses significant mathematical challenges, which can lead to neglecting the effects of composition in the material in the study. Specifically, there is no analytical solution for the case where inclusions and pores co-exist at the same scale. On the basis of these analyses, an alternative matrix configuration is considered involving inclusions, where the matrix contains pores and inclusions at the same scale. By dividing the material into two scales, the matrix of the material conforms to the Drucker-Prager criterion at the microscopic scale. Applying this schema, an ANN-based model for evaluating the macroscopic strength of concrete was developed where the modelling data set was derived from FFT numerical simulations. As already mentioned for the elastic properties above, the FFT model is used to investigate impacts of typical microstructures on macroscopic strength on the one hand, and on the other hand for the construction of a representative dataset. The estimation of macroscopic strength with FFT model needs high computer cost. The ANN model can quickly provide macroscopic strength for a given input set. The ANN topology is shown in Figure 3-9. A distinctive feature of this model is its consideration of

the influence of porosity and inclusion volume fraction on the macroscopic mechanical properties of concrete-like materials. The performance of the ANN model was evaluated using various statistical metrics, demonstrating its high accuracy. Figure 3-10 displays a comparison between the normalized macroscopic strength surfaces of concrete materials obtained from the ANN model and the FFT numerical model. It is evident that the ANN model can successfully reproduce the results obtained from traditional numerical simulations.

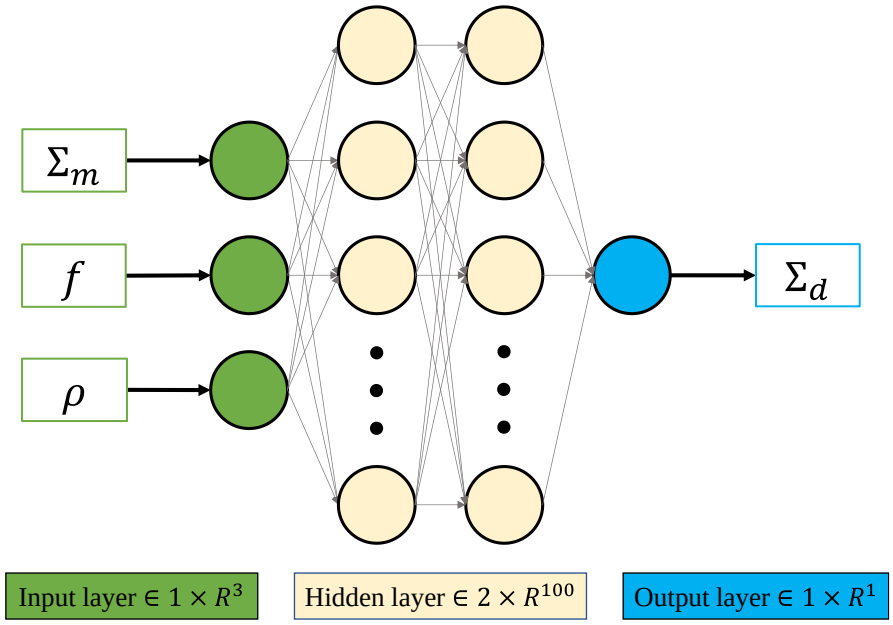

Figure 3-9: A BP neural network model to evaluate the macroscopic yield surface of concrete materials.

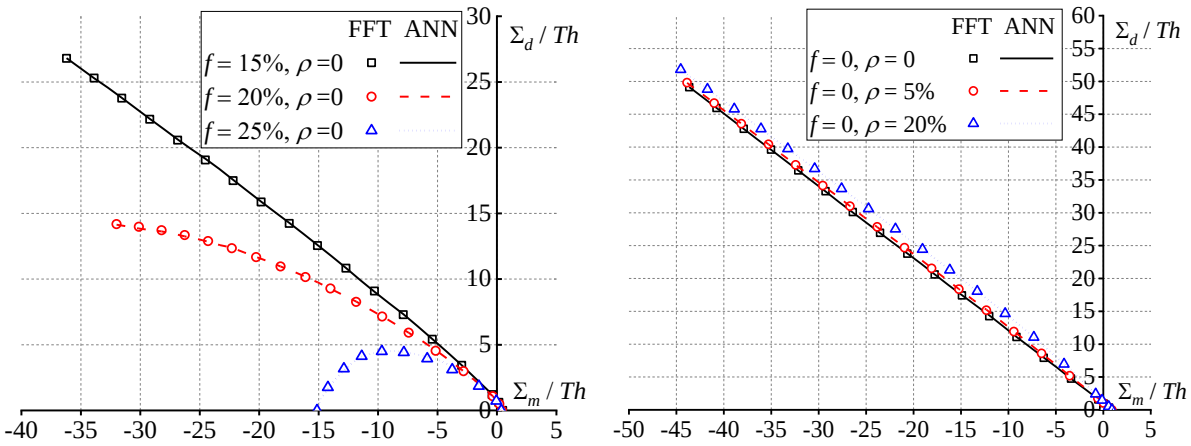

(a) Materials with only inclusion

(b) Materials with only pores

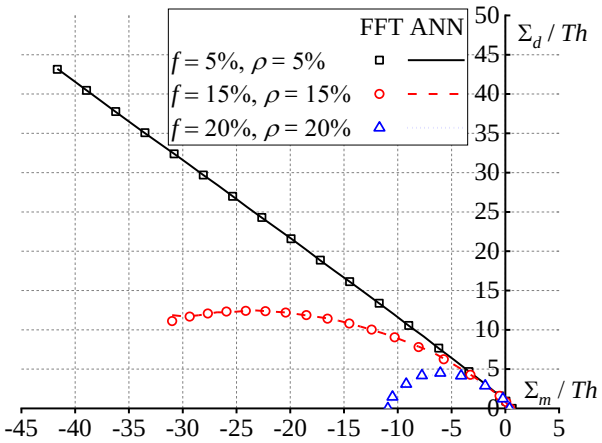

(c) Materials with both pores and inclusions

Figure 3-10: Variations of normalized macroscopic strength surface with porosity and inclusion fraction for concrete materials.

In summary, the available approaches and relationships between them can be classified as follow: (a) direct numerical simulations provide most accurate description of material properties for a given spatial phase distribution and their material properties based on the equations of continuum mechanics. These methods are computational demanding for complex system in terms of phase distribution and spatial resolution considered. (b) Homogenization techniques use volume averaging relationships between the phase composition and macroscopic propertied of the composite material. These relationships work well for materials with a simple microstructure (e.g. spherical inclusions in a homogeneous matrix) but may fail to accurately describe properties of more complex microstructures. (c) ML based approach uses efficient interpolation approach of data obtained by direct numerical simulation with a ANN. Such a model calibrated (trained) model are applied in the interpolation sense. Due to the computational performance, the ANN models are particularly efficient for inverse modelling and parameter sensitivity studies.

4. Upscaling

Concrete is a widely used construction material that is characterized by a high mechanical strength. Concrete has a complex structure consisting of amorphous phases with pore sizes of below nanometers, crystalline phases and clinkers at the micrometer scale, fine sands with sizes below millimeter and finally medium and coarse aggregates with sizes up to tens of centimeters.

Hardened cement paste consists of amorphous and crystalline phases resulting from a hydration process of clinkers. Hardened cement paste is a binding material that binds all other inclusion in concrete, for example aggregates, together and provides material strength. Due to this nature of material, concrete belongs to a large group of particle reinforced composites where each phase can be considered as random (Vorel et al., 2012). This property enable us to upscale physical properties into isotropic homogenized material. Processes of concrete alteration manifest themselves on different spatial scales. Chemical changes can be considered at the scale of solid phases in the material. Microstructure changes due to chemical alterations or mechanical stresses result in the changes of pore size distribution and consequently in physical properties, such as effective diffusivity and permeability. Mechanical damage, on the other hands happen possibly on larger scales (Vorel et al., 2012).

Because of wide range of length scales involved, it is practically impossible to include and analyze all phases with one large scale single experiment or numerical model. Previous work on the scaling of strength across hierarchically structured composite materials in the presence of defects with distinct morphology and origin within the microstructure has been studied on the level of the hardened cement paste (Hlobil et al., 2022). In this work the cement paste strength and its evolution due to chemical

changes has been studied separately in three levels, starting from pure hardened cement paste without any defects or inclusions, and then adding the level of microdefects and finally larger air voids.

The approach of several scale levels has been also adopted by (Drugan & Willis, 1996). They derived a variational formulation for a micromechanics-based, explicit nonlocal constitutive equation relating the ensemble averages of stress and strain for a class of random linear elastic composite materials. The report that the minimum representative volume element (RVE) size for the usual macroscopically homogeneous “effective modulus” constitutive models is at most twice the reinforcement diameter (or inclusion) to achieve a maximum error of 5% of the constant “overall” modulus term. For the error below 1% the size is 4.5 times the reinforcement diameter.

Based on these findings this work builds further on the upscaling of mechanical properties up to the concrete scale.

4.1 Upscaling of transport parameters

In particular, the evolved geometry can be used for retrieving correlations between parameters such as porosity, diffusivity and the local chemical composition. These correlations can then be applied at the macro-scale, for example at finite element codes to track phenomena happening within a single cell. Since the time evolution is calculated, such correlations may also be time-dependent or related to the degree of dissolution. For example, the increase in porosity with regards to the dissolution of a percentage of the solid nodes or the diffusion rate for certain porosities can be tracked.

In addition, the evolution of the chemical composition itself can be used for upscaling. The evolved geometry has different amounts of CH, C-S-H and unhydrated phases with a different porosity. These percentages can be extrapolated to larger volumes, which can then be used as REV for macroscale codes. The upscaled REV can have different mechanical properties (Young's modulus, compressive and tensile strength, etc.) reflecting the microscale phenomena.

PSI has stored the full data for each computational node at regular time steps for the simulations shown in Section 5. This data is saved in VTK files that can be easily viewed and interpreted using a post-processing program such as ParaView (Ahrens, et al., 2005). In particular, these files contain the Ca and Si concentrations of each node as well as an array distinguishing between solid, quasi-solid and fluid nodes. For the quasi-solid nodes, the liquid and solid concentrations are saved separately. This data forms an evolution timeline that will be used by the MAGIC partners at SCK-CEN and LAM3 to determine the mechanical properties of the evolved geometries.

The data can be useful for different environmental conditions, which can be reflected at different boundary conditions in the pore scale simulations. For example, different Ca and Si concentrations at the boundary can reflect the interactions with different clays. Moreover, changing the reaction rate can model conditions with different pH or temperatures.

4.2 Evolution of mechanical properties

The principles of numerical homogenization for concrete remains same as hardened cement paste described in Section 2.4, except the components of concrete differs. These include homogenized cement paste, interfacial transition zone (ITZ), air voids and aggregates. In this study, only aggregates and homogenized cement paste matrix are considered. Future refinements will incorporate air voids for estimating the elastic properties. ITZ may become important for estimating strength properties, which will not be addressed with numerical homogenization.

Typically, the volume fraction of construction concrete is in the range of 60-70% with various aggregate size distribution defined by a certain sieve curve. As the aggregates are treated as spherical inclusions in this study, it is impossible to embed all aggregate sizes respecting the sieve curve. Thus a step wise concrete RVE has to be built, which is elaborated in Section 5.

Similar to numerical homogenization of cement paste, here also the window technique is used in order to respect linear displacement boundary condition as the materials on the boundaries are not necessarily homogeneous.

5. Applications: Interpretation of experimental data and predictive modelling

5.1 Reference model for cement paste microstructure

Sections 3 and 4 describes the methodology applied for simulation of microstructure evolution and determination of elastic properties of cementitious material. Accordingly, the elastic properties of sound, leached and carbonated cement paste and concrete used for the experimental studies in WP MAGIC were estimated. The initial composition of the cement mix is provided in Table 5-1, including inputs needed by the HYMOSTRUC model. Since the objective of this project is to address chemical impact in the long term, it is recommended to compute microstructural state at maximum degree of hydration. Hence, in this study, the microstructural state is sought at 100 days, when the material is expected to reach close to metastable maximum degree of hydration. The volume fractions of the resulting hydrates, including unhydrated clinkers are presented in Table 5-2.

Table 5-1: Composition of the cement mix and general inputs to HYMOSTRUC model.

Parameter	Values
Material	CEM I cement paste
w/c	0.5
RVE size	100×100×100 μm^3
Voxels in the RVE	1,000,000
Density of clinkers	3.15 g/cm^3
Mass fraction of clinkers	
C3S	0.6538
C2S	0.1348
C3A	0.0819
C4AF	0.11
Gypsum	0.0196
Na2O	0.0031
K2O	0.0049

Table 5-2: Output from the hydration model.

Phases	Volume fractions
CH	0.144
HD C-S-H	0.337
LD C-S-H	0.235
Porosity	0.233
Unhydrated phases	0.051

The resulting microstructural arrangement is shown in Figure 5-1. Note that HYMOSTRUC model is based on particle growth kinetics assumption, which therefore yields a structure with concentric spheres. For the sake of simplicity, only major phases are considered in the microstructure for estimating the mechanical properties. AFt and AFm phases are in trace quantities and hence ignored. The resultant volume fractions are re-normalized to 100%. The light blue regions indicate anhydrated clinkers, the yellow regions indicate high density (HD) C-S-H, the orange region indicates low density (LD) C-S-H, the red regions indicate portlandite (CH) and the dark blue region indicates water filled micropores. Thus, the implicit assumption in this model is that the lowest pore size is 1 µm, which essentially captures the upper range of macropores in the commonly accepted nomenclature of cement chemistry. This also implies that when it comes to the choice of properties of individual phases, especially, the C-S-H phase property should be chosen such that the properties of the gel pores is reflected. In other words, at the microscale, the C-S-H is a composite phase. The mechanical properties of individual phases are presented in Table 5-3.

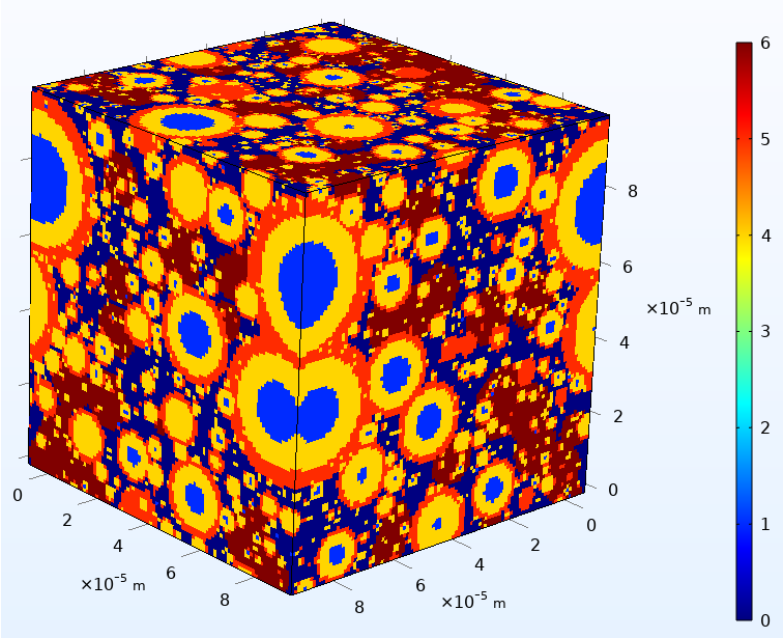

0: water filled micropore; 1: Unhydrated clinkers; 4: HD C-S-H; 5: LD C-S-H; 6: CH

Figure 5-1: Synthetically generated microstructure based on HYMOSTRUC model.

Table 5-3: Typical mechanical properties of the constituents of OPC microstructure.

Phases	E, Young's modulus [GPa]	ν, Poisson's ratio [-]
CH	42.3	0.305
LD C-S-H	21.7	0.24
HD C-S-H	29.4	0.24
Silica gel	2	0.35
Calcite	69.9	0.32
Unhydrated clinkers	135	0.3
Water filled porosity	3×10^{-6}	0.5

Leached calcium is estimated as shown in Equations below. Ca_{CH} is the calcium leached from CH, Ca_{C-S-H} is the calcium leached from C-S-H phase, V_f is the volume fraction and V_m is the molar volume of the phases and C/S is the Ca/Si ratio. During leaching or carbonation, the change in volume fraction of Ca is tracked, the remaining parameters are mineralogical constants as given in Table 5-4. The mechanical properties of the constituents of the microstructure are summarized in Table 5-3.

$$Ca_{CH} = \frac{V_{f,CH}}{V_{m,CH}} \tag{1}$$

$$Ca_{C-S-H} = C/S\left(\frac{Vf_{LD\ C-S-H}}{V_{m,LD\ C-S-CH}} + \frac{Vf_{HD\ C-S-H}}{V_{m,HD\ C-S-CH}}\right) \tag{2}$$

$$Ca_{CC} = \frac{V_{f,CC}}{V_{m,CC}} \tag{3}$$

Table 5-4: Mineralogical data.

Parameters	Values
$V_{m,CH}$	3.3×10^{-5} m³/mol
C/S	1.7
$V_{m,LD\ C-S-CH}$ (*)	1.07×10^{-4} m³/mol
$V_{m,HD\ C-S-CH}$ (*)	1.07×10^{-4} m³/mol
$V_{m,CC}$	3.693×10^{-5} m³/mol

* Although the molar volumes of LD and HD C-S-H are different, for simplicity it is considered the same.

5.2 Impact of Ca leaching on the mechanical properties of cement paste

Figure 5-2 shows 2D cross sections of randomly generated microstructures for various degrees of Ca leaching starting from fully intact cement paste to fully leached state, when only silica gel and water filled pores exist. In the intermediate stages, it is assumed that leaching occurs sequentially with 50% of Ca in CH leached first, followed by 100% of Ca leached from CH, LD C-S-H and HD C-S-H. Note that Figure 5-2(d)-(e) also shows an additional phase identifier 7, which is the silica gel resulting from C-S-H dissolution.

Figure 5-3 and Figure 5-4 shows 2D cross sections of LB simulated microstructures of leached cement paste. Since only CH dissolution was considered in the LB simulations, only CH fractions are discussed. For demonstration, only two degradation states are shown representing approximately 25% (Figure 5-3) and 50% (Figure 5-4) Ca leached from CH at various depths from the boundary in the x-y plane of the microstructure. These are also compared with randomly generated structures for the same two degradation states. As far as the 25% leached state is concerned, both randomly generated and LB simulated microstructure resemble each other. However, this is not the case with 50% leached state, where the spatial differences are more significant. This is to be expected as LB simulations consider reactor transport of ions through the complex pore space.

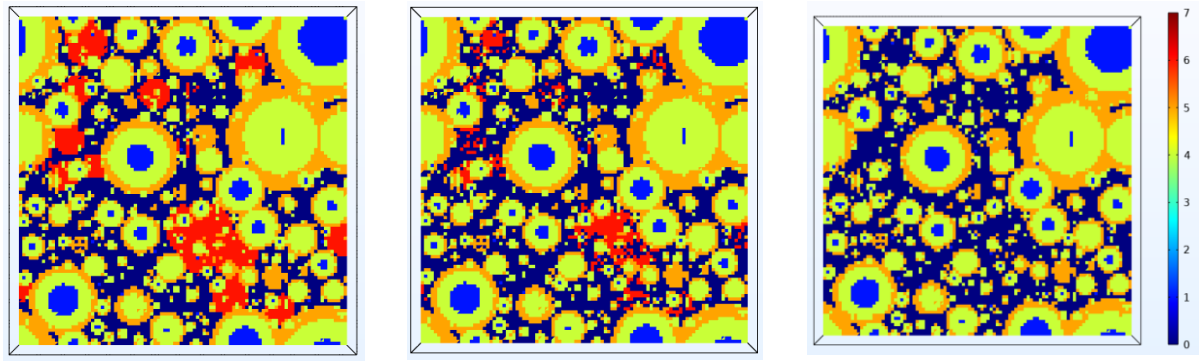

(a) Intact cement paste

(b) 50% CH dissolved

(c) 100% CH dissolved

(d) LD C-S-H dissolved

(e) LD C-S-H fully dissolved, HD C-S-H partially dissolved

(f) All C-S-H dissolved

0: water filled micropore; 1: Unhydrated clinkers; 4: HD C-S-H; 5: LD C-S-H; 6: CH; 7: Silica gel

Figure 5-2: Random generation of dissolution of cement paste microstructure.

Random microstructure	LB simulated microstructure
25% CH leached	
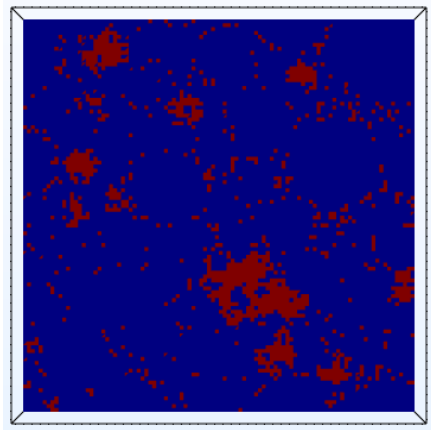 **Depth = 38 µm**	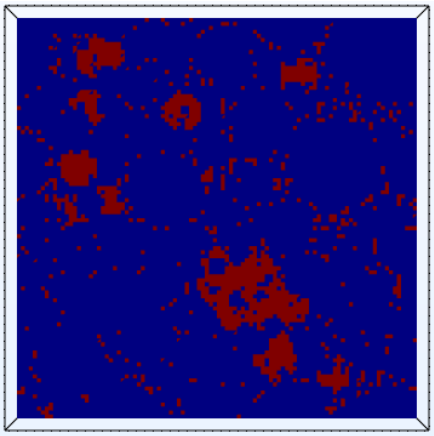 **Depth = 38 µm**
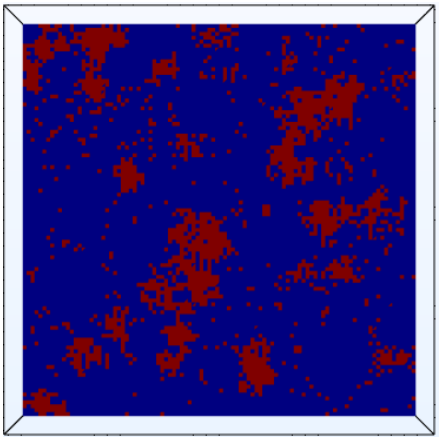 **Depth = 18 µm**	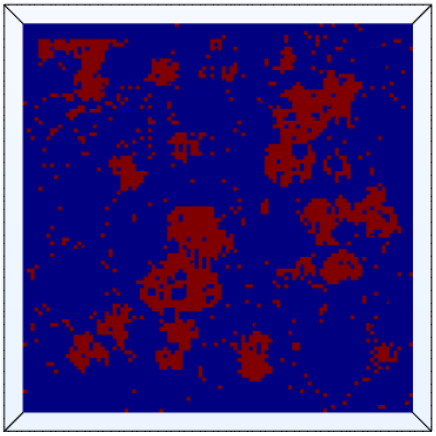 **Depth = 18 µm**
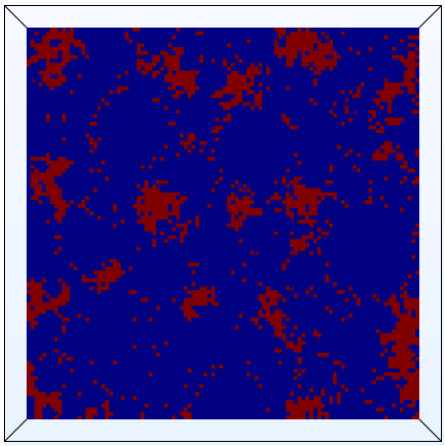 **Depth = 4 µm**	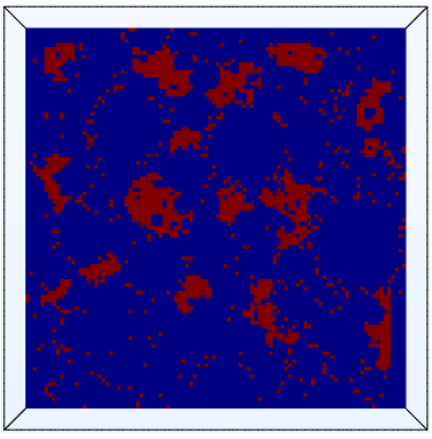 **Depth = 4 µm**

Figure 5-3: Comparison of randomly generated 25% CH leached microstructure with LB simulated microstructure.

Random microstructure	LB simulated microstructure
50% CH leached	
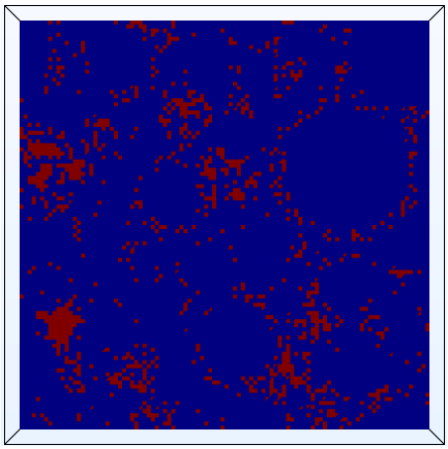	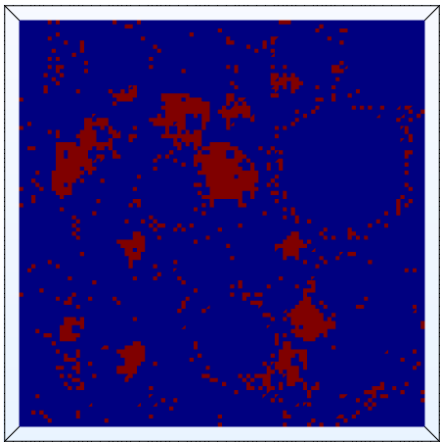
Depth = 38 µm	**Depth = 38 µm**
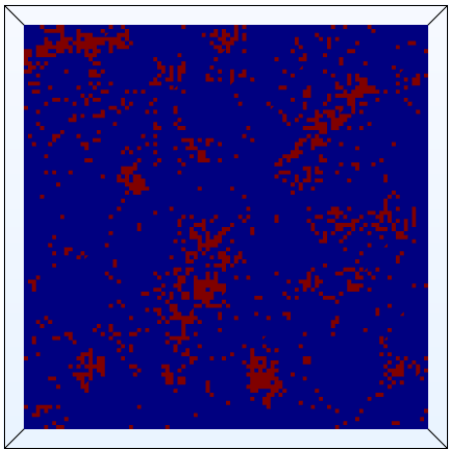	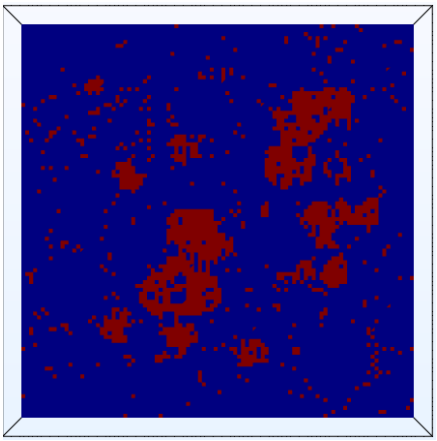
Depth = 18 µm	**Depth = 18 µm**
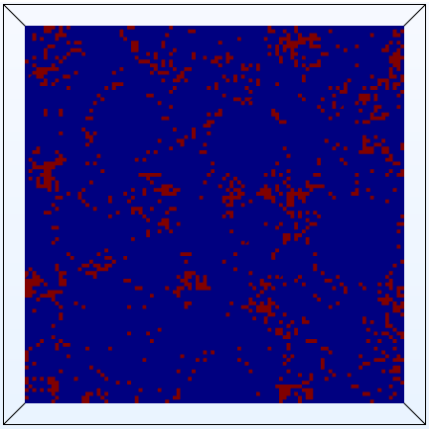	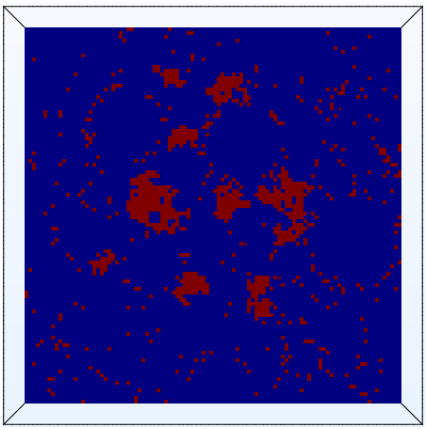
Depth = 4 µm	**Depth = 4 µm**

Figure 5-4: Comparison of randomly generated 50% CH leached microstructure with LB simulated microstructure.

Figure 5-5 shows homogenized or effective Young's modulus of cement paste as a function of mass % of Ca leached (Ca leached/total initial Ca in the microstructure RVE). The calculated effective modulus of sound cement paste is approximately 15.21 GPa. This is consistent with those reported in literature studies summarized in Table 5-5, which captures limited data set on CEM I material with W/C as close to 0.5 (this study) as possible. In fact, Table 7 predominantly covers numerical studies but with varying mix composition and possibly varying phase properties. With the exception of studies by Kamali et al. (2003) and Bernard et al. (2003), the modulus of sound cement paste is quantitatively in good correspondence with other studies. The decrease in the elastic modulus with increase in leaching degree is also consistent with experimental observations. Limited numerical and experimental studies exist for CH leached state only as shown in Table 7. This study yielded 7.28 GPa when CH is fully leached, which is close to those reported by Kamali et al. (2003), Gallé et al. (2004) and Yu and Zhang (2015).

Figure 5-5 also shows a comparison of effective modulus based on randomly generated microstructures and those generated by the LB simulations for 3 different degradation states, which are 25%, 50% and 75% CH leached states. The effective modulus obtained on the basis of LB simulations are in good correspondence with the randomly generated microstructure. This reveals that for the elastic modulus, the spatial distribution of leached zones are not that sensitive, at least at the microstructural scale. In other words, mere knowledge of volume fractions of different phases suffices to reasonably estimate the effective modulus of the material. This also explains why analytical homogenization techniques are generally successful in estimating the effective properties such as elastic modulus, diffusivity and conductivity, where RVE exists. To test this, analytical homogenization results based on Mori-Tanaka scheme have been superimposed in Figure 5-5 (Mori and Tanaka (1973); Benveniste (1987)). The latter calculations were carried out on the hierarchical sequence of microstructural configurations shown in Figure 5-6. The excellent agreement provide confidence in using such computationally efficient analytical homogenization schemes for this type of application.

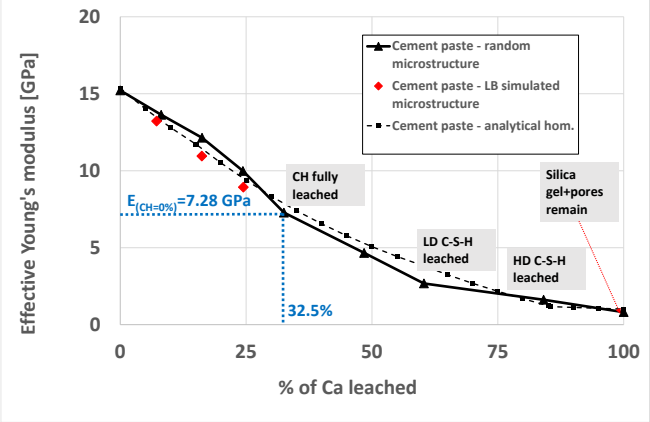

Figure 5-5: Young's modulus of cement paste as a function of mass % of Ca leached.

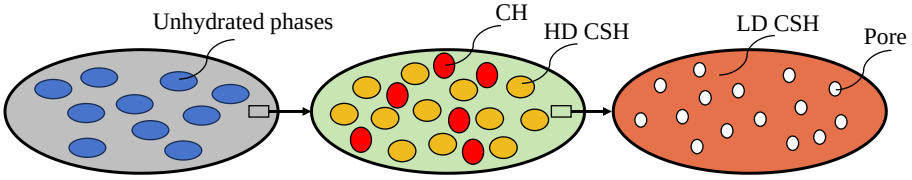

Figure 5-6: Microstructural configurations for analytical homogenization.

Table 5-5: Literature data on elastic properties of sound and leached cement paste.

	Material	w/c ratio	State	Young's modulus	Poisson's ratio	Time	Method
Sound cement paste							
This study	CEM I	0.5	Intact	15.2 GPa	0.28	85% hydration	Numerical homogenization
Honorio et al. (2014)	CEM I	0.5	Intact	15-16 GPa	0.27-0.28	100% hydration	Analytical homogenization
Krishnya et al. (2021)	CEM I	0.55	Intact	14-15 GPa	0.26	1 year	Ultrasonic/load tests
Kamali et al. (2004)	CEM I	0.5	Intact	18.6 GPa	-	-	Numerical homogenization
Hain and Wriggers (2008)	OPC	0.55	Intact	13.42 GPa	0.2	-	Experimental
Hain and Wriggers (2008)	OPC	0.55	Intact	13.51 GPa	0.2	-	Numerical homogenization
Bernard et al. (2003)	OPC	0.5	Intact	18	-	100% hydration	Analytical homogenization
Degraded cement paste							
This study	CEM I	0.5	CH dissolved	7.3 GPa	0.32	85% hydration	Numerical homogenization
Kamali et al. (2004)	CEM I	0.5	CH dissolved	8.7 GPa	-	-	Numerical homogenization
Gallé et al. (2004)	CEM I	0.45	CH dissolved	7±0.5	-	-	Experimental
Yu and Zhang (2015)	CEM I	0.45	CH dissolved	7.64	-	-	Analytical homogenization

5.3 Impact of carbonation on the mechanical properties of cement paste

Carbonation is a much more complex process compared to Ca leaching. For the latter, it is clear that progress of leaching results in increase in porosity. So as a first approximation, it is possible to conceptualize leaching process through simple random microstructure generation even without resorting to reactive transport modelling. With carbonation, many hydrated phases can indeed simultaneously carbonate resulting in a more complex microstructural evolution. Therefore, ideally, pore scale reactive transport modelling is preferred to address the carbonation process. Nevertheless, similar to leaching, microstructural evolution due to carbonation is captured using a simplified conceptual model in this study.

In pore scale simulations the evolution of the microstructure is explicitly considered. The reactivity of solid phases, precipitation and dissolution, takes place at the explicit interface between the solid and fluid and is controlled by the interface specific reaction rates. A significant simplification can be achieved some phases can be considered as not reactive. It is generally well acknowledged that carbonation of CH occurs quicker than that of C-S-H due to faster reaction kinetics and leads to a decrease of the total porosity, the magnitude of which depends on the difference in molar volume of CH and calcite and the available volume fraction of CH. In this study, it is therefore assumed that CH is first to carbonate. Carbonation of LD and HD C-S-H results not only in calcite formation but also release of silica gel and porosity increase due to the dissolution of C-S-H phases. It is possible to estimate the volume fractions of these products given the molar volume of LD and HD C-S-H and silica gel (Table 5-4). For simplicity, it is assumed that LD C-S-H carbonates first and later HD C-S-H. Lastly, it is assumed that unhydrated clinkers do not participate in carbonation reaction. For the given initial volume fractions of various phases (Table 5-2) and the estimates of molar volumes provided in Table 5-4, the evolution of these phases are quantified in Table 5-6. The same is pictorially shown in Figure 5-6.

The calculations show that there will be a minor drop in the total porosity due to CH carbonation, as expected. However, C-S-H dissolution results in a net increase in the total porosity, though marginally for this cement composition. It is interesting to note that at the stage of complete carbonation, the silica gel occupies around 18% of volume in the cement paste RVE. At this stage a maximum of 53% of the volume is filled with calcite in the RVE. The remaining phases are mainly silica gel and pores in this simplified conceptual model. Based on Table 5-6, the snapshots of microstructural evolution due to carbonation is shown in Figure 5-7.

Table 5-6: Simplified phase evolution during carbonation used for random generation of cement microstructure.

	Intact cement paste	CH precipitated	LD C-S-H precipitated	HD C-S-H precipitated
Porosity	0.23	0.215	0.234	0.242
CH	0.144	0	0	0
LD C-S-H	0.235	0.235	0	0
HD C-S-H	0.337	0.337	0.337	0
Silica gel	0	0	0.069	0.176
Calcite	0	0.161	0.307	0.530
Unhydrated clinkers	0.051	0.051	0.051	0.051

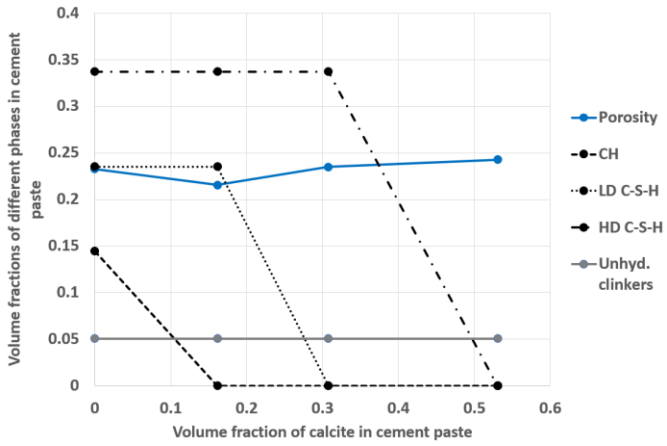

Figure 5-7: Simplified phase evolution during carbonation used for random generation of cement microstructure.

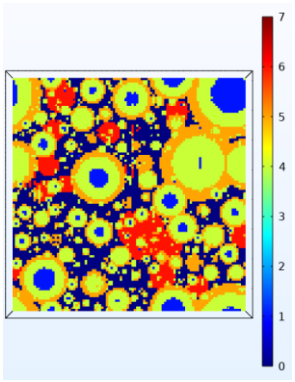

(a) Intact cement paste

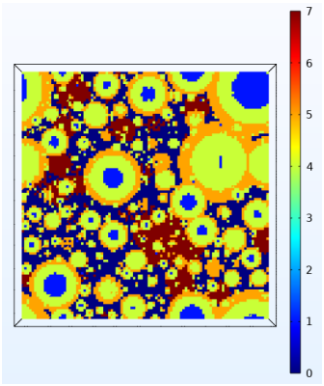

(b) CH fully carbonated

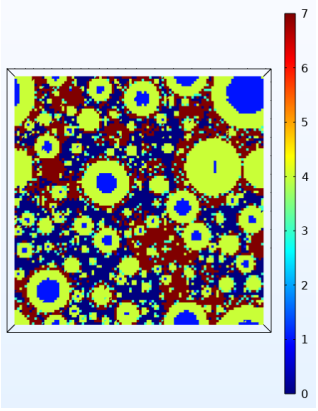

(d) LD C-S-H fully carbonated

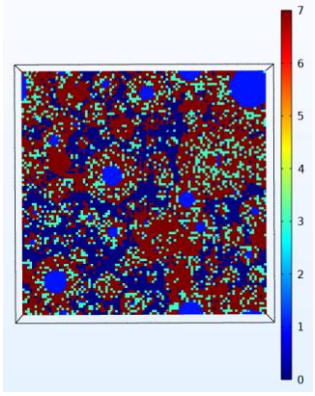

(d) HD C-S-H fully carbonated

0: water filled micropore; 1: Unhydrated clinkers; 3: Silica gel; 4: HD C-S-H; 5: LD C-S-H; 6: CH; 7: Calcite

Figure 5-8: Random generation of calcite precipitation in cement paste microstructure.

Figure 5-9 shows numerical homogenization of the modulus for various degree of carbonation, expressed in terms of volume fraction of calcite precipitated in the RVE of the cement paste. The results show a 30% increase in the effective modulus when CH is fully carbonated, 56% increase when LD C-S-H is fully carbonated and 94% increase when HD C-S-H is fully carbonated. In conclusion, a maximum of two-fold increase in the effective modulus is estimated by the model at full carbonation scenario. Also the relationship between the modulus and volume fraction of calcite is linear. There appears to be no experimental data on carbonated cement paste to validate the findings. This aspect is covered under Task 2 of EURAD-MAGIC, whose outcome is yet to be released.

As with the leaching analysis, the effect of carbonation on the effective modulus was also estimated using Mori-Tanaka scheme on the microstructural configurations shown in Figure 5-6. The results are superimposed in Figure 5-9. Once again, the excellent agreement between the numerical and analytical homogenization provide confidence in using such computationally efficient analytical methods for this type of application.

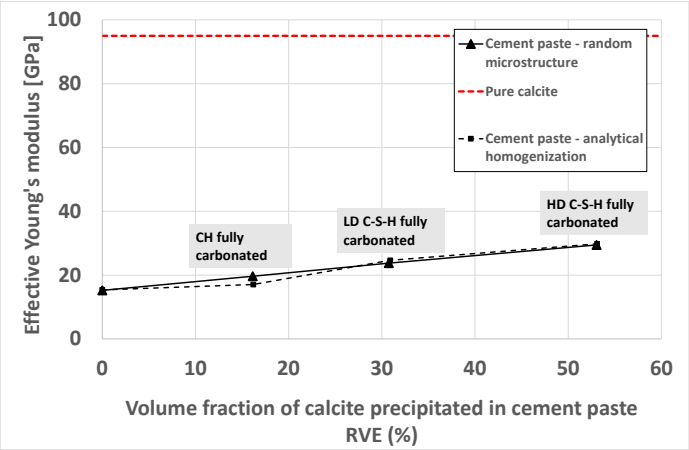

Figure 5-9: Young's modulus of cement paste as a function of volume fraction of cement paste RVE. Red horizontal line indicates elastic modulus of calcite.

5.4 Upscaling mechanical properties from cement paste to concrete

The distribution of aggregates in concrete is defined by a sieve curve. Sieve analysis helps to determine the particle size distribution of the coarse and fine aggregates. This is done by sieving the aggregates by using different sieves as standardized by the IS code and then pass aggregates through them and thus collect different sized particles left over different sieves. The mass that passed each sieve is weighted and given cumulatively in % of passed mass, which is called passing percentage.

For our initial analysis we used the concrete with the following sieve analysis (Figure 5-10).

Table 5-7: Sieve analysis of the reference concrete.

Sieve size [mm]	Passing percentage [%]
19	100.00
16	96.80
9.5	63.13
4.75	43.13
2.38	34.13
1.18	29.80
0.6	26.46
0.3	17.80
0.15	5.46
pan	1.80

The corresponding graphical representation is shown in Figure 5-10.

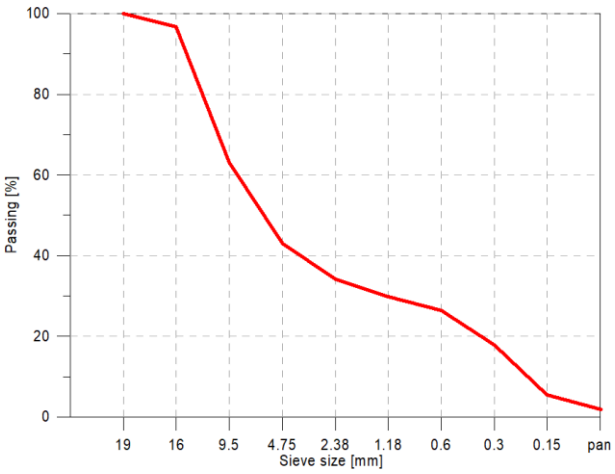

Figure 5-10: Visual representation of the sieve analysis for the reference concrete.

The initial scale is the scale of cement paste. Typical size is around 100μm to assure REV considering the larges solid phases. Considering the REV size from (Drugan & Willis, 1996) and rounding it up, we used factor 5 for each consecutive scale. This results in the range of spatial levels, each being 5 times larger than the previous one. Beginning from the paste scale of 100μm, the next level has a size of 500μm with a maximum particle size of 100μm, the next one 2.5mm with a maximum particle size of 500μm. Another level is 12.5mm and the final one is a bit larger than 62.5mm to be able to accommodate the largest aggregates of size 19mm (this results in a domain size of 95×95×95 mm^3).

5.4.1 Numerical generation of aggregates

Spherical aggregates are generated numerically to reproduce the sieve curve distribution. Spheres are randomly distributed in 3D domain. A truncated normal distribution of aggregate sizes is used to interpolate between each sieve value. The process of particle generation and placement stops when the required volume fraction of aggregates, V_{agg} Is reached.

Particle generation starts at the largest sizes of the sieve curve (i.e. between 16 mm and 19 mm in this study). The particles are generated one by one. Each aggregate particle is assigned to the appropriate spatial scale level (see Figure 5-11).

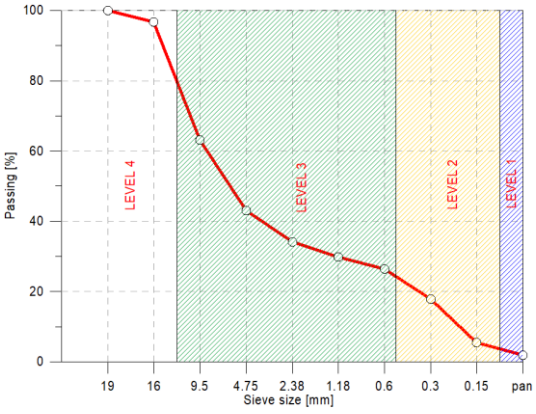

Figure 5-11: Sieve curve and spatial levels.

For illustration, the particles randomly generated in the interval from 9.5mm and 16mm could fall into level 4 if they are larger than 12.5mm or to level 3 if their size is below 12.5mm.

The level 4 is the “concrete” level. When the particle is assigned to level 3, it is assumed, that the same particle will be in each of the virtual smaller cubes in a larger domain. Hence, each generated sphere

contributes to the total volume with a multiplication factor of a ratio in Table 5-8 between a volume of a designated level cube and the largest volume given in the last column of Table 5-7.

The aggregates are added until the required volume fraction of aggregates is obtained. The position of aggregates is randomly chosen in a way that does not overlap with none of the previously generated particles at the same level.

The final representation of aggregates at different spatial levels is given in Figure 5-12.

Table 5-8: Properties of different length scale levels.

Level	Size [mm]	Volume [mm^3]	Ratio (versus level 4)
4	95	857375	1
3	12.5	1953.125	439
2	2.5	15.625	54872
1	0.5	0.125	685900
paste	0.1	0.001	857375000

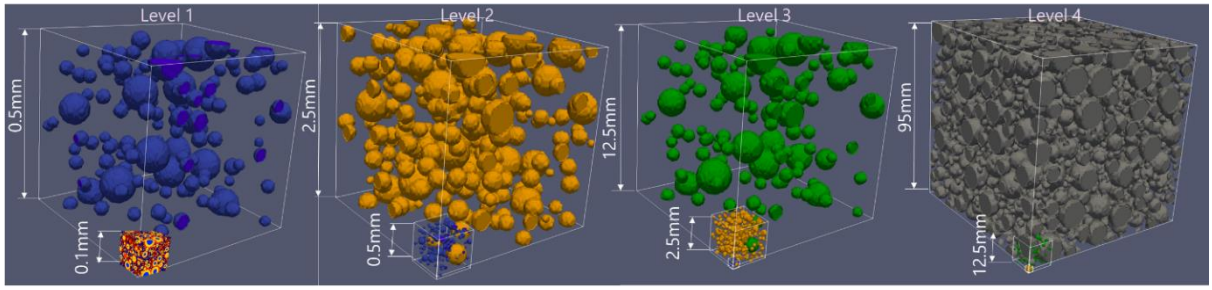

Figure 5-12: Distribution of aggregates at different spatial levels.

By summation of all aggregate volumes (Figure 5-12) we can reconstruct the sieve curve, which is shown in Figure 5-13.

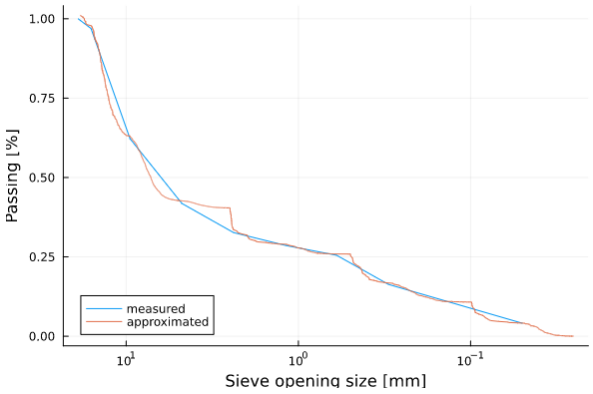

Figure 5-13: Comparison between measured and numerically generated sieve curve.

5.4.2 Mechanical properties of leached concrete

Figure 5-5 shows the effective modulus of leached concrete as a function of mass % of Ca leached. The model shows that the effective modulus reduces by approximately 30%, 60% and 70% when CH, LD C-S-H and HD C-S-H are fully leached, respectively. This is a significant loss of effective modulus.

Experimental data for validation is covered under Task 2 of EURAD-MAGIC, which are not yet available. Although direct comparison of the results is difficult due to a lack of literature data, at least, the trend can be compared based on analytical homogenization on similar cement carried out by Heukamp (2003) on mortar. They report 16% and 80% reduction in the effective modulus when CH and C-S-H are fully leached, though within the same order of magnitude, deviates from this study because the material used here is a concrete.

Figure 5-15 shows leaching damage function for concrete, which is typically used in continuum damage mechanics based formulations, and in particular, useful for the participants of Task 4 dealing with structural scale calculations.

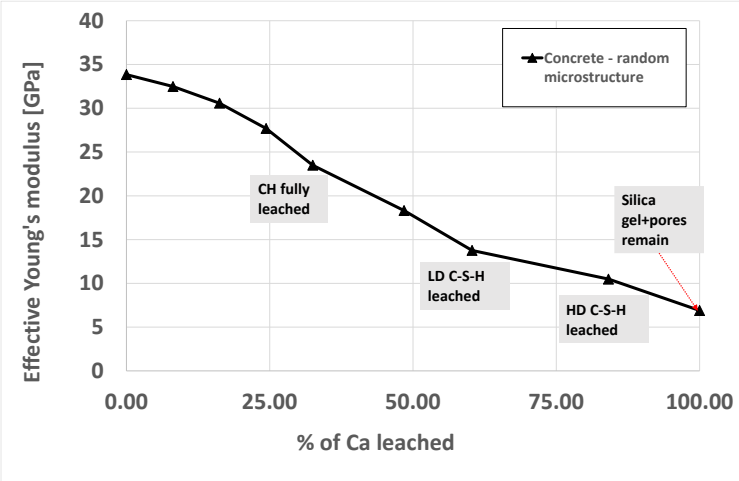

Figure 5-14: Young's modulus of concrete as a function of mass % of Ca leached.

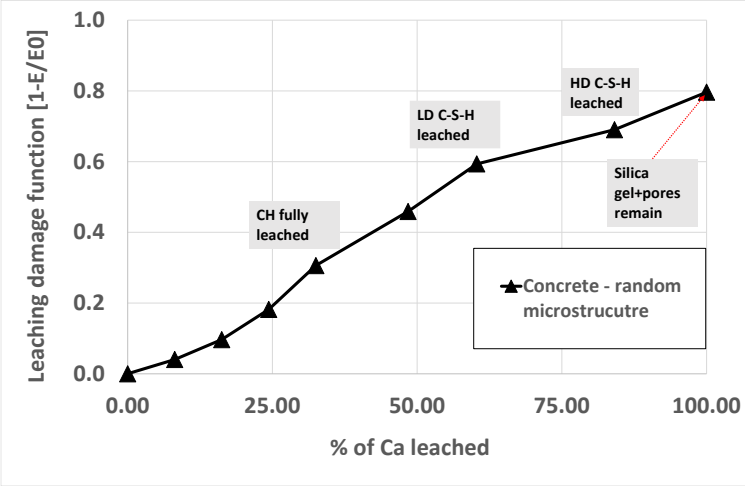

Figure 5-15: Leaching damage function derived from leaching at different levels shown in Figure 5-3 for concrete.

5.4.3 Mechanical properties of carbonated concrete

Figure 5-14 shows the effective modulus of carbonated concrete as a function of volume fraction of concrete RVE. The model shows that the effective modulus increases by approximately 15%, 24% and 37% when CH, LD C-S-H and HD C-S-H are fully carbonated, respectively. Experimental data for validation is covered under Task 2 of EURAD-MAGIC, which are not yet available. Although direct comparison of the results is difficult due to a lack of literature data, at least, the trend can be compared based on analytical homogenization (Mori-Tanaka) on similar concrete carried out by Ghorbanbeigi et al. (2016) on concrete, which shows a maximum increase of effective modulus to 46 GPa at full

carbonation, whereas this study shows 46.5 GPa. In their study this corresponds to 8% volume fraction of calcite in a concrete RVE, as against 17% in this study. The volume fraction of aggregates in their study is 67%, whereas in this study it is 66.7%. However, note that the Young's modulus of the cement paste in their study is 25 GPa as against 15 GPa in this study (Figure 5-16). On the other hand, the effective modulus of concrete in their study is 34 GPa at 4 weeks (in this study also approx. 34 GPa) and 46 GPa at 56 weeks.

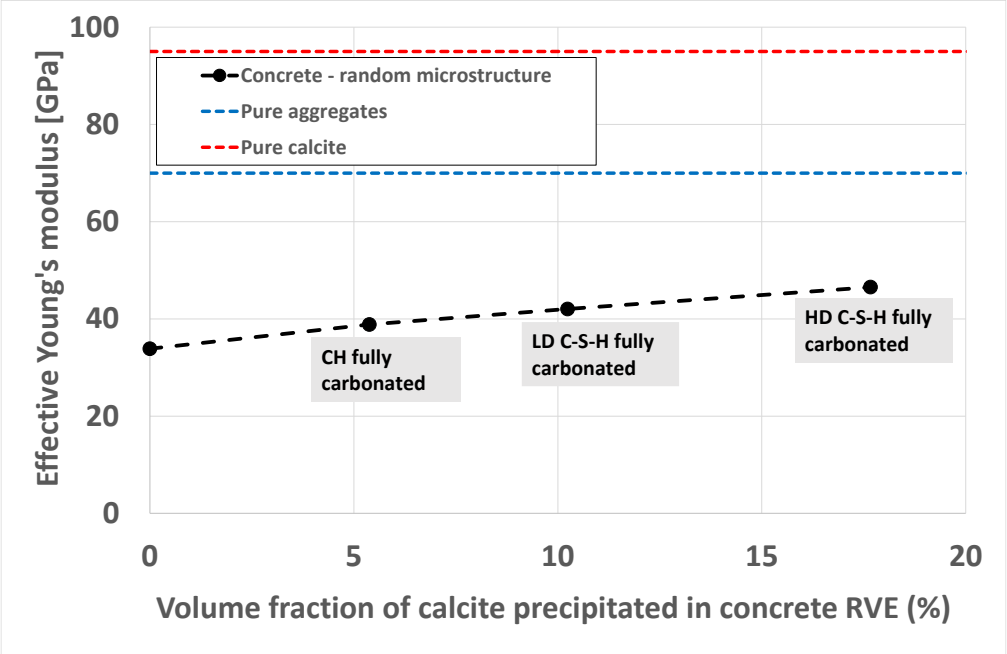

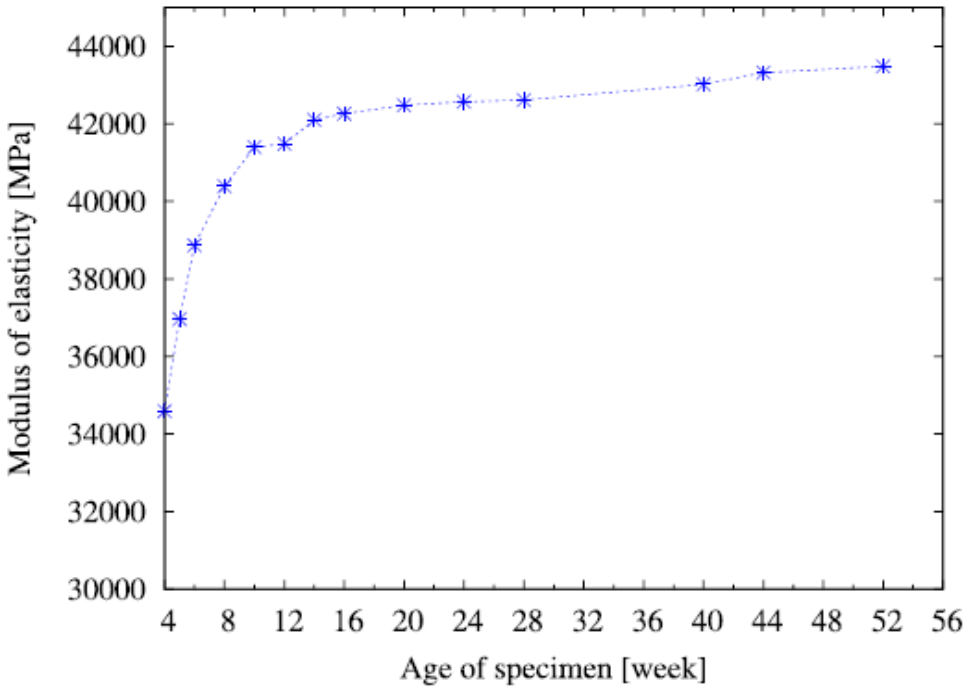

Figure 5-16: Young's modulus of concrete as a function of volume fraction of concrete RVE (top); (bottom) Young's modulus in the study of Ghorbanbeigi et al. 2016 (no copyright sought).

6. Summary

6.1 Future development needs

Cement paste and concrete are intrinsically multiscale materials, due to multipole distribution of pore sizes, minerals and aggregates sizes, as well as the differences in the corresponding chemo mechanical characteristics of the materials. A unified simultaneous description of the processes controlling the chemo-mechanical properties of concrete with a single computer code, or a model is not feasible. The complexity of multiscale nature of the processes requires separate evaluation of relevant processes at relevant scales. Hence, the focus of the future research and development should be set on in the accurate description of the scale dependent phenomena, upscaling material processes and development of code couplings capable of addressing scale transition phenomena (e.g., explains the emergence of material properties on larger scales from the interaction between nonlinearities and variation at the corresponding subscales).

Considering the reactive transport phenomena at the pore scale one of the major challenges in the multi-scale modelling of systems with several primary and secondary phases is coupled description of dissolution and precipitation reactions. These phenomena are either described considering multiple phases reacting in a single voxel or treating the voxel as single phase solid or fluid representative. Whereas the dissolution is described by well-defined reaction kinetic equation, the precipitation is more complex phenomena depending on the phase nucleation probability. The approaches developed on the basis on classical nucleation theory was shown to be successful for description of crystallization in natural systems. Some phases, however, are known to have follow non classical nucleation pathway (e.g. amorphous and crystalline polymorphs of carbonates (Gebauer et al., 2018). Significant efforts are still needed for the implementation of concurrent dissolution and precipitation/nucleation models in high performance reactive transport codes.

Reactive transport modelling used for numerical modelling of mass transport phenomena rely on geochemical solvers for speciation calculations. Analysis of the execution time necessary for mass transport and the geochemical calculations shows that later can consume more than 90% of the wall time. Significant speed up can be achieved replacing native geochemical solved with a surrogate model of reduced dimension based on Neural Networks for example. Further NN based routines can be translated for GPU execution automatically. This substantially facilitate application of the codes at modern High Performance Architecture heavily relying on the distributed graphical processor units. Further development and testing are necessary in automated training and validation of surrogate models for geochemical system. Continuation of international benchmarking exercises and development of practical guidelines for the training of surrogate modelling would be beneficial for boosting reactive transport modelling cement degradation.

The methods for deriving mechanical properties based on the 3D representation of mineral phases and pores are mature and widely used in numerical simulation. The precondition for the successful application of the described techniques is an accurate representation of mineral phases and porosity on a numerical grid. This can be challenging if the temporal evolution of the system over a long period needs to be considered. In the past few decades, significant advancements have been made in understanding the nonlinear behaviour of heterogeneous materials. In particular, various macroscopic strength criteria have been developed to assess the failure stresses of materials. However, establishing analytical strength criteria requires simplification of the microstructural morphology of concrete materials. By dividing the material into two scales, the matrix of the material conforms to the Drucker-Prager criterion at the microscopic scale. Applying this schema, an ANN-based model for evaluating the macroscopic strength of concrete was developed where the modelling data set was derived from FFT numerical simulations. A distinctive feature of this model is its consideration of the influence of porosity and inclusion volume fraction on the macroscopic mechanical properties of concrete-like materials. The performance of the ANN model was evaluated using various statistical metrics, demonstrating its high

accuracy. It is evident that the ANN model can successfully reproduce the results obtained from traditional numerical simulations.

Due to the complexity of topological arrangement and chemical interaction between cement paste and aggregates the upscaling of mechanical properties in concrete is a challenging task conducted following a multiscale approach. The distribution of aggregates in concrete is defined by a sieve curve. Sieve analysis helps to determine the particle size distribution of the coarse and fine aggregates. A simplified models based on spherical aggregates randomly distributed in the 3D domain demonstrate good agreement with available data. Further studies are necessary to analyze the effects of the model resolution, aggregate asymmetry and eventually spatial correlation might be necessary. Considering chemo mechanical coupling in large scale simulation it would be beneficial to develop robust analytical model for mechanical properties or surrogate one with high computational performance. Further the approach can be extended to the analysis of alternative cement formulation specifically developed for geological disposal system such as low pH concrete having a different mechanical behavior with carbonation.

6.2 Needs for validation experiments

Successful model development needs to go hand on hand with the experimental data for the model verification and validation of numerical predictions. Most of the theoretical development described above we cross benchmarked with other sophisticated numerical methods. In WP-Magic Task 2 and Task3 several experiments have been setup to provide data for model validations.

In the task 3.1, series of experiments have been setup to analyse the chemical degradation and evolution of mechanical properties of cement paste and mortar subject to interaction with Opalinus pore water by destructive by destructive and non-destructive techniques. The analysis includes periodic measurement of tracer diffusivity and analysis of fluid accessible porosity. Non-destructive ultrasonic measurements of elastic properties and non-linear ultrasonic spectroscopy for identification of microstructure damage and crack initiation. Upon competition of the experimental measurements the samples are analysed with traditional destructive methods to reveal mineralogical changes and chemical evolution profiles access the sample. These data are to be used for the benchmarking and calibration of reactive transport codes and chemo mechanical homogenisation approaches developed described in the report. A similar set of data are also available in Task 2 for the set of concrete samples on cm-dm scale.

Numerical homogenisation of elastic properties described above is conducted for a 3D representation of mineral phases and pores within the material on a grid. Currently, the models are based on numerical simulation of hydrates structure such as CEMHYD3D (Bentz, 2005), HYMOSTRUC3D (Gao et al. 2019), etc. It could be much more advantageous to use direct input from 3D CT (e.g. x-ray CT or neutron radiography) and to perform mechanical test on the analysed sample. As the CT resolution closely related to the sample size a multi scale analysis would be necessary.

In task 3.3 and task 2, experimental program is implemented to characterise effect of microbial activity on mineral reactivity. Upon finalisation of the microbiological experiments on the surface substrates measured the surface topographies will be applied in numerical model to estimate the reactivity of the carbonate models in presence of bacteria and the derive their effective reactivity constants for necessary for the simulation of chemical degradation.

Within the MAGIC project, HZDR developed a pore-scale reactive transport mode for describing the coupled processes of flow, multi-component transport, microbially induced calcite precipitation, and evolution of the solid surface. The developed model is validated using published experimental data and ready to be used for the interpretation of the experimental results of biofilm growth to be obtained in the project. The numerical experiments focus on fluid flow through a 2D channel with a rough surface. The numerical results show that heterogeneous calcite precipitation causes a generally decreased surface roughness under advection-dominated and transport-limited conditions. Moreover, the results of power spectral density analysis demonstrate that microbially induced calcite precipitation affects surface

topography both through general changes in surface roughness over the entire spatial frequency range (trend of fractal dimension change) and via local modifications in surface topography in the micron wavelength spatial frequency range. Sensitivity studies clearly show that uniform and non-uniform types of precipitation can be caused by different flow rates. Such different types of precipitation lead to different surface shapes. Quantitative insights into the evolution of surface height under different flow and reaction conditions provide a comprehensive understanding of surface evolution by microbially induced calcite precipitation at the pore scale. This has implications for enhanced predictability of contaminant transport in the subsurface with microbial activities at the core scale and beyond.

6.3 Conclusion

Task 3 of WP-MAGIC had an ambitious goal of analysis the microstructure evolution and mechanical properties cement paste under chemical factor such as internal degradation, chemical recrystallisation/leaching due to the interaction with formation water and microbial activities. The current report provides analysis of existing numerical models and describe the newest development accomplished in the course of WP-MAGIC.

The analysis confirms that the magnesium attack is characterised by the dissolution of C-S-H and ettringite, as well as by the formation of M-S-H during the contact between a low-pH paste/concrete and an environment containing magnesium. As M-S-H has much lower microstructural and mechanical properties than C-S-H, the replacement of C-S-H by M-S-H does not maintain good mechanical and microstructural properties. Even if a new semi-amorphous phase is formed, the mechanical properties of the paste are significantly reduced during magnesium attack.

In the course, of the project a multiphase LB code for the reactive transport simulation was coupled with surrogate model chemical equilibria in cement paste. This code was applied for the analysis of temporal evolution of cement phase under leaching and carbonation in 3D using realistic representation of mineral phases and boundary condition. Such analysis not only provide access to the spatial evolution of the microstructure but also set temporal constraints on the evolution scenario. Obtained microstructures used for the numerical homogenisation of mechanical properties enable to estimate temporal scale for mechanical degradation of cement paste performance. Interestingly the spatial evolution of the microstructure and the mechanical properties by time dependent simulations are comparable with the results obtained for a much more simplified model using a stochastic description of dissolution/precipitation phenomena without rigorous time constraints. The principles of numerical homogenization developed for cement paste are applicable for the mortar and concrete. The analysis includes homogenized cement paste, interfacial transition zone (ITZ), air voids and aggregates.

A pore-scale reactive transport mode for describing the coupled processes of flow, multi-component transport, microbially induced calcite precipitation, and evolution of the solid surface was developed and validated using published experimental data and ready to be used for the interpretation of the experimental results of biofilm growth to be obtained in the project. The numerical experiments focus on fluid flow through a 2D channel with a rough surface. The numerical results show that heterogeneous calcite precipitation causes a generally decreased surface roughness under advection-dominated and transport-limited conditions. Moreover, the results of power spectral density analysis demonstrate that microbially induced calcite precipitation affects surface topography both through general changes in surface roughness over the entire spatial frequency range (trend of fractal dimension change) and via local modifications in surface topography in the micron wavelength spatial frequency range. Sensitivity studies clearly show that uniform and non-uniform types of precipitation can be caused by different flow rates. Such different types of precipitation lead to different surface shapes. Quantitative insights into the evolution of surface height under different flow and reaction conditions provide a comprehensive understanding of surface evolution by microbially induced calcite precipitation at the pore scale. This has implications for enhanced predictability of contaminant transport in the subsurface with microbial activities at the core scale and beyond. This pore-scale study presents insights into the microscopic physicochemical processes of biofilm-mineral-fluid interaction and its impact on surface topography and

solute transport. Overall, the generalizable approach presented in this study contributes to improve the predictability of contaminant transport at the pore scale.

Significant progress has been achieved in the applying ML and AI approaches for acceleration of numerical simulation in reactive transport modelling and upscaling the mechanical properties of the cementitious systems. With the several orders of computational speedup for surrogate models replacing native geochemical solvers, time resolved 3D reactive transport simulations of the microstructure evolution become possible. Further, ANN-based model has been developed in the course of WP-Magic to complete and improve the analytical models for elastic moduli of cement paste. The results provided by the ANN model are very good agreement with those obtained from the FFT-based direct simulations.

It has to be noted, that not all the experimental results are available for analysis by the time of this report delivery due to very short project schedule on the one hand and naturally long/slow evolution of the materials on the other. Therefor the cross comparison of the modelling results with the experimental observation is ongoing and will continue as experimental result become available.

Finally, a successful step by step upscaling of mechanical properties form cement paste to concrete scale was demonstrated.

7. References

Ahrens J. P., Geveci B., and Law C. C. (2005) Para View: An End-User Tool for Large-Data Visualization. The Visualization Handbook.

Aldakheel F. (2020) A microscale model for concrete failure in poro-elasto-plastic media. Theoretical and Applied Fracture Mechanics 107:102517.

Arias, D., Cisternas, L. A., Miranda, C., & Rivas, M. (2018). Bioprospecting of Ureolytic Bacteria From Laguna Salada for Biomineralization Applications. *Front. Bioeng. Biotechnol., 6*, 209. doi:10.3389/fbioe.2018.00209

Babaei S. (2021) A Multiscale Approach to Model Thermo-Hydro-Mechanical Behaviour of non-reinforced Concrete. PhD Thesis, University of Antwerp.

Bach T.T.H., Coumes C.C.D., Pochard I., Mercier C., Revel B., Nonat A. (2012) Influence of temperature on the hydration products of low pH cements, Cement and Concrete Research. 42: 805–817.

Baji H., Yang W., Li C.-Q. and Shi W. (2019) Analytical models for effective hydraulic sorptivity, diffusivity and conductivity of concrete with interfacial transition zone. Construction and Building Materials 225:555-568.

Bentz D.P. (2005) CEMHYD3D: A Three-Dimensional Cement Hydration and Microstructure Development Modeling Package. Version 3.0., NIST Interagency/Internal Report (NISTIR), National Institute of Standards and Technology, Gaithersburg, MD, [online]. https://doi.org/10.6028/NIST.IR.7232 (Accessed April 15, 2022).

Benveniste Y. (1987) A new approach to the application of Mori-Tanaka's theory in composite materials. Mechanics of materials 6 (2):147-157.

Bernard E., Lothenbach B., Le Goff F., Pochard I., Dauzères A. (2017) Effect of magnesium on calcium silicate hydrate (C-S-H). Cement and Concrete Research 97: 61–72.

Bernard O., Ulm F.-J. and Lemarchand E. (2003) A multiscale micromechanics-hydration model for the early-age elastic properties of cement-based materials. Cement and Concrete Research 33 (9):1293-1309.

Bibi, S., Oualha, M., Ashfaq, M. Y., Suleiman, M. T., & Zouari, N. (2018). Isolation, differentiation and biodiversity of ureolytic bacteria of Qatari soil and their potential in microbially induced calcite precipitation (MICP) for soil stabilization. *RSC Adv.*, 8(11), 5854-5863. doi:10.1039/c7ra12758h

Bignonnet F., Hassen G. and Dormieux L. (2016) Fourier-based strength homogenization of porous media. Computational Mechanics 58 (5):833-859.

Brinkman, H. C. (1947). A calculation of the viscous force exerted by a flowing fluid on a dense swarm of particles. *Appl. Sci. Res.*, 1(1), 27-34. doi:10.1007/BF02120313

Cao Y., Shen W., Burlion N. and Shao J.-F. (2018a) Effects of inclusions and pores on plastic and viscoplastic deformation of rock-like materials. International Journal of Plasticity 108:107-124.

Cao Y., Shen W., Shao J.-F. and Burlion N. (2018b) Influences of micro-pores and meso-pores on elastic and plastic properties of porous materials. European Journal of Mechanics-A/Solids 72:407-423.

Cao Y., Shen W., Shao J.-F. and Wang W. (2020) A novel FFT-based phase field model for damage and cracking behavior of heterogeneous materials. International Journal of Plasticity 133:102786.

Carrillo J., Ramirez J. and Lizarazo-Marriaga J. (2019) Modulus of elasticity and Poisson's ratio of fiber-reinforced concrete in Colombia from ultrasonic pulse velocities. Journal of Building Engineering 23:18-26.

Christensen R.M. (2012) Mechanics of composite materials: Courier Corporation.

Codina M., Cau-dit-Coumes C., Le Bescop P., Verdier J., Ollivier J.P. (2008) Design and characterization of low-heat and low-alkalinity cements. Cement and Concrete Research 38: 437–448.

Das S., Maroli A., Singh S. S., Stannard T., Xiao X., Chawla N. and Neithalath N. (2016) A microstructure-guided constitutive modeling approach for random heterogeneous materials: Application to structural binders. Computational Materials Science 119:52-64.

Dauzeres A., Achiedo G., Nied D., Bernard E., Alahrache S., Lothenbach B. (2016) Magnesium perturbation in low-pH concretes placed in clayey environment—solid characterizations and modeling, Cement and Concrete Research 79: 137–150.

Deng, H., Molins, S., Trebotich, D., Steefel, C., & DePaolo, D. (2018). Pore-scale numerical investigation of the impacts of surface roughness: Upscaling of reaction rates in rough fractures. *Geochim. Cosmochim. Acta*, 239, 374-389. doi:10.1016/j.gca.2018.08.005

Dunant C. F., Bary B., Giorla A. B., Péniguel C., Sanahuja J., Toulemonde C., Tran A.-B., Willot F. and Yvonnet J. (2013) A critical comparison of several numerical methods for computing effective properties of highly heterogeneous materials. Advances in Engineering Software 58:1-12.

Dupin, H. J., Kitanidis, P. K., & McCarty, P. L. (2001). Pore-scale modeling of biological clogging due to aggregate expansion: A material mechanics approach. *Water Resour. Res.*, 37(12), 2965-2979.

Duplan F., Abou-Chakra A., Turatsinze A., Escadeillas G., Brule S. and Masse F. (2014) Prediction of modulus of elasticity based on micromechanics theory and application to low-strength mortars. Construction and Building Materials 50:437-447.

Ebigbo, A., Golfier, F., & Quintard, M. (2013). A coupled, pore-scale model for methanogenic microbial activity in underground hydrogen storage. *Adv. Water Resour.*, 61, 74-85. doi:10.1016/j.advwatres.2013.09.004

Fang, C., & Achal, V. (2019). Biostimulation of calcite precipitation process by bacterial community in improving cement stabilized rammed earth as sustainable material. *Appl. Microbiol. Biotechnol.*, 103(18), 7719-7727. doi:10.1007/s00253-019-10024-9

Galan I. et al. (2015) Assessment of the protective effect of carbonation on portlandite crystals. Cement and Concrete Research 74: 68-77.

Gallé C., Peycelon H. and Le Bescop P. (2004) Effect of an accelerated chemical degradation on water permeability and pore structure of cementbased materials. Advances in cement research, 16(3), 105-114.

Gao P., Ye G., Wei J. and Yu Q. (2019) Extension of the Hymostruc3D model for simulation of hydration and microstructure development of blended cements. Heron 64(1/2): 125.

Garboczi E. J. and Bentz D. P. (1997) Analytical formulas for interfacial transition zone properties. Advanced Cement Based Materials 6 (3-4): 99-108.

Gebauer D., Raiteri P., Gale J. D. and Cölfen H. (2018) On classical and non-classical views on nucleation. American Journal of Science 318: 969-988.

Hain M., Wriggers P. (2008) Computational homogenization of micro-structural damage due to frost in hardened cement paste, Finite Elements in Analysis and Design 44(5) 233-244.

Hashin Z. and Monteiro P. (2002) An inverse method to determine the elastic properties of the interphase between the aggregate and the cement paste. Cement and Concrete Research 32 (8):1291-1300.

Hashin Z. and Shtrikman S. (1963) A variational approach to the theory of the elastic behaviour of multiphase materials. Journal of the Mechanics and Physics of Solids 11 (2):127-140.

He J., Gao R. and Tang Z. (2022) A data-driven multi-scale constitutive model of concrete material based on polynomial chaos expansion and stochastic damage model. Construction and Building Materials 334:127441.

Herve E., Care S. and Seguin J. P. (2010) Influence of the porosity gradient in cement paste matrix on the mechanical behavior of mortar. Cement and Concrete Research 40 (7):1060-1071.

Idiart M. I., Willot F., Pellegrini Y.-P. and Castaneda P. P. (2009) Infinite-contrast periodic composites with strongly nonlinear behavior: Effective-medium theory versus full-field simulations. International Journal of Solids and Structures 46 (18-19):3365-3382.

Jacques D., Perko J., Seetharam S.C., Mallants D. (2014) A cement degradation model for evaluating the evolution of retardation factors in radionuclide leaching models Applied Geochemistry 49: 143–158.

Jenni A., Mäder U., Lerouge C., Gaboreau S., Schwyn B. (2014) In situ interaction between different concretes and Opalinus Clay. Phys. Chem. Earth Parts A/B/C, 70, 71–83.

Jeong, J. H., Jo, Y. S., Park, C. S., Kang, C. H., & So, J. S. (2017). Biocementation of Concrete Pavements Using Microbially Induced Calcite Precipitation. *J. Microbiol. Biotechnol.*, 27(7), 1331-1335. doi:10.4014/jmb.1701.01041

Johannsen K. and Rademacher S. (1999) Modelling the Kinetics of Calcium Hydroxide Dissolution in Water. Acta hydrochimica et hydrobiologica 27(2): 72-78.

Johnstone, E. V., Hofmann, S., Cherkouk, A., & Schmidt, M. (2016). Study of the Interaction of Eu(3+) with Microbiologically Induced Calcium Carbonate Precipitates using TRLFS. *Environ. Sci. Technol.*, 50(22), 12411-12420. doi:10.1021/acs.est.6b03434

Kanthe V. N., Deo S. V. and Murmu M. (2022) Modulus of elasticity of blended concrete containing multiple admixtures for sustainability infrastructural material. Innovative Infrastructure Solutions 7:1-10.

Kulik D. A. (2011) Improving the structural consistency of C-S-H solid solution thermodynamic models. Cement and Concrete Research 41(5):477-495.

Kulik D.A. et al. (2013) GEM-Selektor geochemical modeling package: revised algorithm and GEMS3K numerical kernel for coupled simulation codes. Computational Geosciences 17(1): 1-24.

Lallemand P. and Luo L.-S. (2000) Theory of the lattice Boltzmann method: Dispersion, dissipation, isotropy, Galilean invariance, and stability. Physical Review E. 61(6): 6546-6562.

Lasaga A. C. (2014) Kinetic Theory in the Earth Sciences. Princeton University Press.

Li C. Q., Zheng J., Zhou X. and McCarthy M. (2003) A numerical method for the prediction of elastic modulus of concrete. Magazine of Concrete Research 55 (6):497-505.

Li Y. and Metcalf J. B. (2005) Two-step approach to prediction of asphalt concrete modulus from two-phase micromechanical models. Journal of Materials in Civil Engineering 17 (4):407-415.

Liu B. and Lu W. (2022) Surrogate models in machine learning for computational stochastic multi-scale modelling in composite materials design. International Journal of Hydromechatronics 5 (4):336-365.

Liu C., Xie D., She W., Liu Z., Liu G., Yang L. and Zhang Y. (2018) Numerical modelling of elastic modulus and diffusion coefficient of concrete as a three-phase composite material. Construction and Building Materials 189:1251-1263.

Ma, L., Pang, A. P., Luo, Y., Lu, X., & Lin, F. (2020). Beneficial factors for biomineralization by ureolytic bacterium Sporosarcina pasteurii. *Microb Cell Fact*, 19(1), 12. doi:10.1186/s12934-020-1281-z

Martin, D., Dodds, K., Ngwenya, B. T., Butler, I. B., & Elphick, S. C. (2012). Inhibition of Sporosarcina pasteurii under anoxic conditions: implications for subsurface carbonate precipitation and remediation via ureolysis. *Environ. Sci. Technol.*, 46(15), 8351-8355. doi:10.1021/es3015875

Maghous S., Dormieux L. and Barthelemy J. (2009) Micromechanical approach to the strength properties of frictional geomaterials. European Journal of Mechanics-A/Solids 28 (1):179-188.

McLaughlin S. (1977) Electrostatic potentials at membrane-solution interfaces. In Current topics in membranes and transport: Elsevier, 71-144.

Mitchell, A. C., Espinosa-Ortiz, E. J., Parks, S. L., Phillips, A. J., Cunningham, A. B., & Gerlach, R. (2019). Kinetics of calcite precipitation by ureolytic bacteria under aerobic and anaerobic conditions. *Biogeosciences*, 16(10), 2147-2161. doi:10.5194/bg-16-2147-2019

Mokos A. et al. (in preparation) Accelerated pore-level modelling of portlandite dissolution.

Mori T. and Tanaka K. (1973) Average stress in matrix and average elastic energy of materials with misfitting inclusions. Acta metallurgica 21 (5):571-574.

Nadeau J. (2003) A multiscale model for effective moduli of concrete incorporating ITZ water–cement ratio gradients, aggregate size distributions, and entrapped voids. Cement and Concrete Research 33 (1):103-113.

Nagra (2021) Waste Management Programme 2021. Nagra Technical Report NTB 21-01E.

Nasser, A. A., Sorour, N. M., Saafan, M. A., & Abbas, R. N. (2022). Microbially-Induced-Calcite-Precipitation (MICP): A biotechnological approach to enhance the durability of concrete using Bacillus pasteurii and Bacillus sphaericus. *Heliyon*, 8(7), e09879. doi:10.1016/j.heliyon.2022.e09879

Neji M., Dauzères A., Grellier A., Sammaljärvi J., Tikkanen O., Siitari-Kauppi M. (2022) Comparison of the chemo-mechanical behavior of low-pH cement exposed to calcareous water and to argillite pore water. Applied Geochemistry 144: 105392.

Parkhurst, D. L., & Appelo, C. A. J. (2013). Description of input and examples for PHREEQC version 3: a computer program for speciation, batch-reaction, one-dimensional transport, and inverse geochemical calculation (6-A43). Retrieved from Reston, VA, USA.

Perko J., Ukrainczyk N., Šavija B., Phung Q.T, Koenders E.A.B, (2020) Influence of Micro-Pore Connectivity and Micro-Fractures on Calcium Leaching of Cement Pastes-A Coupled Simulation Approach. Materials (Basel),13(12), 2697.

Prasianakis N. I. et al. (2009) Lattice Boltzmann method with restored Galilean invariance. Physical Review E. 79(6).

Prasianakis N. I. et al. (2020) Neural network based process coupling and parameter upscaling in reactive transport simulations. Geochimica Et Cosmochimica Acta 291:126-143.

Qian Y.-H., d'Humières D. and Lallemand P. (1992) Lattice BGK models for Navier-Stokes equation. EPL (Europhysics Letters) 17(6): 479.

Qu J. and Cherkaoui M. (2006) Fundamentals of micromechanics of solids. Wiley Online Library Vol. 735.

Ramesh G., Sotelino E. and Chen W. (1996) Effect of transition zone on elastic moduli of concrete materials. Cement and Concrete Research 26 (4):611-622.

Rumelhart D. E., Hinton G. E. and Williams R. J. (1986) Learning representations by back-propagating errors. Nature 323(6088):533-536.

NIROND (2001) Technical overview of the SAFIR 2 report, Safety Assessment and Feasibility Interim Report 2, NIROND 2001–05 E.

Soulaine, C., Roman, S., Kovscek, A., & Tchelepi, H. A. (2017). Mineral dissolution and wormholing from a pore-scale perspective. *J. Fluid Mech.*, 827, 457-483. doi:10.1017/jfm.2017.499

Soulaine, C., & Tchelepi, H. A. (2016). Micro-continuum Approach for Pore-Scale Simulation of Subsurface Processes. *Transp. Porous Media*, 113(3), 431-456. doi:10.1007/s11242-016-0701-3

Scrivener, K. L. and R. J. Kirkpatrick (2008). Innovation in use and research on cementitious material. Cement and Concrete Research 38: 128-136.

Shen W., Kondo D., Dormieux L. and Shao J.-F. (2013) A closed-form three scale model for ductile rocks with a plastically compressible porous matrix. Mechanics of materials 59:73-86.

Shen W. and Shao J.-F. (2016) An incremental micro-macro model for porous geomaterials with double porosity and inclusion. International Journal of Plasticity 83:37-54.

Shen W., Shao J.-F., Burlion N. and Liu Z. (2020a) A microstructure-based constitutive model for cement paste with chemical leaching effect. Mechanics of materials 150:103571.

Shen W., Shao J.-F., Kondo D. and Gatmiri B. (2012) A micro–macro model for clayey rocks with a plastic compressible porous matrix. International Journal of Plasticity 36:64-85.

Shen W., Shao J.-F., Liu Z., Oueslati A. and De Saxcé G. (2020b) Evaluation and improvement of macroscopic yield criteria of porous media having a Drucker-Prager matrix. International Journal of Plasticity 126:102609.

Shen W., Zhang J., Shao J. and Kondo D. (2017) Approximate macroscopic yield criteria for Drucker-Prager type solids with spheroidal voids. International Journal of Plasticity 99:221-247.

Steefel, C. I., Yabusaki, S. B., & Mayer, K. U. (2015). Reactive transport benchmarks for subsurface environmental simulation. *Comput. Geosci.*, 19(3), 439-443. doi:10.1007/s10596-015-9499-2

Tinseau E., Bartier D., Hassouta L., Devol-Brown I., Stammose D. (2006) Mineralogical characterization of the Tournemire argillite after in situ interaction with concretes. Waste Management 26: 789–800.

Van Breugel K. (1995) Numerical simulation of hydration and microstructural development in hardening cement-based materials (I) theory. Cement and Concrete Research 25(2): 319-331.

Vilardell J., Aguado A., Agullo L. and Gettu R. (1998) Estimation of the modulus of elasticity for dam concrete. Cement and Concrete Research 28 (1):93-101.

Wang J. et al. (1998) The dissolution rate of Ca (OH) 2 in aqueous solutions. Chemical Engineering Communications 169(1): 167-184.

Wang J., Lubliner J. and Monteiro P. (1988) Effect of ice formation on the elastic moduli of cement paste and mortar. Cement and Concrete Research 18 (6):874-885.

Winter, N. (2009) Understanding cement. Suffolk, WHD Microanalysis Consultance LTD.

Wolf-Gladrow D. A. (2000) Lattice-gas cellular automata and lattice Boltzmann models - Introduction. Lattice-Gas Cellular Automata and Lattice Boltzmann Models 1725: 1-13.

Yoon, J.-H., Lee, K.-C., Weiss, N., Kho, Y. H., Kang, K. H., & Park, Y.-H. (2001). Sporosarcina aquimarina sp. nov., a bacterium isolated from seawater in Korea, and transfer of Bacillus globisporus (Larkin and Stokes 1967), Bacillus psychrophilus (Nakamura 1984) and Bacillus pasteurii (Chester 1898) to the genus Sporosarcina as Sporosarcina globispora comb. nov., Sporosarcina psychrophila comb. nov. and Sporosarcina pasteurii comb. nov., and emended description of the genus Sporosarcina. *Int. J. Syst. Evol. Microbiol*, 51, 1079–1086

Yuan, T., Ning, Y., & Qin, G. (2016). Numerical Modeling and Simulation of Coupled Processes of Mineral Dissolution and Fluid Flow in Fractured Carbonate Formations. *Transp. Porous Media*, 114(3), 747-775. doi:10.1007/s11242-016-0742-7

Yuan, T., Schymura, S., Bollermann, T., Molodtsov, K., Chekhonin, P., Schmidt, M., et al. (2021). Heterogeneous Sorption of Radionuclides Predicted by Crystal Surface Nanoroughness. *Environ. Sci. Technol.*, 55(23), 15797-15809. doi:10.1021/acs.est.1c04413

Yuan, T., Wei, C., Zhang, C.-S., & Qin, G. (2019). A numerical simulator for modeling the coupling processes of subsurface fluid flow and reactive transport processes in fractured carbonate rocks. *Water*, 11(10), 1957. doi:10.3390/w11101957

Zhang, T., & Klapper, I. (2010). Mathematical model of biofilm induced calcite precipitation. *Water Sci. Technol.*, 61(11), 2957-2964. doi:10.2166/wst.2010.064

Zheng J., Li C. Q. and Zhou X. (2006) An analytical method for prediction of the elastic modulus of concrete. Magazine of Concrete Research 58 (10):665-673.

Zheng J., Zhou X. and Jin X. (2012) An n-layered spherical inclusion model for predicting the elastic moduli of concrete with inhomogeneous ITZ. Cement and Concrete Composites 34 (5):716-723.

Zhu, T., & Dittrich, M. (2016). Carbonate Precipitation through Microbial Activities in Natural Environment, and Their Potential in Biotechnology: A Review. *Front. Bioeng. Biotechnol.*, 4, 4. doi:10.3389/fbioe.2016.00004